A Shear-Stress Responsive Nano-Container To Target Critically Constricted Arteries

Inauguraldissertation

zur

Erlangung der Würde eines Doktors der Philosophie
vorgelegt der
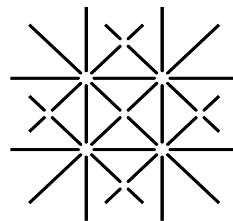
Philosophisch-Naturwissenschaftlichen Fakultät

der Universität Basel

von

Margaret Nancy Holme

aus Schottland

UNI
BASEL

Basel, 2014

Genehmigt von der Philosophisch-Naturwissenschaftlichen Fakultät auf Antrag von:

Prof. Dr. Bert Müller, Fakultätsverantwortlicher
Prof. Dr. Andreas Zumbuehl, Korreferent

Basel, den 26. Februar 2013

<div align="right">Prof. Dr. Jörg Schibler, Dekan</div>

Contents

Summary

Atherosclerosis and associated cardiovascular diseases are the world's biggest cause of mortality. During the acute case of heart attack, vasodilators are administered to open up the constricted artery and allow blood perfusion to the surrounding tissue. However, there are currently no treatments on the market that allow such drugs to be delivered locally to the site of a critically constricted artery. Such a targeted delivery method could significantly improve patient prognosis. The presented thesis is an account of the development of a shear-stress responsive nano-container that could fill this gap in the medic's toolbox, using the physical trigger of increased endogenous shear-stresses in critically constricted human coronary arteries.

In Chapter 2.1, an imaging protocol is presented that sequentially uses laboratory micro computed tomography (μCT), absorption- and phase-contrast synchrotron radiation-based μCT (SRμCT) to gather information on morphology and tissue composition of calcified and subsequently decalcified coronary arteries. This paves the way for micrometre-resolution data on the morphology and tissue distribution of a variety of typical critically constricted vessels.

For flow experiments using shear-stress responsive nano-containers, an vitro model of the human circulatory system in the healthy and diseased state is developed using plastic model arteries connected to a heart pump designed for use in heart bypass surgery. The micrometre-resolution, three dimensional data from human coronary arteries gathered in Chapter 2.1 are invaluable for validating the morphology of these specifically designed plastic models of healthy and critically constricted arteries. Chapter 2.2 quantitatively compares the morphology of the plastic model arteries with a critically constricted human coronary artery and a murine model. Using the validated in vitro model and liposomes formulated from the artificial phospholipid Pad-PC-Pad, Chapter 2.3 presents the first proof-of-principle that mechano-sensitive nano-containers could be used in targeted drug delivery.

Lumen meshes extracted from the μCT datasets are required for computer simulations to truly understand the localised shear-stresses at play in atherosclerotic vessels. Further experiments to construct a micrometre-resolution shear-stress profile of a typical critically constricted vessel will allow predefined, physiologically relevant "breakpoint" shear-stresses to be determined, above which, the nanocontainers should become unstable and release their contents. Such optimised nano-container formulations could have far reaching implications for the treatment of cardiovascular diseases and beyond.

List of Publications

M. N. Holme, G. Schulz, H. Deyhle, T. Weitkamp, F. Beckmann, J. A. Lobrinus, F. Rikhtegar, V. Kurtcuoglu, I. Zanette, T. Saxer, B. Müller, "Complementary X-ray tomography techniques for histology-validated 3D imaging of soft and hard tissues using plaque-containing blood vessels as examples." *Nature Protocols*, **9**, 1401- 1415 (2014).

M. N. Holme, G. Schulz, H. Deyhle, S. E. Hieber, T. Weitkamp, F. Beckmann, J. Herzen, J. A. Lobrinus, F. Montecucco, F. Mach, A. Zumbuehl, T. Saxer, B. Müller, "Morphology of atherosclerotic coronary arteries." *Proceedings of SPIE*, **850609**, 8506 (2012).

B. Müller, G. Schulz, A. Mehlin, J. Herzen, S. Lang, **M. N. Holme**, I. Zanette, S. Hieber, H. Deyhle, F. Beckmann, F. Pfeiffer, T. Weitkamp, "Grating-based tomography of human tissues." *AIP Conference Proceedings*, **1466**, 107-112 (2012).

M. N. Holme, B. Müller, T. Saxer, A. Zumbuehl, "Shear stress as drug delivery trigger." *Chimia*, **66**, 715 (2012) (Polymers and Colloids highlight).

M. N. Holme, I. A. Fedotenko, D. Abegg, J. Althaus, L. Babel, F. Favarger, R. Reiter, R. Tanasescu, P.-L. Zaffalon, A. Ziegler, B. Müller, T. Saxer, A. Zumbuehl, "Shear-stress sensitive lenticular vesicles for targeted drug delivery." *Nature Nanotechnology*, **7**, 536-543 (2012).
(Highlighted in Y. Barenholz, "Nanomedicine: Shake up the drug containers", *Nature Nanotechnology*, **7**, 483-484 (2012).)

I. A. Fedotenko, **M. N. Holme**, R. Tanasescu, P.-L. Zaffalon, A. Zumbuehl, "Putting the P into phospholipids." *Chimia*, **65**, 859-862 (2012).

T. Saxer, A. Zumbuehl, B. Müller, I. Fedotenko, **M. N. Holme**, P.-L. Zaffalon, "Novel lipids and phospholipids, and compositions comprising them for pharmaceutical and cosmetic uses." *WO2012119781A2* (2012).

M. N. Holme, A. Zumbuehl, T. Saxer, B. Müller, "Shear Stress Sensitive Nanocontainers for Targeted Drug Delivery." *European Cells and Materials* **22**, Suppl. 4, 35 (2011).

1 Introduction

Cardiovascular diseases are the world's most prevalent diseases and number one cause of death [1], responsible for three in ten of all deaths globally in 2008 [2]. Atherosclerosis is characterised by a narrowing of the arteries, beginning with formation of fatty streaks on the artery walls that form lesions in which a lipid core expands, eventually leading to calcified plaques [3]. When these plaques rupture they partially or completely block the arteries causing heart attack. Vasodilators such as nitroglycerine are administered intra-venously to open the occluded arteries and increase blood perfusion in the surrounding heart muscle. This improves the patient's chance of survival and minimises the damage to the heart caused by ischemic hypoxia. However, the action of nitroglycerine is systemic and hypotension is a common side effect. Careful monitoring of the patient's blood pressure is required throughout administration and often doses must be adjusted or medication withdrawn altogether to avoid potentially fatal hypotension, before the desired vasodilatory effect at the heart is achieved. This problem could be overcome by using nano-container delivery vectors such as liposomes, to transport such drugs to the heart and release them preferentially at the site of constriction.

Liposomes in drug delivery

Liposomes are phospholipid bilayers with an internal aqueous compartment and are well-established nano-container vectors for targeted drug delivery, with several formulations currently on the market [4]. Whilst protecting encapsulated contents from chemical and biological reactions with outer surrounding media, liposomes also pose a hurdle for the release of any encapsulated therapeutic agents. Targeted delivery using liposomes can be achieved by both passive and active mechanisms. Naked liposomes are rapidly cleared from the body by the kidneys, however introducing a polyethylene glycol coating cre-

ates sterically stabilised "stealth" vesicles capable of circulating in the blood stream for hours or days [5–7]. The classical example of passive targeting uses the enhanced permeability and retention effect to target the leaky vascularisation of tumour tissue, whereby these long-circulating "stealth" liposomes preferentially accumulate around the tumour periphery over time. The first ever liposome formulation, marketed under the name Doxil in the USA and Cealyx in Europe, used this principle to improve efficacy and reduce side effects of the drug doxorubicin in the treatment of ovarian cancer [8–10].

Active targeting typically involves tethering ligands such as antibodies, peptides, folate or transferrin to the liposome surface, which then bind to specific biomarkers over-expressed in the target pathology (typically cancers) [4, 10–12]. Cationic liposomes have also attracted considerable attention as DNA transfection vectors in gene therapies [13–17]. Unfortunately, there are no reported biomarkers that are sufficiently specifically over-expressed in critically constricted arteries, which might be used for targeted delivery during myocardial infarction. This raises the question of using an alternative targeting mechanism, such as a physics-based trigger which takes advantage of the mechano-sensitivity of *de novo* designed nano-containers to the increased shear-stresses observed in diseased heart vessels.

Defining the morphology of critically constricted vessels

In order to optimise nano-container formulations with appropriate mechano-sensitivity to treat advanced cardiovascular disease, one must first define a) what the exact local wall shear stresses within a critically constricted vessel are, and how these compare to the common, healthy situation, and b) what is meant by a critically constricted vessel in terms of lumen morphology and tissue composition.

There are several computational fluid dynamics-based methods for calculating wall shear stresses in human coronary artery trees [18]. The arterial morphology on which these calculations are based is often acquired using in vivo methods such as ultrasound and magnetic resonance imaging. Pairs of coronary angiograms (measured using clinical CT) taken at different angles can also be used, and have been successfully employed in both steady-state and transient flow simulations in healthy coronary arteries [19, 20]. There are a few reports

of coronary flow simulations in the literature based on stenosed vessels. Rikhtegar and co-workers investigated the suitability of different wall shear stress parameters for predicting plaque location, based on coronary angiograph-derived models [21]. Katrisis and co-workers observed blood recirculation in stenoses greater than 90%, along with a significant flow reduction, the extent of which is governed by the stenosis' position in the arterial tree [22]. Using an arterial tree reconstructed in three dimensions from coronary angiograms, a 50% stenosis immediately before or after a bifurcation was also found to lead to recirculation as well as vortex formation, resulting in a stagnant flow [23]. However, such data is not available for critically constricted arteries because there are very few micrometre resolution images of such vessels, from which meshes can be extracted. Finally, it is also reported that the vulnerability of a plaque is governed predominantly by its structure and composition and not the degree of stenosis [24]. Therefore, to identify "culprit lesions" - plaques likely to rupture - it is essential to understand the local morphology, for example of soft tissues such as thrombus, collagen, fat and muscle, as well as hard tissues such as calcifications and the fibrous cap.

It is most common in the literature to report stenosis as the percentage of vessel occlusion by diameter. Although it is widely accepted that arteries with over 50% stenosis by diameter present significant stenosis and coronary artery disease [25–28], the majority of sites of plaque rupture are greater than 75% stenosed [29]. Occasionally, percentage stenosis by both diameter and cross-sectional area are reported simultaneously. For example, Virmani and co-workers report vulnerable plaques with 50% diameter stenosis in over 75% of cases, corresponding to 75% stenosis by cross-sectional area [30]. When these values are also quantified in absolute as opposed to relative values, the data become even more useful [31], since compensatory vessel wall remodelling could lead to unrepresentitavely small degrees of percentage stenosis observed by angiography [25].

Mean diameter stenosis of culprit lesions has been reported as $(83.8\pm 15.8)\%$ [32, 33]. However, there is growing and often conflicting data concerning the relationship between infarction type and percentage stenosis of culprit lesions. For example, Huang and co-workers reported a $(66.7\pm23.9)\%$ stenosis for non-ST elevated myocardial infarc-

tion (NSTEMI) and (78.6±21.2)% for ST-elevated myocardial infarction (STEMI) culprit lesions measured by 64-slice multi-detector computed tomography (64-slice CT) [34]. Manoharan and co-workers, on the other hand, used conventional coronary angiography to report an average diameter stenosis of (68.6±12)% in patients presenting STEMI versus (71±12)% for NSTEMI, corresponding to a minimal lumen diameter of 0.9±0.4 and 0.7±0.4 mm respectively [35]. Although both studies claim to have found that a particular infarction type leads to an increased stenosis in culprit lesions, the errors in both studies are so large that the only statistically significant conclusion to be drawn is that both STEMI and NSTEMI lesions occur over a broad and overlapping range of stenoses. Evidence suggests that the method of measurement has an effect on the measured constriction, with multi-slice CT overestimating the percentage diameter stenosis in calcified plaques (by 11%) but underestimating it in the case of non-calcified plaques (by 7%), when compared with pathohistology [36]. Although it provides 3D data, when compared with coronary angiography the 64-slice CT is reported to be an inaccurate tool for predicting the percentage stenosis [37].

Clearly, the characterisation of "culprit lesions" is non-trivial. Arteries in this thesis are characterised both by percentage stenosis by cross sectional area (to conform with the literature) and also minimum cross-sectional area (Chapters 2.1 and 2.2). This second quantity is more relevant for predicting the required "break points" of mechano-sensitive formulations for localised drug delivery. Other quantities commonly seen in the literature, such as percentage stenosis by diameter, can be calculated from the percentage stenosis by cross sectional area (assuming a circular cross-sectional area).

Micro computed tomography

Visualisation and characterisation of human coronary arteries to diagnose and monitor disease progression is an extensively studied area of medicine [38, 39]. In the clinic, conventional coronary angiography is the method of choice, with multi-slice CT angiography [40], magnetic resonance imaging (MRI) [28, 41] and echocardiography [42] completing the clinician's toolbox. However, these techniques only achieve resolutions of hundreds of microns and provide limited differentiation

between tissue types [24, 43]. The gold standard of ex vivo imaging is histology, which characterises the 2D morphology and tissue composition of ex vivo arteries down to the sub-micrometre level, with the resolution in the third dimension limited only by slice thickness. However, due to its anisotropic nature, the cutting process leads to strain and pleat deformations in the 2D data, and since histological slice preparation is a very lengthy process it is practically unfeasible to prepare enough consecutive slices to build micrometre-resolution 3D datasets.

Laboratory micro computed tomography (μCT) in absorption contrast mode is a convenient, non-destructive technique that provides the required 3D spatial resolution in the sub-micrometre range. It is ideally suited to simple cases, for example teeth fixed in formalin where the attenuation values of the individual components are well-discretised [44]. In contrast to laboratory μCT, which typically uses cone beam-emitting X-ray sources, synchrotron radiation-based μCT (SRμCT) provides such a high photon flux that, using a monochromator, a monochromatic beam with a reasonable photon flux and improved spatial coherence and density resolution can be generated [45, 46], and beam hardening is avoided. SRμCT has been used successfully to, for example, correct for deformations induced during histology [47] and detect ganglion cells (with the aid of a contrast agent) [48] where laboratory systems could not.

Both the above methods are examples of absorption-contrast based imaging, which measures the distribution of local X-ray linear attenuation coefficients. For X-rays of given wavelength λ, the complex refractive index distribution of a specimen can be expressed as

$$n(x, y, z) = 1 - \delta(x, y, z) + i\beta(x, y, z). \tag{1.1}$$

While the real part, δ(x,y,z), describes the phase shift (see page 6), the imaginary part, β(x,y,z), describes the X-ray absorption within the specimen. This quantity in turn is related to the linear attenuation coefficient, μ, measured in absorption-based μCT, by

$$\mu(x, y, z) = \frac{4\pi}{\lambda} \cdot \beta(x, y, z). \tag{1.2}$$

In such a setup, the minimum scan time for a given ratio of sensitivity

to resolution is given when the equation;

$$\mu \cdot D = 2 \tag{1.3}$$

is satisfied, where D the diameter of a homogeneous, cylindrical specimen and μ is inversely proportional to the cube of the optimal photon energy. Therefore, optimal photon energy is very sensitive to the specimen's thickness, density and chemical composition, and it is impossible to select a single photon energy that provides optimal radiographs of specimens containing both highly X-ray absorbing plaque and water-dominated soft tissues [49, 50].

An alternative to absorption-based μCT is to calculate the phase shift of the X-rays as they pass through the specimen (based on measureing the first or second derivitive of the phase shift). Whereas absorption-based methods measure the imaginary part of the refractive index, phase contrast-based SRμCT (phase SRμCT) measures the real part, δ, which is linearly proportional to the inverse of the photon energy. It is therefore much less dependent on elemental composition of the specimen, and is the method of choice for imaging samples that contain both soft and hard tissues. Several phase tomography methods are available today, based on reconstructing the phase shift or decrement of the phase shift [51–56]. This study uses the recently developed grating-based interferometry, which detects deflection angles of the X-rays once they pass through the specimen [57, 58]. Since these angles are in the sub-microradian range, a beam-splitting and analyser grating are used in a phase-stepping setup to simultaneously yield data on the phase shift and attenuation values, as in absorption-SRμCT.

Studies using this grating interferometry setup have successfully investigated the micro-structures of the human cerebellum, visualised individual Purkinje cells without the need for a stain or contrast agent [46], and corrected for deformations incurred during histology [59]. Here, Chapter 2.1 presents one of the first studies that uses grating-based phase-SRμCT to visualise human coronary arteries, which unlike human brain contain a mixture of soft and hard tissues.

Measurements of critically constricted human coronary arteries

The first part of this thesis deals with the development of a protocol for screening a library of human coronary arteries. Using sequential

μCT techniques, this protocol enables the user to differentiate between the plaque, muscle and fat tissues without the use of a contrast agent, and to determine the 3D morphology down to the micrometre scale [60].

It is designed to evaluate the morphological characteristics of a stenosed vessel, with particular reference to the tissue type and microstructure of the lumen. Phase-SRμCT, in combination with histology, provides details about the different tissues present, whereas absorption-SRμCT is more appropriate for lumen segmentation and subsequent flow simulations due to its smaller pixel size and differing sources of artifacts between the two measurement modalities [61].

Before any measurements can be made, the specimen must be suitably prepared. One of the most important steps is the selection of suitable sections of artery for imaging. This can be done by consulting medical records of the donor, visual inspection and manually feeling for the presence of plaques and obstructions. The specimen must then be extracted, cut to an appropriate size (2 to 3 cm length) and fixed in formaldehyde. Subsequent embedding in paraffin makes it easier to transport the specimen and accurately identify areas from the 3D datasets for histological sectioning, to within fractions of a millimetre. However, the paraffin embedding process is not without its drawbacks and can lead to lumen deformation and encapsulation of air bubbles (particularly problematic for phase-SRμCT where the sharp change in decrement of the refractive index between air and the paraffin causes starburst artifacts).

Once five arteries had been appropriately prepared, a Skyscan 1174 setup for bench-top μCT (Skyscan 1174 compact micro-CT, Bruker microCT, Kontich, Belgium) was used to select three arteries presenting advanced atherosclerosis. Measurement of these arteries in absorption-SRμCT (Beamline W2, HASYLAB, DESY, Hamburg, Germany) made it possible to additionally visualise the surrounding muscle but not the vessel wall and fatty tissues. This is a problem intrinsic to the imaging modality, where the optimal X-ray energy is different for hard and soft tissues. Too low an energy, and the photon statistics are insufficient due to the highly X-ray absorbing species. Too high an energy and there is loss in sensitivity for differentiation within the soft tissues. To better visualise the soft tissues, the most promising artery

was decalcified to remove the highly X-ray absorbing species, then
re-measured using a lower energy incident X-ray beam and otherwise
identical experimental setup. The lumen morphology could be seg-
mented from this absorption-SRμCT data and was extracted for use
in flow simulations. A region-growing algorithm (Region Growing tool,
VGStudio Max 2.1, Volume Graphics GmbH, Heidelberg, Germany)
was used, since segmentation by thresholding was not possible due
to overlapping attenuation-related values in the intensity distribution,
and the lumen surface was too complex for a feature-based method.
Starting from a selection of seed points, neighbouring voxels within
a fixed intensity range were added to the lumen region of interest
[62]. Flow simulations, conducted in collaboration with PhD-student
F. Rikhtegar of the Kurtcuoglu group at ETH Zurich, calculated wall
shear stresses of over 18 Pa at the site of critical constriction, and less
than 3 Pa elsewhere.

Although the absorption-SRμCT data was ideal for extracting infor-
mation concerning the lumen morphology, it was insufficient for iden-
tification of different soft tissue types. However, it was possible to
distinguish between different tissue types using phase-SRμCT data
(Beamline ID19, ESRF, Grenoble, France) from the same decalcified
artery. Specifically, it was possible to distinguish between muscle,
decalcified plaque and fat using thresholding after visual comparison
with the "gold standard" of 2D analysis, i.e. appropriately stained his-
tological slices. This protocol allows identification of the morphology
and tissue composition of human explanted human coronary arteries
down to the micrometre scale, and could also be applied to other hard
and soft tissue-containing specimens.

A model critically constricted artery

In order to test the suitability of liposome formulations for shear-stress
induced release of a drug, in vitro flow experiments with suitable model
arteries and physiological flow conditions were required [63]. The Swiss
company Elastrat, a supplier of cardiovascular models for training
medical students, was commissioned to design such models for this
purpose, fabricated from polymethylmethacrylate (PMMA). In order
to assess how closely the in vitro results mimic the real, in vivo situa-
tion, it is absolutely essential to quantitatively compare the morpholo-

gies of the models with real, critically constricted, human coronary arteries. An advanced laboratory μCT setup (Phoenix|x-ray, GE Sensing & Inspection Technologies GmbH, Wunstorf, Germany) was used in this study to measure a) a PMMA critically constricted and healthy model artery and b) a decalcified human coronary artery embedded in paraffin after formalin fixation. Since the attenuation-related values of the PMMA medium and surrounding air were easily discretised, a simple histogram-based thresholding method was used to segment the vessel lumen morphology [64]. The human coronary artery again required a more complicated region-growing algorithm to extract the lumen morphology, due to the overlapping attenuation-related values in the intensity distribution (Region Growing tool, VGStudio Max 2.1, Volume Graphics GmbH, Heidelberg, Germany).

Additionally, the use of a murine model was also considered. The explanted aorta of an APO E knock-out mouse, bred to present atherosclerosis, was measured using grating-based phase-SRμCT (Beamline BW2, HASYLAB, DESY, Hamburg, Germany). This imaging method was selected after an initial unsuccessful attempt to visualise the lumen with the advanced laboratory μCT set-up, where the attenuation-related values of the tissue and formalin fixation media overlapped extensively, leading to incomplete lumen visualisation, and failure to segment of the lumen morphology. Finally, the total cross-sectional area and percentage constriction of all three arteries was calculated.

The diseased human artery possessed an $(85.2\pm5)\%$ maximum constriction by cross sectional area versus $(81.8\pm5)\%$ in the related PMMA model. Assuming a circular cross-section, this corresponds to a minimum radius of 0.51 and 0.61 mm, respectively. The critically constricted PMMA model had a morphology with similar characteristics to the studied human coronary artery, and was therefore a valid tool for identification of nano-container formulations suitable for clinical studies. It was used for shear-stress induced release studies, published in Nature Nanotechnology (Chapter 2.3). The mouse aorta however, unlike in the human coronary arteries studied, presented no significant constrictions and no calcifications were observed, with only the muscle of the vessel wall distinguishable from the surrounding formaldehyde medium. The aorta was smaller than the human coronary artery measured, with a maximum cross-sectional area of 0.37 mm^2 com-

pared to the human coronary artery maximum cross-sectional area of 5.60 mm^2. With a maximum 50% constriction by cross-sectional area, corresponding to 0.27 mm^2 cross-sectional area, the mouse aorta morphology represented a 96% constriction of a 2.5 mm diameter human coronary artery. However, the constriction in the mouse aorta was due to the tapering of the artery from the proximal to distal direction and not any underlying pathology, and unlike a typical diseased human coronary artery it had a smooth morphology. Finally, the representative 96% constriction is slightly higher than desired for testing the suitability of shear-stress sensitive nano-containers.

Shear-stress sensitive liposomes for drug delivery

The final part of this thesis deals with formulating and testing shear-stress sensitive liposomes using PMMA model arteries with morphologies corresponding to a critically constricted and healthy coronary artery. There is sparse literature precedence for such mechano-sensitive delivery vectors. Almost 20 years ago, Giorgio and Chakravarthy observed that calcium ion permeability of phosphatidylcholine liposomes was greatly increased when increasing shear stresses within the range of the mammalian cardiovascular system [65]. Addition of cholesterol, known to stabilise PC bilayers through hydrocarbon-region interactions, decreased this effect [66]. It was not until ten years later that the subject resurfaced in a paper by Bernard and co-workers [67], who found that shear rates in excess of 5,000 s^{-1} led to an increase in permeability and fusion in 50 to 400 nm-sized EggPC large unilamellar vesicles. Doping with 1 mol% of the surfactant Brij S10 or increasing the shear rate increased their permeability. However, the shear stresses and timescales required for appreciable release of encapsulated contents were several orders of magnitude higher than those needed for the in vivo application presented in this thesis. Although this basic study was far removed from the clinical aim of the current work, the formulation was taken as a reasonable starting point for further experiments.

Liposomes with a 100 nm diameter were formulated from EggPC doped with the surfactant Brij S10 (0-1 mol%), using the well established extrusion method reported by Olson and co-workers [68]. They were loaded with an aqueous buffer containing the fluorophore

5(6)-carboxy-fluorescein at a self-quenching concentration (50 mM) [69]. When released from the liposomes, the carboxyfluorescein is diluted by the external medium to sufficiently low concentrations that it is no longer self-quenching and produces a bright fluorescence signal, the intensity of which is linearly proportional to the extent of release. The assay thus represents a simple but powerful model to quantify the release of encapsulated contents from a nano-container.

The formulated liposomes were subjected to in vitro shear stresses under haemodynamic flow conditions using the PMMA models of critically constricted and healthy coronary arteries. An extracorporeal circulation pump simulated the heart (Medtronic Bio-Pump, Bio Console 540, Minneapolis, MN, USA, used in coronary bypass and aortic valve replacement surgery). The shear stress in each arterial model was calculated as within reported physiological ranges. The optimal concentration of Brij S10 for shear-stress induced release was observed at 0.6 mol%. It led to high differences in fluorescence release between the healthy and critically constricted PMMA model arteries over long circulation times. Specifically, 14% more of the total concentration of encapsulated carbxyfluorescein was released after 40 passes through the critically constricted than the healthy artery PMMA model. At Brij S10 concentrations of zero and 1% there was no appreciable difference in release between the diseased and healthy artery models, although the 1% Brij S10 formulation was intrinsically less stable on the bench.

The relation between vesicle shape and stability has historically received only minor attention. Lenticular vesicles with large bending moduli have been computationally predicted to be more susceptible to mechanical stress than their spherical analogues [70] but this has yet to be shown experimentally. Thanks to its unusual chemical structure, the artificial phospholipid Pad-PC-Pad [71] was found to form lentil shaped vesicles [63]. Unlike natural phospholipids, the hydrophobic tails are attached to the glycerol backbone using amide linker functionalities. Additionally, the tails are attached in the 1,3 configuration compared to the 1,2 configuration seen in natural counterparts. This increases the spacing between the tails, leading to an unfavourably high-energy state, which is probably stabilised by interdigitation between the membrane bilayer leaflets. The interdigitation leads to a

higher Young's modulus in the bilayer, forcing liposomes to form with domains of lower curvature and point or edge discontinuities in the crystal structure, giving lenticular shapes. In comparison with their EggPC/Brij S10 analogues discussed above, Pad-PC-Pad liposomes demonstrated a much clearer distinction between release in the healthy and critically constricted artery models; the critically constricted PMMA artery model led to 25% more release of the total concentration of encapsulated carboxyfluorescein than the healthy PMMA artery model after *only one pass.* Finally, liposomes containing mixtures of Pad-PC-Pad and EggPC became unstable, or leaky, with an increase in Pad-PC-Pad concentration, but did not significantly increase their susceptibility to shear-induced release. Indeed, there was no statistically significant increase in release after one pass through either the healthy or critically constricted model.

Ideally, a mechano-sensitive nano-container for shear-stress triggered drug delivery should release 100% of the encapsulated drug on the first pass through a constricted vessel, but none in the healthy vascular system. Although this was impossible with the reported formulation, a significant preferential release (i.e. 25% increased release after one pass through an 85% constricted vs. healthy model) could still drastically improve patient prognosis. Finally, since the publication of these results, Korin and co-workers [72] reported the use of a different nano-construct that also utilises the elevated shear-stresses in constricted arteries for a physics-based, targeted drug delivery. Micrometer-sized aggregates of poly-lactic-co-glycolic acid were shown to break down to their individual nano-particle components under shear-stress conditions corresponding to a 60% constricted coronary artery. These nano-particles were then coated with tissue plasminogen activator (tPA), a protein involved in breaking down blood clots, and administered intravenously to in vivo murine pulmonary embolism models. Here, they were able to dissolve clots as effectively as a one-hundred-times more concentrated solution of free tPA. At last, physics-based delivery vectors are under the radar.

2 Results

2.1 A systematic protocol using multi-model micro-computed tomography for uncovering the morphology and tissue composition of critically constricted human coronary arteries

A sequential protocol using laboratory then synchrotron radiation-based μCT in absorption and phase contrast mode resolves the morphology and tissue composition of the soft and hard tissue-containing human coronary arteries with micrometre precision.

Absorption-SRμCT can be used to extract the lumen morphology for subsequent flow simulations. Phase-SRμCT, by comparison with histology, can be used to identify different soft tissues. Understanding the morphology and tissue composition of critically constricted arteries is essential for subsequent flow experiments to test the suitability of mechano-sensitive nano-containers for targeted drug delivery.

Published in Nature Protocols

Complementary X-ray tomography techniques for histology-validated 3D imaging of soft and hard tissues using plaque-containing blood vessels as examples

Margaret N Holme[1], Georg Schulz[1], Hans Deyhle[1], Timm Weitkamp[2], Felix Beckmann[3], Johannes A Lobrinus[4], Farhad Rikhtegar[5], Vartan Kurtcuoglu[6], Irene Zanette[7,8], Till Saxer[4] & Bert Müller[1]

[1]Biomaterials Science Center (BMC), University of Basel, University Hospital Basel, Basel, Switzerland. [2]Synchrotron Soleil, Gif-sur-Yvette, France. [3]Institute of Materials Research, Helmholtz-Zentrum Geesthacht, Geesthacht, Germany. [4]University Hospitals Geneva, Geneva, Switzerland. [5]Laboratory of Thermodynamics in Emerging Technologies, ETH Zurich, Zurich, Switzerland. [6]The Interface Group, Institute of Physiology, University of Zurich, Zurich, Switzerland. [7]European Synchrotron Radiation Facility, Grenoble, France. [8]Physik-Department, Technische Universität München, Garching, Germany. Correspondence should be addressed to B.M. (bert.mueller@unibas.ch).

A key problem in X-ray computed tomography is choosing photon energies for postmortem specimens containing both soft and hard tissues. Increasing X-ray energy reduces image artifacts from highly absorbing hard tissues including plaque, but it simultaneously decreases contrast in soft tissues including the endothelium. Therefore, identifying the lumen within plaque-containing vessels is challenging. Destructive histology, the gold standard for tissue evaluation, reaches submicron resolution in two dimensions, whereas slice thickness limits spatial resolution in the third. We present a protocol to systematically analyze heterogeneous tissues containing weakly and highly absorbing components in the original wet state, postmortem. Taking the example of atherosclerotic human coronary arteries, the successively acquired 3D data of benchtop and synchrotron radiation–based tomography are validated by histology. The entire protocol requires ~20 working days, enables differentiation between plaque, muscle and fat tissues without using contrast agents and permits blood flow simulations in vessels with plaque-induced constrictions.

INTRODUCTION

Atherosclerosis is the leading cause of death worldwide[1]. An understanding of the changes in 3D vessel morphology as the disease develops provides insights into its relationship with blood flow, which is essential for oxygen and nutrient supply and waste removal. Specifically, the determination of the generic clinical morphology of critically stenosed arteries is a key topic of cardiological and vascular research. Flow simulations based on high-resolution 3D data sets of real human coronary arteries provide in-depth information on physical parameters such as wall shear stress in healthy and diseased vessels[2]. A tenfold increase in shear stress is reported in critically stenosed arteries compared with their healthy counterparts[3]. Recently published proof-of-principle studies are based on using this physical parameter to trigger the release of vasodilatory and thrombolytic drugs[4,5]. The precise morphological knowledge of the generic atherosclerotic plaque is necessary to determine the shear stresses at calcified stenoses in comparison with the healthy arteries in order to tailor the targeted drug release.

Advantages and limitations of histology in the analysis of heterogeneous tissues

It is widely accepted that histology is the gold standard for tissue characterization down to the submicrometer level. In this technique, only the wavelength of the applied light limits the spatial resolution of the 2D light microscopy images. More importantly, resolution in the third dimension, which can be obtained through the preparation of serial sections, is restricted to tens of micrometers. As the diseased arteries contain hard- and soft-tissue components, slicing

paraffin-embedded arteries is problematic and the resulting slides are generally afflicted with preparation artifacts. Such serious artifacts change the lumen cross-sectional area[6] and render the data useless for subsequent blood flow analysis. To optimize the cutting strategy, the histologist should know the local arrangement of the soft- and hard-tissue components. This knowledge can principally be gained from X-ray tomography[7], but the tissue inhomogeneity gives rise to deficiencies in the tomograms such as streak artifacts, which excessively complicate the procedure. As a result, specimens containing both soft and hard tissues are difficult to cut and are therefore regularly decalcified before slicing. However, the decalcification procedure induces heterogeneous strain[8] and hence a modification of the vessel morphology.

Nondestructive 3D X-ray imaging

Benchtop micro computed tomography (μCT) and synchrotron radiation–based micro computed tomography (SRμCT) reach true micrometer resolution, although the resolution usually remains inferior to that of histology[9]. SRμCT provides better contrast and better contrast-to-noise ratio than benchtop systems[10], and it has already been used, for example, to correct deformations induced during histological sectioning[11]. The absorption contrast between different soft tissues is, however, rather weak, which makes simultaneous visualization of hard and different soft tissues very challenging. To obtain improved soft-tissue contrast, SRμCT in phase-contrast mode can be used[12,13]. X-ray phase-contrast methods generate image signal from variations of the decrement δ of the X-ray refractive index distribution in

2.1 A systematic protocol using multi-model micro-computed tomography for uncovering the morphology and tissue composition of critically constricted human coronary arteries

15

| PROTOCOL

Box 1 | Differences in the information extracted from tomography measurements in absorption- (conventional) and phase-contrast modes

The complex refractive index distribution of an object for X-rays of given wavelength λ is usually written as follows:

$$n(x, y, z) = 1 - \delta(x, y, z) + i\beta(x, y, z)$$

The X-ray absorption within the object is described by the imaginary part $\beta(x,y,z)$, which is related to the widely used linear X-ray attenuation coefficient $\mu(x,y,z)$ by

$$\mu(x, y, z) = \frac{4\pi}{\lambda} \cdot \beta(x, y, z)$$

Absorption-contrast CT. The retrieved data in absorption-contrast SRμCT measurements is the distribution of local linear X-ray attenuation coefficients for the given X-ray energy.

Phase tomography. In phase-contrast imaging, the signal is generated from the real part of the X-ray refractive index of the specimen. As this real part is generally very close to 1, it is usually described by its deviation from unity, the decrement δ. Its spatial distribution $\delta(x,y,z)$ is directly related to the electron density distribution $\rho_e(x,y,z)$ of the object by the equation

$$\delta(x, y, z) = \frac{r_e \lambda^2}{2\pi} \rho_e(x, y, z)$$

with the classical electron radius r_e (ref. 68). Most of the phase-tomography measurements are, however, based on the first or second derivative of the phase shift and thus require procedures to calculate the local decrements of the refractive index (phase retrieval).

---

the specimen (**Box 1**). A variety of phase-contrast tomography methods are available today[14–19]. Phase-contrast methods that are used to retrieve the real part of the refractive index are referred to as phase tomography. More recently, phase tomography based on X-ray grating interferometry (XGI phase tomography, herein XGI phase SRμCT) was developed[20,21]. This method detects minute deflection angles of the incoming X-rays that pass through the sample, which are proportional to the first derivative of the phase shift. It reaches the particularly high contrast required for identifying structures with tiny differences in electron density[22–24].

Overview of the protocol
This protocol enables the user to differentiate between the plaque, muscle and fat tissues present within diseased arteries without the use of a contrast agent and to determine the 3D morphology down to the micrometer scale. By using a combination of nondestructive hard X-ray imaging techniques, it allows a detailed analysis of the 3D morphology of atherosclerosis-presenting human coronary arteries, including identification of plaque-containing arteries (SkyScan 1174 benchtop μCT), characterization of the lumen morphology (absorption SRμCT) and the quantification of the amount of the anticipated tissue types such as plaque, muscle and fat, and their X-ray phase shifts (XGI phase SRμCT). The results are validated by selected subsequently prepared histological slides.

This protocol was designed to evaluate the morphological characteristics of a stenosed vessel, with particular reference to the tissue type and the microstructure of the lumen. By using a SkyScan 1174 setup for benchtop μCT, the most appropriate stenosed arteries from all available human specimens was selected for absorption and XGI phase SRμCT measurements. Measurements using absorption SRμCT allowed us to calculate a maximum of 75% stenosis by cross-sectional area. This protocol has also been

used to identify the morphology of a critically stenosed artery (>80%; ref. 7). Images obtained using XGI phase SRμCT allowed different soft-tissue types to be identified. The data obtained were validated by comparison with the gold standard of 2D analysis, i.e., appropriately stained histological slides.

Comparing the equipment setup for the CT methods used in this protocol
Equipment setup (**Fig. 1**) for all μCT methods includes the basic elements of an X-ray source, a specimen on a high-precision manipulator and a detector. Whereas benchtop μCT uses a polychromatic cone beam, the beam in SRμCT is essentially parallel and usually monochromatized. As the parallel beam implies that the X-ray image is not geometrically magnified before detection, detectors in SRμCT setups usually have a smaller pixel size than benchtop methods.

In addition to these basic elements, XGI phase-contrast setups include two gratings between the specimen and detector. These gratings are used in a phase-stepping regime, in which the beam splitter grating (G_1) is moved laterally relative to the analyzer grating (G_2) to quantify minute deflections of the X-ray beam due to refraction in the sample (**Fig. 2**). In benchtop XGI phase-contrast (not used in this protocol), usually an additional grating between the X-ray tube and the sample is needed to fulfill the beam coherence requirements.

CT for the determination of tissue composition and morphology
In our recent published work[7], we used absorption-contrast SRμCT to extract a 3D mesh of tessellated 2D polygons representing the surface of the artery lumen. Such surface meshes generally form the basis for flow simulations to calculate wall shear stresses in human coronary arteries[25]. However, the most important factor in the determination of pathogenesis of acute coronary
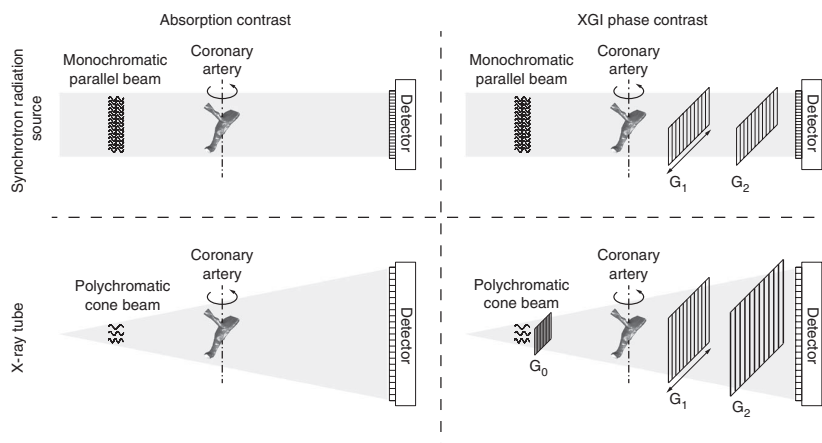
Figure 1 | Schematics of setups for μCT imaging.

syndromes is the structure and composition of the atherosclerotic plaques, rather than the extent of stenosis[26]. The likelihood of a plaque rupturing (its vulnerability) depends on its tissue structure. To understand the vulnerability of a plaque, it is essential to understand the local morphology, for example, of soft tissues such as thrombus, collagen, fat and muscle, as well as hard tissues such as calcifications and the fibrous cap. It is often impossible to image the individual tissue types within an *ex vivo* coronary artery by using benchtop μCT, which only allows differentiation between three tissue types, i.e., calcified atherosclerotic plaques, fat tissue and mixed tissue.

In clinical imaging, multidetector-row computed tomography (MDCT) with barium sulfate contrast agent has been used to attempt to differentiate calcified and noncalcified plaques[26]. Artifacts can occur owing to extreme calcifications or incomplete filling of arteries with contrast medium. Other methods are available, such as dual-source CT scanners, which permit simultaneous scanning at two peak X-ray energies. The combination of images obtained at two acceleration voltages allows marked improvement in the identification of anatomical structures compared with conventional lab-based CT[27].

For imaging tissues with prominently varying degrees of mineralization, XGI phase tomography is becoming an indispensable tool because of its combination of high soft-tissue contrast with microscopic resolution in full 3D[28]. As with other CT techniques, subsequent correlation with histology is possible and can help interpret the tomography images. In this protocol, we use XGI phase tomography on a synchrotron radiation source. This technique has been demonstrated to be compatible with conventional X-ray sources[29], and recently results from a preclinical scanner based on this principle were reported[30].

Our group has used both XGI phase SRμCT and absorption-based μCT to visualize a variety of anatomical structures[7,22,28,31–34]. Herzen *et al.*[35] showed that XGI phase SRμCT can be used to

visualize the microstructure of urethra, in which absorption-contrast SRμCT was not sensitive enough to detect differences between the absorption values within the tissues and the surrounding fluid (formaldehyde). In 2010, XGI phase and conventional absorption SRμCT setups similar to the ones reported here were used to investigate the microstructures of the human cerebellum, and to visualize individual Purkinje cells without the need for a stain or contrast agent[22].

Multimodal data registration
Techniques to register data sets can be broadly broken down into two approaches, namely intensity- and feature-based algorithms. The inherent dimensionality reduction ability of feature-based techniques makes them suitable for large data sets. However, matching features between data sets obtained from different imaging modalities is frequently nontrivial, and in these cases intensity-based registration that relies on the classical maximization of mutual information is often more suitable[36,37]. Affine and nonrigid registration algorithms can, for example, provide information on the effects of global volume change and local strain field of the human brain during extraction and formalin fixation of the whole brain, by using data sets that are acquired via MRI[38]. These registration methods can, in some cases, also be used to compare 3D SRμCT images with 2D histological slices[11,39]. In particular, these registrations facilitate the correction of artifacts such as the formation of pleats during the preparation of histological slides. Indeed, further studies found that XGI phase SRμCT followed by histological slide preparation could lead to improvements in the accuracy of stereotactic brain atlases used for noninvasive MR-guided neurosurgery[32]. Similarly, 3D μCT data sets have been used to select appropriate representative histological slices for the analysis of bone augmentation materials in human mandibles. Subsequent registration of the 3D μCT data sets with 2D histological slices allowed 2D histograms to be plotted,
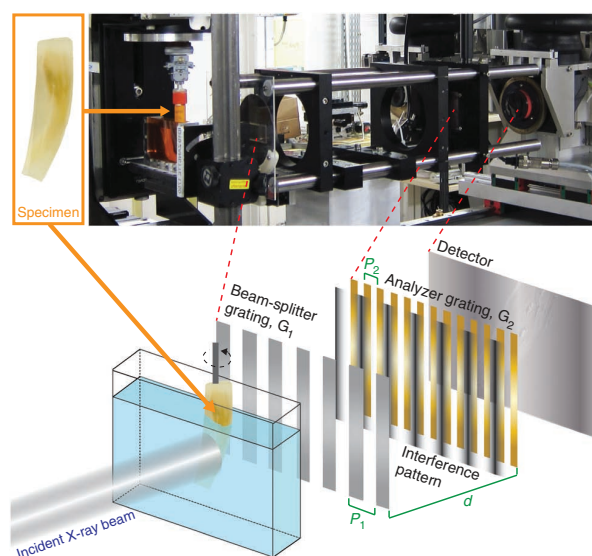
Figure 2 | XGI phase SRμCT setup at ESRF. From left to right, along the incident X-ray beam; sample holder, phase grating (beam-splitter grating, G_1; periodicity, P_1), absorption grating (analyzer grating, G_2; periodicity, P_2) and detector. The distance d between G1 and G2 is chosen for optimum tradeoff between contrast and resolution. The reconstructed value is the difference ($\Delta\delta$) between the real part of the refractive index in the sample (δ) and surrounding water bath (δ_{water})[22].

2.1 A systematic protocol using multi-model micro-computed tomography for uncovering the morphology and tissue composition of critically constricted human coronary arteries

17

| PROTOCOL

which were used to identify anatomical features that cannot be identified by histology or μCT alone[39].

The protocol presented here has been used to extract information from multimodal imaging techniques about both the morphology and tissue composition of atherosclerotic human coronary arteries[7], which, unlike human brain and teeth, contain a mixture of soft and hard tissues.

Determination of the lumen of the diseased vessels
To determine the actual lumen of vessels (i.e., shape and cross-section), staining agents such as iodine compounds and barium sulfate emulsions have been successfully applied[40–43]. The reliable application of such staining agents for human tissues, especially for the smallest capillaries, however, has not yet been demonstrated. In addition, the pressure applied to fill the vessels with staining agent can deform the inhomogeneous, diseased walls or even lead to unintentional leakage of the medium. Therefore, such an additional preparation step should be avoided whenever possible.

Pai *et al.*[44] have shown that osmium tetroxide (OsO_4) as a staining agent to image artery walls of mice is reasonable even when applying conventional X-ray sources. This approach has excellent potential, as the agent binds to the lipids that are responsible for the plaque formation, so that even early stages of plaque formation are assessable. Unfortunately, the spatial resolution of both the conventional and the synchrotron radiation–based setups was ~10 μm, which is more than one order of magnitude larger than the wall thickness of capillaries in mice and only slightly smaller than the ~50-μm wall thickness of the largest arteries. As a result, only very few vessels with a restricted number of bifurcations were identified. Therefore, the 3D images had restricted quality, and any quantification of the morphology of stenosed arteries via this approach, such as changes in the cross-section along the individual vessel, has to be regarded as questionable. Furthermore, OsO_4 is highly toxic and, if possible, it is preferable to avoid handling this and other toxic compounds. Finally, it is unclear to what extent the application of OsO_4 gives rise to local deformations caused by nonhomogeneous shrinkage of the soft tissues, which can markedly influence the quantification of the lumen morphology.

Segmentation of morphological features
In this protocol, the lumen morphology is segmented from the absorption SRμCT data set and extracted for use in flow simulations. In biomedical image segmentation, histogram-based methods are very efficient when the intensity distribution allows the choice of appropriate thresholds[45]. When the intensities of the local absorption values overlap substantially, more sophisticated approaches are required, such as feature-based and region-growing algorithms. Feature-based approaches detect objects by their characteristic structure; for example, the Frangi filter identifies vessels by their tubular structure[46]. A region-growing algorithm adds neighboring voxels within a range of intensity to an object starting from a selection of seed points[47]. In this study, the arteries are segmented well by using region growing, whereas thresholding leads to insufficient results and the lumen surface is too complex for a feature-based method.

Experimental design
Specimen preparation. Before the tomography measurements, the specimens must be appropriately prepared. This involves extracting up to the entire coronary artery tree from a donated heart, carefully selecting a suitable section of coronary artery, removing surrounding tissue, fixing the specimen in formaldehyde, and subsequently selecting appropriate embedding material (paraffin, formaldehyde or polymer resins) and containers for storage and measurement. In addition to calcified, diseased arteries, healthy specimens may also be selected for comparison. Further preparatory steps are required if the sample needs to be decalcified, e.g., for the histological sectioning. The decalcification process dissolves hard-tissue components, which in this case is plaque; this is an essential step before cutting histology slices. Decalcification is also often beneficial for the μCT imaging. It allows the use of lower photon energies, and it therefore provides increased contrast between soft-tissue components at the cost of losing information about the hard tissues dissolved during the process.

Preparation for beamline measurements. Once the specimen is prepared, it must be transported to the beamline. This often involves the crossing of international borders, which requires necessary legal paperwork with related administrative procedures and delays. For the tomography measurements, the samples are usually glued to a sample holder and fixed on a high-precision manipulator. These preparatory steps are extremely important, and they must not be overlooked. Inappropriate specimen preparation can lead to severely decreased image quality.

Data acquisition. The necessary beamtime correlates with the selected photon energy. In conventional, absorption-based μCT, the minimum scan time for a given ratio of sensitivity to resolution is given when the equation $\mu \cdot D = 2$ is satisfied, where μ is the linear X-ray attenuation coefficient (**Box 1**) and D is the specimen diameter[48]. Between absorption edges, μ is inversely proportional to the cube of the photon energy. The optimal photon energy therefore varies with thickness, density and chemical composition of the sample. For example, by assuming a cylinder that is 1 cm in diameter, the above equation is satisfied when $\mu = 2$ cm^{-1}, which occurs at 14 keV for a water-only specimen, but 100 keV for an iron-only specimen. Therefore, it is impossible to select a single photon energy that provides optimal radiographs of specimens containing highly X-ray-absorbing plaque and water-dominated soft tissues[48,49].

Phase tomography yields the real part of the refractive index relative to the surrounding medium ($\Delta\delta$) (**Box 1**). This part of the refractive index is linearly proportional to the inverse of the photon energy. It is also much less dependent on the elemental composition of the specimen than the imaginary part. As a consequence, phase tomography is much more suitable for differentiating between different soft tissues in the presence of hard tissues.

The image quality is a function of the exposure time. The detector normally has a 12–14-bit (i.e., 4,000:1–16,000:1) dynamic range—i.e., a ratio of maximum signal to noise. The initial exposure time is set before the recording of the radiographs starts. To ensure an optimized photon density in each radiograph, algorithms compensate for temporal modulations in the X-ray beam. To maximize the contrast between soft-tissue components, it is preferable to use the full dynamic range of the detector.

The quality of the tomography data depends on the number of acquired projections. The 3D data are reconstructed from a series of radiographs, which today are usually ~1,000, taken at

fixed incremental angles of rotation. The number of projections for best resolution of a specimen with diameter *D* is intrinsically linked to the number of detector pixels along *D*. Assuming a symmetrical rotation center, the displacement between the corresponding image features in neighboring radiographs is dictated by the angular increment and maximal distance from the rotation center. Sampling theory stipulates that the number of required radiographs for a symmetrical rotation center is $n_r \times \pi/2$, where n_r is the number of pixels along the maximal diameter of the specimen. The data at the edge of the specimen are furthest from the rotation center, and thus they have the greatest displacement. To ensure maximal spatial resolution, the distance between points in consecutive radiographs must be smaller than the effective pixel size of the detector, but it should be large enough to minimize the scan time. The spatial resolution within the radiographs is often a factor of 1.5–2.0 poorer than the limit given by the pixel size. Thus, one records fewer radiographs without compromising the image quality in the tomograms. An optimized angular increment between individual radiographs, i.e., a reasonable compromise between spatial resolution and scan time, should be determined before the measurement starts. During data acquisition, in addition to the projection radiographs of the specimen, images need to be taken with the sample removed from the beam, termed flat-field images, against which the radiographs are normalized to correct for the inhomogeneity in the beam profile. The procedure is usually automated. For long scan times as in this protocol, flat-field images are required at periodic intervals throughout the measurement to correct for time-dependent fluctuations in the beam profile.

Adapting the protocol to other specimen types. The protocol can be adapted to measure any explanted human or animal specimen containing both soft and hard tissues, including specimens from the diseased heart, vascular system, amyloid plaque–containing brain or articulations (see, for example, ref. 28). X-ray energy should be carefully chosen for the tissue type. In biological specimens with a diameter of ~1 cm, soft tissues are typically resolved with a photon energy of 10–20 keV and calcified tissues are resolved with a photon energy of 25–50 keV. Selecting too low an energy leads to insufficient photon statistics caused by highly X-ray-absorbing species, whereas too high an energy leads to loss in sensitivity for differentiation within the soft tissues. In addition, the photon energy for XGI phase SRμCT must match the design energy of the available grating setups. The main limiting factor in the measurements is often the specimen size. Stitching techniques (e.g., asymmetric rotation axis with respect to the incoming beam[34]) can increase the horizontal field of view. Stitching multiple height steps together can increase the vertical field of view[50]. The time to scan each height step is in the region of 2–6 h for optimally high-density-resolution SRμCT measurements, depending on the protocol, so the amount of beamtime available limits the number and size of specimens that can be measured. We recommend that the technique be used only for measuring specimens up to a diameter of slightly less than twice the available maximum width of the radiographs. For the beamline ID19 at the European Synchrotron Radiation Facility (ESRF), this means a maximum sample diameter of ~9 cm. The height of the investigated sample region, insofar as it exceeds the height of the field of view, will depend on the amount of beamtime available.

MATERIALS
REAGENTS
▲ **CRITICAL** In our work, all solvents were purchased from Merck, Ultraclear or JTBaker, and they were used as supplied.
Tissue samples
• The starting material for this procedure is human coronary arteries. In our published work[7], 2.5-cm-long arteries were selected for analysis from the Institute of Forensic Medicine, University Medical Center, Hamburg-Eppendorf, Germany, in consultation with medical doctors (specialists in pathology, internal medicine and critical care). The selection criteria were as follows: visual evidence of atherosclerosis; palpating of substantial amounts of hard tissue in the artery; and evidence of infarction zone on the myocardium ❗ **CAUTION** Samples should be removed in accordance with the ethical regulations and guidelines of the investigator's institution and, if applicable, with the consent of the patient and the patient's family. In this case, specimens were collected postmortem from individuals who donated their bodies for teaching and research purposes to the Institute of Anatomy, University of Basel, Switzerland. ▲ **CRITICAL** Careful selection of the artery is paramount for generic results. Medical records were unavailable here, but they would be another useful tool for selecting typical stenosed arteries.
Tissue preparation
• Fixation material: buffered formaldehyde, 4% (vol/vol) in water
• Decalcification materials: formic acid, formaldehyde, ammonium oxalate, ammonia solution, distilled water
• Dehydration materials: xylene, alcohol, paraffin
• Histological stains: hematoxylin and eosin (H&E), Masson's Trichrome, Miller
EQUIPMENT
For artery preparation
• A scalpel is required for removing the surrounding tissue, and paraffin (after the embedding process)

• Dehydration: Tissue-Tek VIP E300 Histokinette automated dehydrator (Sakura)
• Histological slices: Microm Cool-cut HYRAX M 40 (Carl Zeiss)
For data collection
• XGI phase SRμCT setup, beamline ID19, ESRF[28,51]
• Absorption SRμCT setup, beamline BW2, Helmholtz-Zentrum Geesthacht (HZG) Research Centre, HASYLAB, Deutsches Elektronen-Synchrotron (DESY)[52]. The software IDL 8.1 (Exelis Visual Information Solutions) was used for data collection and preprocessing
• Benchtop μCT setup (SkyScan 1174 compact micro-CT, Bruker microCT)
• Nikon Eclipse 80i microscope (Nikon) for photography of histology slides
Software for data reconstruction
• Benchtop μCT, NRecon (Bruker microCT)
• Absorption SRμCT, standard filtered back-projection algorithm at the beamline[52], by using an implementation of the RECLBL Library[53]
• XGI phase SRμCT, code written in-house using MATLAB R2010b (MathWorks)[54]. Note that more powerful resources are available at the synchrotron beamline. These could also have been used for data reconstruction
### Programs for data visualization and analysis
• Absorption SRμCT and XGI phase SRμCT: VGStudio Max 2.1 (Volume Graphics) and MATLAB R2010b
• H&E-stained histology slides: Fiji, ImageJ, version 1.45k (EMBL) and Adobe Photoshop CS3 (Adobe)
• Benchtop μCT: VGStudio Max 2.1
• Preprocessing for flow simulations: Geomagic Studio 12 (Geomagic) and ANSYS ICEM CFD (ANSYS)
• Flow simulations: ANSYS CFX (ANSYS)
EQUIPMENT SETUP
Benchtop μCT For preliminary benchtop μCT scans, use a SkyScan 1174 or a similar model. Note that this μCT system is among the most basic of its

2.1 A systematic protocol using multi-model micro-computed tomography for uncovering the morphology and tissue composition of critically constricted human coronary arteries

19

PROTOCOL

Figure 3 | 3D representations of four characteristic plaque morphologies with different degrees of stenosis obtained from SkyScan 1174 compact micro-CT. (**a–d**) Shown are: concave plaque (**a,b**), circumferential plaque (bottom of **c,d**). The length of each artery specimen is ~2.5 cm.
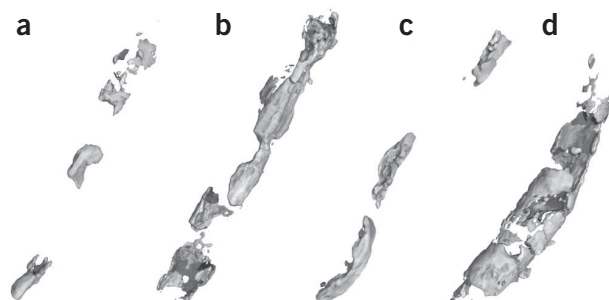
kind, allowing for very simple operation with minimal user training. Select an appropriate acceleration voltage and beam current for each specimen. Initial values should be chosen by reference to the literature and/or on the basis of previous experience. The Experimental design section 'Adapting the protocol to other specimen types' contains guidelines for the selection of the specific values. These initial values can be fine-tuned after performing preliminary scans. In our case, we used an acceleration voltage of 35 kVp and an 800-μA beam current. **Figure 3** shows characteristic examples of plaque present in human coronary arteries, which are measured using these parameters. See **Table 1** for details of experimental parameters for this and subsequent μCT steps. Comparisons of the μCT equipment and methods can be found in **Table 2** and **Box 2**.

Absorption SRμCT for nondecalcified artery Monochromatize the X-ray beam, select an appropriate photon energy, and insert and center the sample on the sample manipulator. The rotation axis of the specimen should be aligned to the pixel rows of the detector to allow the parallel reconstruction of tomography slices. The manipulator not only allows for precise sample rotation but also for sample translation to record the intensity distribution within the X-ray beam without specimen for normalization. To improve photon statistics, and thus density resolution, combine pixels in the projection radiographs by, for example, a binning factor of two in each dimension[49].

In our case, the highly intense, collimated X-ray beam at the beamline BW2 (HASYLAB, DESY) is monochromatized by means of a fixed-exit double-crystal monochromator (Si(111)-crystals) to the photon energy of 23 keV with a relative bandwidth of 10^{-4}. The tomography setup, installed 40 m from the radiation source, consists of the sample manipulator and the charge-coupled device (CCD)-based area detector. The X-ray image detector consists of a luminescent screen (270-μm-thick CdWO$_4$ single crystal), an optical lens (Nikkor 35 mm focal length, Nikon) and the CCD camera (KX2, Apogee Instruments, 14-bit digitization at 1.25 MHz, 1,536 × 1,024 pixels,

each 9 μm × 9 μm). The luminescent screen converts the incident X-rays into visible light, projected with the magnification of 3.05 onto a CCD chip, resulting in an effective pixel size of 2.95 μm. See **Figure 4** for characteristic examples of calcified human coronary arteries measured by using this setup.

Absorption SRμCT for decalcified artery Follow the procedure described above, with lower photon energy (in our case, 14 keV).

XGI phase SRμCT for decalcified artery Monochromatize the beam, select an appropriate photon energy, and insert and center the sample in the water tank (**Fig. 2**). During phase-contrast measurements, immerse the specimen in a water tank with parallel walls (we use Kapton plates). This arrangement minimizes artifacts due to strong phase shift at the interface between air and the paraffin-embedding material. In our setup, the specimen and tank are located ~10 cm upstream of the beam-splitter grating, which has a periodicity of p_1 = 4.785 μm and a Si structure height of 29 μm. The photon energy of 23 keV was selected using a double-crystal Si(111) monochromator. With a distance between source and interferometer of 150 m and a distance between the gratings of d = 481 mm (9th Talbot order), the ratio of the grating periods, p_2/p_1, is matched to the beam divergence[55]. The detector, placed ~3 cm downstream of the analyzer grating with gold lines of a periodicity of p_2 = 2.400 μm and a structure height of 50 μm, is a lens-coupled scintillator and CCD system that uses a FReLoN (Fast-Readout, Low-Noise, ESRF, Grenoble, France) CCD with 2,048 × 2,048 pixels. The effective pixel size corresponds to 5.4 μm.

TABLE 1 | Parameters for image acquisition in PROCEDURE Steps 2, 3, 5 and 6.

	Non-decalcified artery		Decalcified artery	
	Benchtop μCT	**Absorption SRμCT**	**Absorption SRμCT**	**XGI phase SRμCT**
Protocol step number	2	3	5	6
Photon energy	≤35 keV (800 μA beam current)	24 keV	14 keV	23 keV
Number of radiographs	1,200	1,440	1,440	999
Rotation angle increment	360°/1,200	360°/1,440	360°/1,440	360°/999
Rotation axis position	Centered	Asymmetric	Asymmetric	Centered
Projection size (pixels)	1,024 × 1,024	1,536 × 751	1,536 × 1,023	2,048 × 2,048
Pixel length (μm)	14.4	7.2 or 7.9	5.3	5.4
Scan time per height step	60 min	220 min	220 min	390 min
Number of height steps	2	4 or 2	2	2
Total size of raw data	5 GB (16 bit)	15 GB for 4 height steps (16 bit)	10 GB (16 bit)	67 GB (16 bit)
Size of reconstructed data	0.2 × 10^{10} voxels (2 GB, 8 bit)	5.4 × 10^{10} for 4 height steps (50 GB, 8 bit)	1.8 × 10^{10} (17 GB, 8 bit)	1.7 × 10^{10} (32 GB, 16 bit)

Figure 4 | Absorption SRμCT visualization of plaque and cardiac muscle. Top, 3D visualization of plaques of three nondecalcified human coronary arteries, corresponding to **Figure 3a–c**, extracted by using intensity-based thresholding[45]. White arrows denote the location of slice (below) within the plaque. Bottom, 2D slices showing plaque (white) and muscle (dark gray).
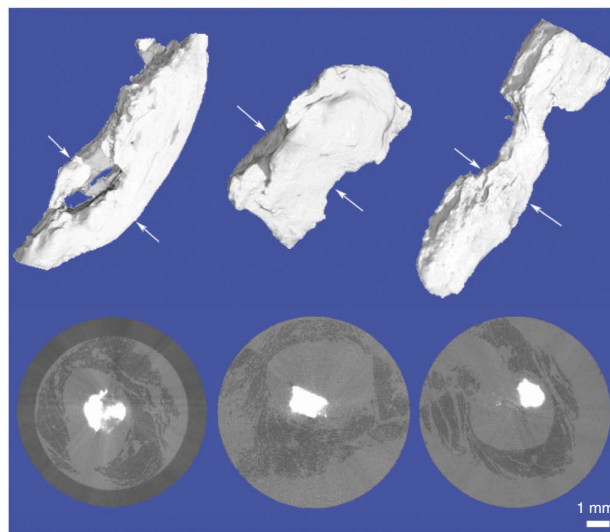
Computing equipment for benchtop μCT Data acquisition: Dell Precision 490 workstation with a four-core 2.66-GHz Intel Xeon processor, 4 GB of RAM, a 256-MB ATI FIRE GL V7200 (MRGA13B) graphics card and Windows XP Professional. Data reconstruction: Dell Precision 490 workstation with a four-core 2.66-GHz Intel Xeon processor and 8 GB of RAM with 64-bit Windows 7 Enterprise.
Computing equipment for absorption SRμCT Data acquisition: Pentium DualCore CPU 3.4 GHz, 4 GB RAM running Windows XP Professional. Data reconstruction: several workstations running Scientific Linux, with a total of 128 GB of RAM and 48 cores.
Computing equipment for XGI phase SRμCT Data acquisition: PC cluster available at the beamline. Data reconstruction: Dell Precision T5500 workstation with a 64-bit Linux openSUSE 11.3 operating system with a total 24 GB of RAM and four cores. This setup was also used for registering the absorption and XGI phase SRμCT data sets. This was the computing equipment at the university laboratory; it should be noted that more powerful resources are available at the synchrotron beamline, and they could have been used for reconstruction of the data.
Computing equipment for flow simulations Image data preprocessing, steady-flow calculations and postprocessing of results; Fujitsu Celsius R670-2

workstation with a six-core 2.53-GHz Intel Xeon processor E5649 and 48 GB of RAM with 64-bit Windows 7 Professional. Transient flow simulation is conducted using 16 parallel nodes of Brutus, the central high-performance cluster of ETH Zurich, Switzerland.

PROCEDURE
▲ **CRITICAL** The experiment can be paused after any step, for example, while waiting for an available beamtime, provided that the artery is stored appropriately (i.e., fixed in formaldehyde and embedded in paraffin). The chronology is presented below. The order of the absorption and XGI phase SRμCT steps can be swapped. Details of the parameters used in the image measurements are given in **Table 1**. **Table 2** highlights the differences in tissue visualization, experimental time and cost (**Box 2**) and complexity of each μCT method.

Artery extraction, fixation and embedding ● **TIMING** 48 h per artery
1| Extract the artery as soon as possible after death and select an appropriate specimen (see 'Tissue samples' in Reagents). For vessel specimens 2–3 cm long, fix them in at least 20 times the sample volume of 4% (vol/vol) formaldehyde for at least 10 h, to ensure that fixation is complete. This step may take up to 2 d for large specimens with plenty of plaque. Marking the orientation of the specimen will help with data registration.

2| Dehydrate the artery by soaking it under reduced pressure overnight in alcohol, followed by xylene, and then immerse it in molten paraffin at a temperature of 60 °C.

3| Embed the artery in a paraffin block. Once it is cooled, minimize the specimen diameter by, e.g., trimming it with a scalpel, to be able to use pixel sizes as small as possible while imaging the whole object.
▲ **CRITICAL STEP** Embedding in paraffin after fixation in formaldehyde is advisable for measurements, as it prevents movement of the sample during the experiment and allows the same region to be easily identified for imaging and analysis. Take care to ensure that there are no trapped air bubbles in the paraffin, particularly inside the vessel. Such air bubbles, even microscopic ones, lead to strong artifacts in the XGI phase SRμCT images.

Measurement
4| The nondecalcified sample can now be analyzed by benchtop μCT (option A, SkyScan 1174 benchtop micro-CT) and/or by SRμCT (option B).
(A) Benchtop μCT ● **TIMING** 75 min per height step plus data reconstruction time
   (i) To minimize the pixel size, set the geometric magnification to a value that allows the entire specimen to just fit into the field of view for all radiographs. In our case, this resulted in a pixel size of 14.4 μm² (**Table 1**).

| PROTOCOL

TABLE 2 | Comparison of µCT methods

Specimen	Plaque-containing artery		Artery with plaque removed	
Measurement type	**Benchtop µCT**	**Absorption SRµCT**	**Absorption SRµCT**	**XGI phase SRµCT**
Visualization				
Hard tissues (calcified plaque)	Local intensity–based segmentation	Local intensity–based segmentation, streak artifacts	Traces of plaque observable, plaque-related artifacts	Traces of plaque observable, no plaque-related artifacts
Lumen segmentation	Invisible	Invisible	Segmented using region-growing tools	Partially segmentable, artifacts from embedded air bubbles
Identifiable soft tissues (correspondence to histology)	None	Surrounding heart muscle	Muscle, fibrous cap, cholesterol, adventitia and foamy cells (no distinction); residual plaque	Foamy cells, cholesterol, epithelium and adventitia (no distinction); muscle and fibrose cap (no distinction); residual plaque
Experiment time for one height step				
Experiment setup	0.25 h, center sample, select experimental parameters	5 h, beamline setup; 0.5 h, select parameter settings	5 h, beamline setup; 0.5 h, select parameter settings	5 h, beamline setup; plus extra 5 h, grating setup; 0.5 h, select parameter settings
Measurement	1.2 h	3.7 h	3.7 h	6.5 h
Preparative work for reconstruction	None	1.5 h	1.5 h	3 h (image processing)
Reconstruction using the described computing equipment (see 'Computing Equipment')	1 h	0.5 h	0.5 h	4.5 h
Cost and complexity				
Cost of equipment	$100,000 to purchase plus $5,000 running costs per year	Beamtime free of charge if beamtime granted through peer-review process (**Box 2**)	Beamtime free of charge if beamtime granted through peer-review process (**Box 2**)	Beamtime free of charge if beamtime granted through peer-review process (**Box 2**), including XGI phase SRµCT setup (**Figure 2**)
Complexity of equipment setup	Introduction required, can be done by undergraduates	Can be operated by non-expert scientist or graduate student after basic training	Can be operated by non-expert scientist or graduate student after basic training	Requires assistance from experts

(ii) Reconstruct the data by using the manufacturer's NRecon software (based on a modified Feldkamp algorithm) with a correction to reduce ring and beam-hardening artifacts within the tomography data set. Suitable parameters for beam-hardening compensation should be defined in an iterative process. The number of iterations required to reach optimum parameters can be greatly reduced by consulting suppliers and experts in the field.
    ? TROUBLESHOOTING

(B) SRµCT for nondecalcified artery ● TIMING 3 h 40 min per height step plus data reconstruction time

(i) At a beamline with SRµCT setup optimized for absorption contrast mode, acquire ~1,000 radiographs at equiangular steps along 180°. If necessary, use an asymmetric rotation axis with respect to the detector center, record radiographs at equiangular steps along 360° and combine the opposite radiographs to create radiographs with up to two times more pixels for the spatial resolution increase (**Table 1**)[50].

Box 2 | Charges for acquiring tomograms at synchrotron radiation sources

The cost of synchrotron radiation-based tomography varies depending on the synchrotron and funding options available. Beamtime can be applied for by submitting a proposal for peer review, or it can be paid for to guarantee rapid access. Applicants whose beamtime proposals are accepted use the facilities free of charge and conduct the measurements on their own once they have received a short training by the beamline staff (typically half a day). Paid access has a shorter waiting time, and data can be acquired and processed by the beamline staff for an extra cost. Unlike in proposal-based beamtime, there is no obligation to publish the results. The cost for paid access varies slightly, but it is usually charged in shifts of a fixed time, e.g., 8 h costing USD $5,500, depending on whether the users operate the experiment themselves or require the beamline staff to acquire and process the data. Note that, contrary to absorption tomography, phase tomography currently still requires assistance from experts in the method in planning, setting up and executing such measurements.

(ii) Experimentally characterize the spatial resolution of the setup by using the 10% value of the modulation transfer function from a highly X-ray–absorbing edge[31]. In our case, the derived values corresponded to 7.24 and 7.88 μm, respectively. Although the X-rays from synchrotron radiation sources are not completely parallel, they are sufficiently parallel that the tomograms can be reconstructed slice-wise by using a standard filtered back-projection algorithm for a parallel beam.
? TROUBLESHOOTING

Artery decalcification and re-embedding in paraffin ● TIMING 3 d in total
5| *Preparation of the decalcifier.* This is a solution of distilled water:formic acid:formaldehyde (87:8:5 (vol/vol)).
! CAUTION Decalcification solvents are corrosive and carcinogenic. Handle them in a fume hood with gloves.

6| Remove paraffin from the artery by heating it to 60 °C, and then wash the artery in a Histokinette (Tissue-TEK VIP E3000) over a 12-h period in xylene; then wash it with alcohol and finally with water under reduced pressure.

7| Immerse the artery in decalcifier at 37 °C and test for complete decalcification periodically by extracting a 2-ml sample of decalcifier surrounding the artery and mixing with 1 ml of ammonium oxalate (5%, vol/vol) and 1 ml of ammonia (5%, vol/vol). If the solution becomes milky, decalcification is incomplete and the sample should be immersed in a new solution of decalcifier. Test for complete decalcification twice a day until it yields a clear, colorless solution.

8| Dehydrate and embed the artery in paraffin, as described in Steps 2 and 3.
? TROUBLESHOOTING

9| In the conventional and XGI phase SRμCT setups used, a sample diameter of <1 cm is preferred, as it facilitates the collection of high-resolution data. Minimize the sample diameter by, e.g., trimming the paraffin to roughly the diameter of the artery with a scalpel (taking care not to cut too close to the artery itself), and then rubbing the surface to smooth any uneven areas. This prevents air bubbles from forming on the paraffin surface during XGI phase SRμCT when the sample is immersed in a water tank. Any bubbles, even microscopic ones, can lead to strong artifacts in XGI phase SRμCT data. An example of an artery prepared in this manner is shown in **Figure 2**.
? TROUBLESHOOTING

Measurement: absorption SRμCT for decalcified artery ● TIMING ~4 h per height step
10| Conduct data acquisition at a beamline with SRμCT setup optimized for absorption contrast mode (as in Step 3, above, see **Table 1**). As the highly X-ray-absorbing plaque has been removed, lower energies can be used to improve the contrast between soft tissues (**Table 1**).
? TROUBLESHOOTING

Measurement: XGI phase SRμCT for decalcified artery ● TIMING ~7 h per height step
11| Conduct data acquisition at a beamline with the setup optimized for XGI phase-contrast mode. To image sections of the artery that are larger than the height of the beam (i.e., larger than the field of view), acquire multiple scans at different height positions (**Table 1**). In our case, we acquired two slightly overlapping height steps to image the whole artery. A detailed description of grating interferometry and of the phase-stepping method is given by Weitkamp *et al.*[20].
? TROUBLESHOOTING

*2.1 A systematic protocol using multi-model micro-computed tomography for
uncovering the morphology and tissue composition of critically constricted human
coronary arteries*   23

| PROTOCOL

Preparation of histology slides ● TIMING ~2 d for 30 slides

12| Slice the paraffin-embedded, decalcified artery into 2–4-μm lateral sections forming a paraffin ribbon with the arterial slices embedded therein. Maintaining the artery in the same paraffin embedding material minimizes the risk of morphological changes between μCT measurements and histological preparation. As it is far too time-consuming to prepare a slide from every slice made, mount, for example, every 20th slice from the paraffin on a glass slide. Keep the remaining slices in case further analysis or slide preparation is required.
? TROUBLESHOOTING

13| Stain the slices with H&E.
▲ **CRITICAL STEP** H&E stains the cell nuclei blue and nonspecifically stains intercellular and intracellular proteins pink. To further analyze the tissue types present, consider using other stains such as Masson's Trichrome to distinguish cells from connective tissue and Miller stain to distinguish elastic fibers and collagen.
? TROUBLESHOOTING

Measurement: 2D histology slices ● TIMING ~1 d

14| Photograph the slices mounted on glass slides by using a microscope and a camera (we used a Nikon Eclipse 80i microscope at tenfold magnification). For improved spatial resolution, we photographed each slide in an average of 20 sections and stitched the images together by using the Stitching plug-in[56] available in the Fiji software (ImageJ version 1.45k)[57]. This results in high-resolution color images of ~4,500 × 5,500 pixels, with a pixel size of 0.5 μm.

Analysis and comparison of results ● TIMING 2 weeks (working time)

15| To compare absorption and XGI phase SRμCT of decalcified arteries, a registration of the data sets using a 3D rigid algorithm[58,59] with 6 d.f.—three for translation and three for rotation—should be sufficient for a solid state. Register the data sets by using a 3D affine algorithm with another 3 d.f. (scaling factors) in order to compensate for the mismatch in individual pixel sizes at different SR facilities. Because the imaging modalities are different, preferentially perform the 3D registration by using the classical maximization of mutual information[36,37]. All registration steps can be automated; however, an appropriate starting point for the registration should be identified during a preliminary manual registration. This allows faster automated registration and avoids problems such as mirrored data sets.

16| Compare 3D SRμCT data sets with histology slices by performing a 2D-2D nonrigid registration of the individual histology slices (**Fig. 5**) with the appropriately selected slice from the 3D-registered phase-contrast SRμCT data set. For this, we used a code developed by Kroon and Slump[60] in MATLAB 2010b (multimodality nonrigid demon algorithm image registration).

Figure 5 | Histograms, cross-sectional tomograms, and histological slices show different tissue types. (**a**–**h**) Cross-sectional slices from absorption SRμCT (**c**) and XGI phase SRμCT (**d**) are comparable. However, **d** shows greater dynamic range in the soft-tissue region, with different tissue types validated by comparison with the corresponding H&E-stained histology slide (**e**). (**a**,**b**) Histograms of 3D reconstructions from absorption SRμCT (**a**) and XGI phase SRμCT (**b**) confirm that XGI phase SRμCT also provides more detailed information about the anticipated soft tissues present in the 3D data set, and that **c** and **d** are typical tomography slices. In absorption SRμCT (**a**), one can only distinguish between the paraffin (peak 1); soft tissues, including muscle, fat and fibrous cap (peak 2); and artifacts caused by residual plaque (slight hump on right hand side of peak 2). (**f**) The same slice with annotations highlights the artifact caused by an entrapped air bubble in the paraffin embedding (white circle) and the origin of the two observed streak artifacts caused by highly absorbing species, where decalcification is incomplete (black arrows). In XGI phase SRμCT (**b**), one can additionally distinguish between the soft tissues, i.e., paraffin and lumen (peak 1); foamy cells, cholesterol, epithelium (fine, well-defined outline of vessel lumen) and adventitia (peak 2); muscle and fibrous cap (peak 3); and residual plaque artifacts (peak 4). (**g**) This is illustrated in a false-color representation (see also Holme *et al.*[7]). Here, the white circle highlights an air bubble, and the white arrow points to the streak artifact that this causes in XGI phase SRμCT images; peak 1 is black, peak 2 is yellow, peak 3 is gray to white and peak 4 is red to blue. (**h**) Finally, these tissues are also identified on the H&E-stained histology slide, prepared by maximizing the contrast in each color channel, with the lumen (**h**, indicated by i), region of foamy cells and cholesterol (**h**, indicated by ii) and residual plaque with calcification (**h**, indicated by iii) outlined.
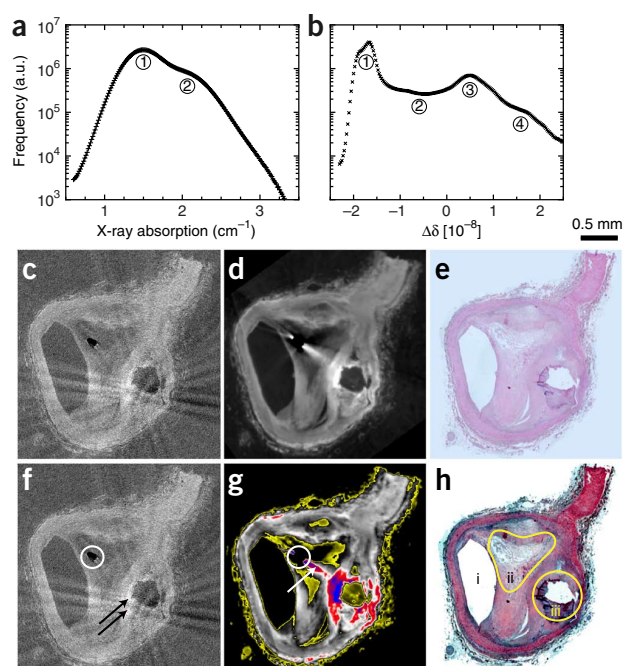
Figure 6 | The lumen mesh segmented from the absorption SRµCT data set requires further treatment before being used in flow simulations. Left, exported, triangulated surfaces of the segmented artery. Middle, surface smoothed and inlet-outlet boundary conditions defined. Right, individual artifacts removed, surface further smoothed and bifurcation boundary conditions defined. The distance between the arrowheads is 950 µm.
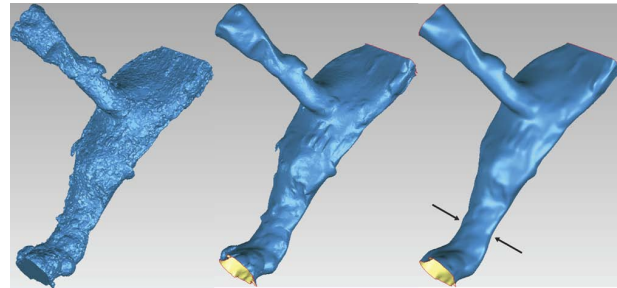
Converting voxel-based data to vector-based data

▲ **CRITICAL** The absorption SRµCT data form a solid grounding for clinically relevant flow simulations from which the endothelial shear stress distribution (time-averaged wall shear stress, AWSS) can be derived[61]. The voxel-based tomography data, however, are noisy because of the limited photon statistics[52], and they have to be converted into a vector-based format as commonly used for simulations. After the segmentation of the lumen, a mesh must be extracted.

17| Use the region-growing tool in VGStudio Max 2.1 to select a seeding point far from visible artifacts. Conduct the lumen segmentation in a step-wise manner, adapting the sensitivity by visual inspection (we used sensitivity levels varying between 20 and 30 a.u.).

18| Next, convert the extracted voxel-based data of the lumen to a triangular mesh of the lumen surface in stl format, by using the Export function in VGStudio Max 2.1 (**Fig. 6**, left). Original voxel-based data are shown in **Figure 7**.

19| Smooth the lumen surface by using the 'Polygons' → 'Relax Polygons' tool in Geomagic Studio 12 with the settings 'smoothness level' and 'strength' = medium, and 'curvature priority' = maximum. This smooths the surface by decreasing the angles between individual triangles of the mesh. Planarize inlet and outlet boundaries (**Fig. 6**, middle).

20| Use the automatic 'Polygons' → 'Mesh Doctor' tool in Geomagic Studio 12 to remove individual artifacts such as non-manifold edges, self-intersections, spikes, small holes and tunnels, as well as highly creased edges. Further smooth the surface by using the 'Polygons' → 'Relax Polygons' tool in Geomagic Studio 12 with 'smoothness level', 'strength', 'curvature' = maximum. Finally, define planarized boundary conditions for the bifurcations, if present (**Fig. 6**, right).

21| From the resulting lumen surface, generate a volumetric tetrahedral computational grid, e.g., by using an octree method in ANSYS ICEM CFD (ANSYS).

22| For accurate calculation of wall shear stress (WSS) at a minimal computational cost, refine the mesh at the vicinity of the arterial wall and gradually coarsen toward the lumen center.

23| Successively refine the computational mesh and compare the WSS obtained at each refinement step to test whether the computational results are independent of the spatial discretization. The procedure is terminated when the values between two refinements differ by <1%.

Flow simulations
24| For flow simulations, extrude the inlet and outlet surface grids along their axes to five times the boundary diameter to allow flow to develop. This is common practice for uncertain boundary conditions[62].

25| Solve the incompressible Navier-Stokes and continuity equations numerically in ANSYS CFX (ANSYS) to obtain the velocity and pressure fields within the artery. Regard blood as a Newtonian fluid with a density of 1,050 kg/m^3 and viscosity of 0.0035 Pa·s (ref. 63), and use residual reduction to 10^{-8} of the initial value as the convergence criterion.
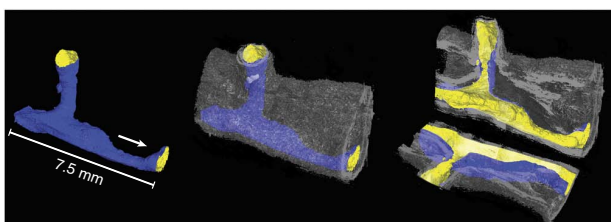
Figure 7 | Cross-sectional reconstructed image of the lumen morphology extracted from absorption SRµCT showing the effective vessel lumen along a 7.5-mm-long section of a diseased human coronary artery at the bifurcation between the circumflex and the LAD artery (surface blue, inside yellow), soft tissues (semitransparent gray) and direction of blood flow (white arrow).

| PROTOCOL

Figure 8 | AWSS derived from the transient flow simulations by using the absorption SRµCT data, as prepared for **Figure 7**. Blue-colored regions show similar AWSS as healthy arteries (<5 Pa). Green-colored regions are larger than those observed in the healthy body (7–12 Pa). Yellow- and red-colored regions indicate markedly stenosed areas (>13 Pa), with AWSS values being one order of magnitude higher than those typically observed in the healthy vascular system. Length along the vessel section is 7.5 mm.
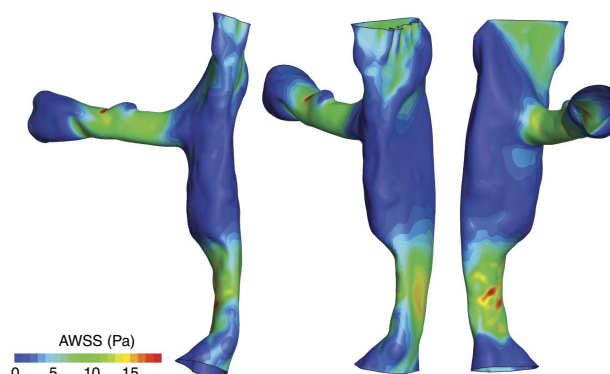
26| Begin with steady-state simulations to obtain a first approximation of hemodynamics, and then perform transient calculations to analyze time-dependent flow and shear stress patterns.

27| For transient simulation (**Fig. 8**), select a suitable flat velocity profile with temporal waveform. Impose a zero-pressure boundary condition at the extended outlets of the computational model arteries. For less severely stenosed and larger artery segments than treated here, boundary conditions based on Murray's Law or variations thereof should be applied to the outlets instead of zero pressure[64]. The artery studied in this protocol is the bifurcation between the circumflex and left anterior descending (LAD) coronary artery. Temporal waveforms from such diseased human LADs are unavailable in the literature, and thus we used data from a canine LAD coronary artery at rest, as used by La Disa *et al.*[65] to model the effect of alterations in WSS distribution.

? TROUBLESHOOTING
Troubleshooting advice can be found in **Table 3**.

TABLE 3 | Troubleshooting table.

Step	Problem	Solution
4A(ii)	Beam-hardening artifacts as seen by cupping (i.e., apparently higher absorption at the specimen's periphery)	Use a metal filter such as aluminum or copper to narrow the spectrum by increasing the mean X-ray energy at constant maximal X-ray energy
4B(ii), 10, 11	Streak artifacts from highly X-ray–absorbing species (even after decalcification)	Increase the energy of the incident X-ray beam
4, 10, 11	Undesired specimen movement (relative or rotational/translational)	Stop measurement, improve the fixation and restart the measurement. Consider the inertia of the specimen within the liquid environment
8, 9	Air bubbles embedded in the paraffin	Re-embed with slower cooling or reduced pressure. If possible, check for the presence of air bubbles using a benchtop µCT setup (e.g., SkyScan 1174) before making time-consuming measurements at synchrotron facilities
11	Bubbles formed between paraffin block and water bath	Rub the paraffin to smooth the surface
12, 13	Pleats or folds in the histology slices	Use a neighboring slice from the stored histology ribbon

● **TIMING**
In terms of time, there are two main crucial factors. First, beamtime at the desired synchrotron radiation facility must be planned well in advance for both absorption and phase tomography. Second, tissue preparation is time-consuming because it includes diffusion-limited processes for fixation and staining. The time for histology, which includes cutting and staining, depends on the number of histological slides to be prepared. Below are the timings that we typically use in our measurements.
Steps 1–3, artery extraction, fixation and embedding: 48 h per artery. Several arteries can be collected in one session
Step 4A, benchtop µCT of nondecalcified artery: 75 min per height step (data reconstruction: 1 h per artery)
Step 4B, absorption SRµCT of nondecalcified artery: 3 h 40 min per height step for data collection (several height steps are needed). Data reconstruction takes 2 h per height step. The total number of height steps depends on artery length and X-ray beam height

Steps 5–7, artery decalcification: 12 h to several days per artery (depends on the initial degree of calcification)

Steps 8 and 9, re-embedding in paraffin: 6 h per artery (several arteries can be prepared simultaneously)

Step 10, absorption SRμCT of decalcified artery: as in Step 4B

Step 11, XGI phase SRμCT of decalcified artery: 6 h per height step for tomography (several height steps are needed). Data processing for phase-projection images takes 3 h, and data reconstruction takes 4 h 30 min per height step. Note that we used our in-house reconstruction tool and computer for the XGI phase SRμCT reconstruction (see Equipment). Provided the same reconstruction tool and computer are used, the time taken to reconstruct similarly sized absorption and phase SRμCT data sets is comparable. The total number of height steps depends on artery length and X-ray beam field of view

Steps 12 and 13, preparation of histology slices: 2 d for cutting and staining (for 30 histological slices mounted on suitable glass substrates)

Step 14, 2D histology slides: 1 d for microscopy and postprocessing (stitching) of digital slices

Steps 15–27, analysis of results and flow simulations: 2 working weeks, including automatic 3D data registration

ANTICIPATED RESULTS

This protocol allows human or animal organs to be measured with micrometer precision. Without the deformation risk during histological slide preparation, very reliable information is given about morphology and plaque presence. Specifically, the nondestructive μCT techniques applied here can, in combination, give an indication of the location of plaques in soft tissues in 3D and enable us to identify and characterize soft-tissue components by their refractive indices. In the case of blood vessels, they can also give quantitative information about the percentage cross-section of the lumen over the whole measured area. Such results can therefore be used to characterize atherosclerosis severity in postmortem arteries in terms of percentage occlusion of arterial cross-sectional area and plaque vulnerability. Meshes extracted from imaging data of the vascular system (here, human coronary arteries) can directly be used for flow simulations or other simulation models.

We find that the SkyScan 1174 benchtop μCT allows plaque segmentation but does not give meaningful information about the soft tissues. The μCT data are therefore a useful preliminary screening tool to identify the 3D structure of the plaque and aid selection of diseased arteries. We find that the resolution of the lumen morphology is of highest quality in absorption SRμCT of decalcified arteries. In addition to having a smaller pixel size in comparison with the other methods, it presents artifacts that are due to the highly X-ray-absorbing plaque, whereas the XGI phase SRμCT artifacts originate from air bubbles formed during paraffin embedding (see example in **Fig. 5**). These air bubbles often occur at or near the lumen, and therefore they make simple extraction tools such as local intensity–based segmentation unfeasible.

In this protocol, the lumen morphology is extracted from the absorption SRμCT data set and used to quantify the extent of stenosis (**Figs. 6** and **7**). By using this approach for the specimens studied in our published work[7], the maximum occlusion was found to have a surface area of 0.83 mm^2, corresponding to an 85% stenosis by lumen cross-sectional area.

XGI phase SRμCT affords distinction between different tissue types. We are able to assign $\Delta\delta$ values to the plaque artifacts (1×10^{-8} to 2×10^{-8}), muscle and fibrous cap (0.25×10^{-8} to 0.75×10^{-8}), and foamy cells, cholesterol, epithelium and adventitia (-1×10^{-8} to 0). Note that this is usually impossible in absorption contrast owing to the overlapping attenuation values and the presence of artifacts caused by the plaque. Note that the $\Delta\delta$ values are specific to the experimental parameters. Donath *et al.*[66] proposed converting these values to phase-contrast Hounsfield units (HU-phase) given by $\frac{\Delta\delta}{\delta_{water}} \cdot 1{,}000$. This allows a standardized, quantitative comparison of phase shifts that are measured in a variety of specimens by using different experimental parameters, and it has been used by, for example, Hetterich *et al.*[67] investigating tissue types found in human coronary arteries. HU-phase values calculated from the $\Delta\delta$ values reported above are 23–46 HU-phase (plaque artifacts), 5–17 HU-phase (muscle and fibrous cap) and −23–0 HU-phase (foamy cells, cholesterol, epithelium and adventitia). These are slightly lower than the values found by Hetterich *et al.*[67], which is probably due to the methods used for segmenting the tissues, specimen preparation and variations in artery structure between patients.

Histology provides a gold standard for confirming the tissues; see, for example, 2D images (**Fig. 5**). However, constructing a 3D image stack of the histology images is not trivial. Because of the pleats and different orientations of the individual slices in the histology slides, it is impossible to stack them automatically to create a 3D image by using software such as VGStudio or Fiji. Therefore, we overlaid the images manually in Adobe Photoshop C5, taking the artery lumen as the reference point, and then stacked them to give a 3D representation with VGStudio Max 2.1. We find that the quality of the 3D morphological data is substantially compromised by the unavoidable pleats in individual slices produced during the cutting process. In addition, histology provides a poor axial resolution (here, the distance between each prepared H&E-stained histology slide is 400–800 μm) and error in the manual image overlay when stacking. However, the individual slices are indispensable for validation of tissue characterization with XGI phase SRμCT data. In combination, XGI phase SRμCT and histology can be used to build up a 3D picture of the size and location of tissue types present, and the plaque stability can be qualified.

2.1 A systematic protocol using multi-model micro-computed tomography for uncovering the morphology and tissue composition of critically constricted human coronary arteries

27

| PROTOCOL

An example of spatial distribution of AWSS after three cardiac cycles (see PROCEDURE Steps 24–27) is shown in **Figure 8**. In this experiment, an increase of AWSS is observed from less than 3 Pa in the least-constricted to 18 Pa in the most-stenosed areas. This example illustrates that the imaging data are sufficiently detailed to perform meaningful flow simulations after further data processing.

AUTHOR CONTRIBUTIONS M.N.H. and B.M. wrote the manuscript with sections provided by T.W. and V.K. G.S., I.Z., M.N.H. and T.W. set up and performed the phase-contrast SRμCT measurements. F.B., G.S., H.D. and M.N.H. set up and performed the absorption-contrast SRμCT measurements. G.S., H.D. and M.N.H. performed the benchtop μCT measurements. F.B., M.N.H., G.S. and H.D. performed data processing, reconstruction and analysis, excluding the flow simulations (Steps 21–27), which were performed by F.R. and V.K. Histology slides were prepared by J.A.L. T.S. and J.A.L. provided a clinical perspective for data analysis. T.W., J.A.L., V.K. and I.Z. provided technical and conceptual advice. B.M. and T.S. designed the study. All authors contributed to editing the manuscript, including tables and figures.

COMPETING FINANCIAL INTERESTS The authors declare no competing financial interests.

Reprints and permissions information is available online at http://www.nature.com/reprints/index.html.

1. Lloyd-Jones, D. *et al.* Heart disease and stroke statistics—2009 update: a report from the American Heart Association Statistics Committee and Stroke Statistics Subcommittee. *Circulation* **119**, e21–e181 (2009).
2. Knight, J. *et al.* Choosing the optimal wall shear parameter for the prediction of plaque location, a patient-specific computational study in human right coronary arteries. *Atherosclerosis* **211**, 445–450 (2010).
3. Cheng, C. *et al.* Large variations in absolute wall shear stress levels within one species and between species. *Atherosclerosis* **195**, 225–235 (2007).
4. Holme, M.N. *et al.* Shear-stress sensitive lenticular vesicles for targeted drug delivery. *Nat. Nanotechnol.* **7**, 536–543 (2012).
5. Korin, N. *et al.* Shear-activated nanotherapeutics for drug targeting to obstructed blood vessels. *Science* **337**, 738–742 (2012).
6. Goderie, T.P.M. *et al.* Combined optical coherence tomography and intravascular ultrasound radio frequency data analysis for plaque characterization. Classification accuracy of human coronary plaques *in vitro*. *Int. J. Cardiovasc. Imaging* **26**, 843–850 (2010).
7. Holme, M.N. *et al.* Morphology of atherosclerotic coronary arteries. *Proc. SPIE* **8506**, 850609 (2012).
8. Coombs, B.D., Rapp, J.H., Ursell, P.C., Reilly, L.M. & Saloner, D. Structure of plaque at carotid bifurcation high-resolution MRI with histological correlation. *Stroke* **32**, 2516–2521 (2001).
9. Stock, S.R. *Microcomputed Tomography: Methodology and Applications* (CRC Press, 2008).
10. Drews, S. *et al.* Comparative micro computed tomography study of a vertebral body. *Proc. SPIE* **7078**, 70780C (2008).
11. Germann, M. *et al.* Strain fields in histological slices of brain tissue determined by synchrotron radiation-based micro computed tomography. *J. Neurosci. Meth.* **170**, 149–155 (2008).
12. Fitzgerald, R. Phase-sensitive X-ray imaging. *Phys. Today* **53**, 23–26 (2000).
13. Momose, A. Recent advances in X-ray phase imaging. *Jpn. J. Appl. Phys.* **44**, 6355–6367 (2005).
14. Momose, A., Takeda, T., Itai, Y. & Hirano, K. Phase-contrast X-ray computed tomography for observing biological soft tissues. *Nat. Med.* **2**, 473–475 (1996).
15. Beckmann, F., Bonse, U., Busch, F. & Günnewig, O. X-ray microtomography (μCT) using phase contrast for the investigation of organic matter. *J. Comput. Assist. Tomo.* **21**, 539–553 (1997).
16. Förster, E., Goetz, K. & Zaumseil, P. Double-crystal diffractometry for the characterization of targets for laser fusion experiments. *Krist. Tech.* **15**, 937–945 (1980).
17. Davis, T., Gao, D., Gureyev, T., Stevenson, A. & Wilkins, S. Phase-contrast imaging of weakly absorbing materials using hard X-rays. *Nature* **373**, 595–598 (1995).
18. Koch, A., Raven, C., Spanne, P. & Snigirev, A. X-ray imaging with submicrometer resolution employing transparent luminescent screens. *J. Opt. Soc. Am. A* **15**, 1940–1951 (1998).
19. Cloetens, P. *et al.* Holotomography: quantitative phase tomography with micrometer resolution using hard synchrotron radiation X-rays. *Appl. Phys. Lett.* **75**, 2912–2914 (1999).
20. Weitkamp, T. *et al.* X-ray phase imaging with a grating interferometer. *Optics Exp.* **13**, 6296–6304 (2005).
21. Koyama, I., Momose, A., Wu, J., Lwin, T.T. & Takeda, T. Biological imaging by X-ray phase tomography using diffraction-enhanced imaging. *Jpn. J. Appl. Phys. 1* **44**, 8219–8221 (2005).
22. Schulz, G. *et al.* High-resolution tomographic imaging of a human cerebellum: comparison of absorption and grating-based phase contrast. *J. R. Soc. Interface* **7**, 1665–1676 (2010).
23. Pfeiffer, F. *et al.* High-sensitivity phase-contrast tomography of rat brain in phosphate-buffered saline. *J. Phys. Conf. Ser.* **186**, 012046 (2009).
24. Pfeiffer, F. *et al.* High-resolution brain tumor visualization using three-dimensional X-ray phase-contrast tomography. *Phys. Med. Biol.* **52**, 6923–6930 (2007).
25. Rikhtegar, F. *et al.* Compound *ex vivo* and *in silico* method for hemodynamic analysis of stented arteries. *PLoS ONE* **8**, e58147 (2013).
26. Galonska, M. *et al.* Characterization of atherosclerotic plaques in human coronary arteries with 16-slice multidetector-row computed tomography by analysis of attenuation profiles. *Acad. Radiol.* **15**, 222–230 (2008).
27. Zachrisson, H. *et al.* Soft tissue discrimination *ex vivo* by dual energy computed tomography. *Eur. J. Radiol.* **75**, e124–e128 (2010).
28. Müller, B. *et al.* Grating-based tomography of human tissues. *AIP Conf. Proc.* **1466**, 107–112 (2012).
29. Pfeiffer, F., Weitkamp, T., Bunk, O. & David, C. Phase retrieval and differential phase-contrast imaging with low-brilliance X-ray sources. *Nat. Phys.* **2**, 258–261 (2006).
30. Tapfer, A. *et al.* Experimental results from a preclinical X-ray phase-contrast CT scanner. *Proc. Natl. Acad. Sci. USA* **109**, 15691–15696 (2012).
31. Müller, B. *et al.* Three-dimensional evaluation of biocompatible materials by microtomography using synchrotron radiation. *Proc. SPIE* **4503**, 178–188 (2002).
32. Schulz, G. *et al.* Evaluating the microstructure of human brain tissues using synchrotron radiation–based micro-computed tomography. *Proc. SPIE* **7804**, 78040F (2010).

33. Schulz, G. *et al*. Multimodal imaging of human cerebellum—merging X-ray phase microtomography, magnetic resonance microscopy and histology. *Sci. Rep.* **2**, 826 (2012).

34. Schulz, G. *et al*. Asymmetric rotational axis reconstruction of grating-based X-ray phase-contrast tomography of the human cerebellum. *Proc. SPIE* **8506**, 850604 (2012).

35. Herzen, J. *et al*. X-ray grating interferometer for imaging at a second-generation synchrotron radiation source. *Proc. SPIE* **7804**, 780407 (2010).

36. Maes, F., Collignon, A., Vandermeulen, D., Marchal, G. & Suetens, P. Multi-modality image registration maximization of mutual information. *IEEE* **16**, 187–198 (1997).

37. Viola, P. & Wells, W.M. III Alignment by maximization of mutual information. *Int. J. Computer Vision* **24**, 137–154 (1997).

38. Schulz, G. *et al*. Three-dimensional strain fields in human brain resulting from formalin fixation. *J. Neurosci. Meth.* **202**, 17–27 (2011).

39. Stalder, A. *et al*. Combining micro computed tomography and histology to assess the efficacy of bone augmentation materials. *Int. J. Mater. Res.* doi:10.3139/146.111050 (2014).

40. Grabherr, S. *et al*. Angiofil: a novel radio-contrast agent for postmortem micro-angiography. *Proc. SPIE* **7078**, 707810 (2008).

41. Müller, B., Fischer, J., Dietz, U., Thurner, P.J. & Beckmann, F. Blood vessel staining in the myocardium for 3D visualization down to the smallest capillaries. *Nucl. Instrum. Meth. Phys, Res, B Beam Interact, Mater, Atoms* **246**, 254–261 (2006).

42. Plouraboué, F. *et al*. X-ray high-resolution vascular network imaging. *J. Microsc.* **215**, 139–148 (2004).

43. Stephenson, R.S. *et al*. Contrast enhanced micro-computed tomography resolves the 3-dimensional morphology of the cardiac conduction system in mammalian hearts. *PLoS ONE* **7**, e35299 (2012).

44. Pai, V.M. *et al*. Coronary artery wall imaging in mice using osmium tetroxide and micro-computed tomography (μ-CT). *J. Anat.* **220**, 514–524 (2012).

45. Stockman, G. & Shapiro, L.G. *Computer Vision* 1st edn. (Prentice Hall PTR, 2001).

46. Frangi, A.F., Niessen, W.J., Vincken, K.L. & Viergever, M.A. In *Medical Image Computing and Computer-Assisted Intervention—Miccai'98*, Vol. 1496 (eds. Wells, W.M., Colchester, A. & Delp, S.) 130–137 (Springer-Verlag, 1998).

47. Pratt, W.K. *Digital Image Processing: Piks Scientific Inside* (John Wiley & Sons, 2007).

48. Grodzins, L. Optimum energies for X-ray transmission tomography of small samples—applications of synchrotron radiation to computerized-tomography 1. *Nucl. Instrum. Methods* **206**, 541–545 (1983).

49. Thurner, P., Beckmann, F. & Müller, B. An optimization procedure for spatial and density resolution in hard X-ray micro-computed tomography. *Nucl. Instrum. Meth. B* **225**, 599–603 (2004).

50. Müller, B. *et al*. Three-dimensional registration of tomography data for quantification in biomaterials science. *Int. J. Mater. Res.* **103**, 242–249 (2012).

51. Weitkamp, T. *et al*. Recent developments in X-ray Talbot interferometry at ESRF-ID19. *Proc. SPIE* **7804**, 780406 (2010).

52. Beckmann, F., Herzen, J., Haibel, A., Müller, B. & Schreyer, A. High density resolution in synchrotron-radiation-based attenuation-contrast microtomography. *Proc. SPIE* **7078**, 70781D (2008).

53. Huesman, R.H. *RECLBL Library Users Manual: Donner Algorithms for Reconstruction Tomography* (Lawrence Berkeley Laboratory, University of California, 1977).

54. Pfeiffer, F., Bunk, O., Kottler, C. & David, C. Tomographic reconstruction of three-dimensional objects from hard X-ray differential phase-contrast projection images. *Nucl. Instrum. Meth. A* **580**, 925–928 (2007).

55. Weitkamp, T., David, C., Kottler, C., Bunk, O. & Pfeiffer, F. Tomography with grating interferometers at low-brilliance sources. *Proc. SPIE* **6318**, 63180S (2006).

56. Preibisch, S., Saalfeld, S. & Tomancak, P. Globally optimal stitching of tiled 3D microscopic image acquisitions. *Bioinformatics* **25**, 1463–1465 (2009).

57. Walter, T. *et al*. Visualization of image data from cells to organisms. *Nat. Methods* **7**, 479–479 (2010).

58. Andronache, A., von Siebenthal, M., Székely, G. & Cattin, P. Non-rigid registration of multi-modal images using both mutual information and cross-correlation. *Med. Image Anal.* **12**, 3–15 (2008).

59. Fierz, F.C. *et al*. The morphology of anisotropic 3D-printed hydroxyapatite scaffolds. *Biomaterials* **29**, 3799–3806 (2008).

60. Kroon, D.-J. & Slump, C.H. MRI modality transformation in demon registration. *IEEE International Symposium on Biomedical Imaging: From Nano to Macro, ISBI '09* (June 28–July 1, 2009, Boston, Massachusetts, USA) 963–966 (2009).

61. Olgac, U., Poulikakos, D., Saur, S.C., Alkadhi, H. & Kurtcuoglu, V. Patient-specific three-dimensional simulation of LDL accumulation in a human left coronary artery in its healthy and atherosclerotic states. *Am. J. Phys.* **296**, H1969–H1982 (2009).

62. Moyle, K.R., Antiga, L. & Steinman, D.A. Inlet conditions for image-based CFD models of the carotid bifurcation: is it reasonable to assume fully developed flow? *J. Biomech. Eng.* **128**, 371–379 (2006).

63. Rikhtegar, F. *et al*. Choosing the optimal wall shear parameter for the prediction of plaque location—a patient-specific computational study in human left coronary arteries. *Atherosclerosis* **221**, 432–437 (2012).

64. van der Giessen, A.G. *et al*. The influence of boundary conditions on wall shear stress distribution in patients specific coronary trees. *J. Biomech.* **44**, 1089–1095 (2011).

65. La Disa, J.F. *et al*. Alterations in regional vascular geometry produced by theoretical stent implantation influence distributions of wall shear stress: Analysis of a curved coronary artery using 3D computational fluid dynamics modeling. *Biomed. Eng. Online* **5**, 40 (2006).

66. Donath, T. *et al*. Toward clinical X-ray phase-contrast CT demonstration of enhanced soft-tissue contrast in human specimen. *Invest. Radiol.* **45**, 445–452 (2010).

67. Hetterich, H. *et al*. Grating-based X-ray phase-contrast tomography of atherosclerotic plaque at high photon energies. *Z. Med. Phys.* **23**, 194–203 (2013).

68. Als-Nielsen, J. & McMorrow, D. *Elements of Modern X-ray Physics* (John Wiley & Sons, 2011).

2.2 Comparison of the morphology of model and explanted human coronary arteries

A combination of advanced laboratory and synchrotron radiation-based micro tomography techniques are combined to non-destructively study the 3D morphology of human, murine and PMMA model arteries. The advantages and disadvantages of each technique are discussed. Intensity-based and region-growing segmentation techniques allow the cross-sectional areas and maximum constrictions to be calculated for each artery. The PMMA model arteries are found to be a good morphological approximation of the studied human coronary artery. The murine artery however is not, and is unsuitable for flow simulations.

Published in Proceedings of SPIE

Morphology of atherosclerotic coronary arteries

Margaret N. Holme[a,b,c], Georg Schulz[a], Hans Deyhle[a], Simone Elke Hieber[a], Timm Weitkamp[d],
Felix Beckmann[e], Julia Herzen[e], Johannes A. Lobrinus[f], Fabrizio Montecucco[c], François Mach[c],
Andreas Zumbuehl[b], Till Saxer[c], and Bert Müller*[a]

[a]Biomaterials Science Center, University of Basel, c/o University Hospital, 4031 Basel, Switzerland;
[b]Department of Chemistry, University of Fribourg, 1700 Fribourg, Switzerland;
[c]Cardiology Division, University Hospitals of Geneva, 1211 Geneva, Switzerland;
[d]Synchrotron Soleil, 91190 Gif-sur-Yvette, France;
[e]Institute of Materials Research, Helmholtz-Zentrum Geesthacht, 21502 Geesthacht, Germany;
[f]Department of Clinical Pathology, University Hospitals of Geneva, 1211 Geneva, Switzerland

ABSTRACT

Atherosclerosis, the narrowing of vessel diameter and build-up of plaques in coronary arteries, leads to an increase in the shear stresses present, which can be used as a physics-based trigger for targeted drug delivery. In order to develop appropriate nanometer-size containers, one has to know the morphology of the critical stenoses with isotropic micrometer resolution. Micro computed tomography in absorption and phase contrast mode provides the necessary spatial resolution and contrast. The present communication describes the pros and cons of the advanced laboratory and synchrotron radiation-based approaches in the visualization of diseased human and murine arteries. Using registered datasets, it also demonstrates that multi-modal imaging, including established histology, is even more powerful. The tomography data were evaluated with respect to cross-section, vessel radius and maximal constriction. The average cross-section of the diseased human artery (2.31 mm^2) was almost an order of magnitude larger than the murine one (0.27 mm^2), whereas the minimal radius differs only by a factor of two (0.51 mm versus 0.24 mm). The maximal constriction, however, was much larger for the human specimen (85% versus 49%). We could also show that a plastic model used for recent experiments in targeted drug delivery represents a very similar morphology, which is, for example, characterized by a maximal constriction of 82%. The tomography data build a sound basis for flow simulations, which allows for conclusions on shear stress distributions in stenosed blood vessels.

Keywords: Atherosclerosis: vessel morphology, shear stress, human coronary artery, mouse model, plaque, micro computed tomography, phase tomography, histology

1. INTRODUCTION

Cardiovascular disease is the number one cause of morbidity and mortality in modern society. In 2008 it was responsible for 30% of all deaths globally [1]. The disease is characterized by the natural progression of lesion formation followed by lipid core expansion, macrophage accumulation and finally formation of a fibrose cap [2]. In the latter stages, the arteries become increasingly rigid and significantly stenosed due to the space occupied by the diseased tissue. In the acute case of plaque rupture, i.e. myocardial infarction (MI), the vasodilator nitroglycerine is often administered to open up and widen the stenosed arteries to allow for the reperfusion of blood before ischemic events. Unfortunately, owing to the systemic effect of such vasodilators, their administration has to be carefully monitored or withdrawn prematurely to minimize the unavoidable side effects such as systemic hypotension.

It is well known that the constriction in critically stenosed arteries leads to local endogenous shear stresses that are significantly higher than those found in the healthy vascular system [3]. Encapsulating the vasodilators (nitroglycerine) in shear-sensitive nanocontainers, e.g. liposomes [4], could alleviate these problems. Targeting shear stresses such as those found in, for example, an 80%-stenosed artery would ensure the drug is delivered to the diseased artery but significantly less to the surrounding healthy vascular system. In order to better understand the local shear stress changes using flow simulations, the morphology of critically stenosed arteries must be uncovered down to the micrometer level.

*bert.mueller@unibas.ch; phone +41 61 265 9659; fax +41 61 265 9699; www.bmc.unibas.ch

The imaging of plaque-containing arteries is challenging, as the simultaneous artifact-free visualization of hard and soft tissue components needs precise knowledge on the preparation including embedding and on the choice of imaging modalities and parameters. Nevertheless, micro computed tomography (μCT) is one of the most powerful techniques that enable the experimentalist to nondestructively image microstructures with isotropic resolution in the three-dimensional (3D) space. The presence of the plaque within the blood vessels means that higher photon energies are required to avoid streak artifacts. This choice, however, leads to a decrease in the density resolution of the soft tissue components since higher energy X rays exhibit much less interaction probability in the conventional absorption contrast. In synchrotron-radiation based μCT in phase contrast mode (phase tomography) using hard X rays this dependence is much weaker [5]. Therefore, phase tomography might be much better suited to visualize the plaque-containing stenosed arteries.

Here, we report data on human and mouse arteries acquired using μCT. Micro computed tomography using a conventional or advanced laboratory setup (laboratory μCT) provides a user-friendly imaging modality that can be rather easily implemented in a research lab, and is suitable for segmenting the lumen morphology and understanding the extent of stenosis in a given vessel. It is also well suited to investigate plastic models of the human vascular system such as those recently applied to demonstrate the efficacy of nanocontainers in targeted drug delivery [4]. One can quantify the degree of occlusion in a polymethylmethacrylate (PMMA) model of the diseased situation with respect to the healthy morphology. Subsequently the model data can be quantitatively compared with the actual morphology of stenosed human or animal arteries. In search of an animal model for further testing of targeted drug delivery and following the advice of international experts, we measured two mouse abdominal aortas using phase SRμCT. One has to recognize that mice have an intrinsically higher shear stress due to their smaller vessel sizes. It is, however, rather simple to breed plaque in their arteries. Tomography data can be the basis of flow simulations to determine how far experiments with small animals resemble the situation of patients.

Phase tomography [6, 7] provides significantly better contrast in soft tissues than both advanced laboratory μCT and SRμCT in absorption contrast mode. Therefore, this approach allows the differentiation between several tissue types similar to well-established histology. We know, however, that the combination of imaging techniques, often termed multi-modal imaging, is even more powerful. In this communication on human coronary arteries we show registered slices of multi-modal imaging.

2. MATERIALS AND METHODS

2.1 PMMA model

Previous *in vitro* studies to evaluate the shear stress sensitivity of nanometer-size vesicles were based on a flow system akin to the human vascular system [4]. The aim of this previous study was to identify lipid formulations that react to endogenous shear stresses in stenosed human coronary arteries as a physical release trigger. For this reason, a PMMA model (Elastrat, Lausanne, Switzerland) of a healthy and diseased artery was built and incorporated into the experimental setup. To assess the morphology of this model and to quantitatively compare it with human vessel morphology, it was visualized using an advanced laboratory μCT by means of a nanotom m (Phoenix|x-ray, GE Sensing & Inspection Technologies GmbH, Wunstorf, Germany) using a 180 kVp / 15 W nanofocus X-ray source. The model was measured with an accelerating voltage of 120 kVp, a beam current of 100 μA, and 2 s exposure time, with a 0.2 mm aluminum filter to increase the mean photon energy. 1000 equiangular projections were recorded over 360° in a field of view of 1300 × 2400 pixels, pixel size 25 μm. Reconstruction of the projections was carried out using a cone beam filtered back-projection algorithm of phoenix datos|x 2.0.1 - RTM (GE Sensing & Inspection Technologies GmbH, Wunstorf, Germany). The reconstructed 3D dataset contains 16-bit values, which correlate to the local X-ray absorption in the specimen.

2.2 Mouse aortas

Apolipoprotein E deficient mice (ApoE-/-) in a C57BL/6J background were obtained from the Charles River Laboratories. At eleven weeks of age, two males were fed with a high-cholesterol diet (HCD; 1.25% cholesterol) for an additional eleven weeks. Then, the animals were euthanized and perfused for five minutes with phosphate buffer saline before the abdominal aortas were collected [8]. These tissues were immediately immersed in 4% paraformaldehyde (PFA) fixative for 24 h before analysis. This protocol was approved by the local ethical committee and Swiss authorities as well as conformed to the 'position of the American Heart Association on Research Animal Use'.

The phase tomography measurements were carried out using a Talbot-Lau interferometer at the beamline W 2 (HASYLAB at DESY, Hamburg, Germany), operated by the HZG Research Center [6, 9]. The grating interferometer consisted of three gratings: the source grating (period 22.9 μm; gold height 130 μm), the phase grating (period 4.33 μm; silicon height about 60 μm) and the analyzer grating (period 2.4 μm; gold height: 150 μm). Source and phase gratings were fabricated at the Paul Scherrer Institut (Villigen, Switzerland). The analyzer gold grating was produced at the Karlsruhe Institute of Technology (Karlsruhe, Germany). The photon energy was set to 31 keV corresponding to the third fractional Talbot order. The X-ray detector consisted of a ~ 580 μm-thick $CdWO_4$ scintillator lens-coupled to a CCD camera. The PL09000 CCD camera (Finger Lakes Instrumentations, New York, USA) had an active area of 3056×3056 pixels, pixel size 12 μm. For each projection a phase-stepping scan was performed, in which a set of images at eight different positions of the phase grating over two periods was recorded. The moderate optical magnification of 5.41 gave rise to an effective pixel size of 2.22 μm with a field of view of 6.77×6.77 mm^2. The spatial resolution determined from a highly absorbing edge in absorption mode was 5.18 μm [10]. Tomographic reconstruction was performed using a modified filter kernel in combination with standard filtered back-projection algorithm [6, 11].

2.3 Multi-modal imaging of atherosclerotic human coronary arteries

Two 2.5 cm-long sections from different human coronary arteries were explanted *post mortem* at the Institute of Forensic Medicine, University Medical Center, Hamburg-Eppendorf. They were subsequently immersed in 4% PFA fixative for more than 10 h, then dehydrated by soaking under reduced pressure overnight in alcohol followed by xylene after which it was immersed in molten paraffin (60 °C) and cooled to room temperature. After SRμCT-measurements (not reported here), the paraffin was removed by heating the artery to 60 °C then washing in a Histokinette (Tissue-TEK VIP E3000) for 12 h under reduced pressure in xylene, alcohol then water. The artery was immersed in decalcifier (distilled water : formic acid : PFA, 87 : 8 : 5 v/v) at a temperature of 37 °C for two days. After complete decalcification, a 2 mL sample of decalcifier in which the artery is immersed does not become milky if mixed with 1 mL ammonium oxalate (5%) and 1 mL ammonia (5%). The artery was then dehydrated and immersed in molten paraffin as described above. Once the paraffin had cooled, the block was trimmed to the part containing the artery and smoothed by rubbing to avoid air bubbles on the surface during measurement.

Advanced laboratory μCT: The morphology of a human coronary artery was assessed first by laboratory μCT using a nanotom m (Phoenix|x-ray, GE Sensing & Inspection Technologies GmbH, Wunstorf, Germany) and 180 kVp / 15 W nanofocus X-ray source, analogously to the PMMA model described above. An accelerating voltage of 60 kVp, a beam current of 310 μA, and 1.2 s exposure time were used together with a 0.5 mm-thick aluminum filter to increase the mean photon energy. 1000 equiangular projections were measured over 360°. The field of view was 1300×2400 pixels, pixel size 17.78 μm. Reconstruction of the projections was carried out using a cone beam filtered back-projection algorithm of the software phoenix datos|x 2.0.1 - RTM (GE Sensing & Inspection Technologies GmbH, Wunstorf, Germany) with a ring artifact removal routine.

Absorption SRμCT: The absorption contrast-based SRμCT measurement was carried out at the beamline BW 2 (HASYLAB, DESY, Germany) operated by the Helmholtz-Zentrum Geesthacht [12]. The highly intense, collimated X-ray beam was monochromatized by means of a fixed-exit double crystal monochromator (Si(111)-crystals) to realize a photon energy of 14 keV with a bandwidth of 0.01%. The tomography set-up was installed 40 m from the radiation source and consisted of the sample manipulator and two-dimensional detection unit. The sample manipulator was used for both precise sample rotation and sample translation, so the photon distribution within the X-ray beam could be recorded without specimen for normalization. The X-ray detection unit was a luminescent screen (500-μm-thick $CdWO_4$ single crystal), optical lens (Nikkor 35 mm focal length, Nikon Inc., Tokyo, Japan), and charge-coupled device (CCD) camera (KX2, Apogee Instruments Inc., Roseville, CA, USA, 14-bit digitization at 1.25 MHz, 1536×1024 pixels, pixel size 9 μm. The incident X rays were converted into visible light by the luminescent screen, projected with the magnification of 3.05 onto the CCD chip [13] resulting in an effective pixel size of 2.95 μm. To increase photon statistics, and therefore the contrast in the reconstructed slices, projections were binned by a factor of two [14]. The spatial resolution determined from a highly absorbing edge was 5.28 μm [11].

Phase tomography: The phase tomography measurement was carried out at the beamline ID 19 (ESRF, Grenoble, France). Artifacts were expected by the strong phase shift at the surface of the artery-containing paraffin block with surrounding air, caused by the prominent difference in decrement of the refractive indexes. To minimize related artifacts, the specimen was immersed in a water bath with parallel PMMA plates arranged perpendicular to the incoming X-ray beam. To ensure that no air bubbles formed on the specimen's surface, it was smoothed by rubbing gently before immersion in the bath. A photon energy of 23 keV was selected using a double-crystal Si(111) monochromator in Bragg

geometry. The specimen was situation 10 cm upstream from the beam-splitter grating (4.785 µm periodicity, 29 µm Si structure height). With a distance between source and interferometer of 150 m and a distance between the gratings of 481 mm (ninth Talbot order), the ratio of the grating periods was matched to the beam divergence [15]. The detector, placed about 3 cm downstream of the analyzer grating with a periodicity of 2.400 µm and a structure height of 50 µm, was a lens-coupled scintillator and CCD system using a FReLoN 2K (Fast-Readout, Low-Noise, ESRF Grenoble, France) CCD with 2048×2048 pixels. The effective pixel size corresponded to 5.4 µm. The field of view was 10.4×11.0 mm^2. Projection radiographs were taken at taken at an angular step size of 0.36° (999 intervals over 360° scan range), with 1.2 s exposure time. At each projection angle, four phase-stepping images were taken over one period of the interferometer fringe pattern. The reader is referred to the literature for detailed descriptions of grating interferometry and of the phase-stepping method [7] and for the details of the instrument used in this study [16]. The phase-contrast projection dataset was reconstructed using a modified filter kernel (Hilbert transform) in combination with a standard filtered back-projection algorithm [17-19].

Histology: The paraffin embedded artery was prepared into 2 to 4 µm-thin lateral sections. Maintaining the artery in the same paraffin embedding ensured the unchanged morphology between µCT-measurements and histological preparation. Since it is time consuming to prepare each slice, the preparation of all sequential slices is impossible within a reasonable time frame. Therefore, every 20th slice from the paraffin ribbon was mounted on a glass slide and stained with Hematoxylin and Eosin (H&E) stain. Each slice was photographed using a Nikon Eclipse 80i microscope and camera at 10× magnification in an average of 20 sections, which were stitched together using the stitching plug-in [20] available in Fiji software (ImageJ version 1.45k, EMBL, Germany) [21] to give color images of on average 4500×5500 pixels, pixel size 0.5 µm.

3. RESULTS

3.1 PMMA model artery

In the center of Figure 1 the model with the two channels that represent a healthy vessel and an atherosclerotic human coronary artery are displayed. One easily recognizes the morphology of the diseased vessel on the left and the morphology of the healthy vessel on the right. The lumen is easily extracted by means of thresholding [22]. The cross-sectional area of the lumen for each vessel in the individual slices is determined using computer code (MATLAB R2010b). The right diagram in Figure 1 with the graph in red color shows the variation of the cross-section as a function of position (height). The value varies by a maximum of 7% between 6.04 and 6.49 mm^2. The diagram on the left in Figure 1 with the blue-colored graph corresponds to the diseased vessel and the cross-sectional area fluctuates between 1.17 and 6.43 mm^2, which is more than a factor of five. This means that the maximal cross section in both cases is identical within the error bars, whereas the minimal cross sections differ by more than a factor of five.
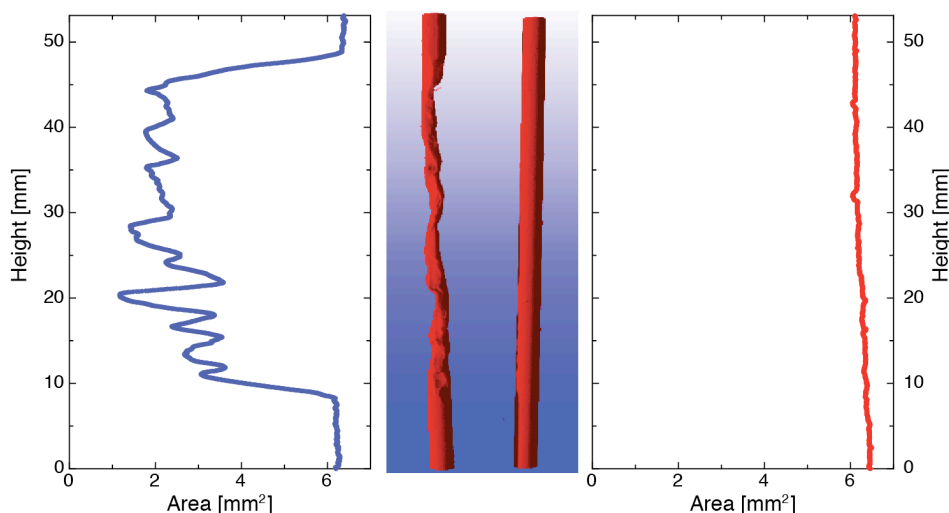

Figure 1. Cross-sectional area of the inner volume of a diseased (left) and healthy (right) artery model derived from laboratory µCT measurements. In the center, the data are represented as 3D rendering.

3.2 Mouse aortas

The mouse abdominal aortas were investigated using synchrotron radiation-based phase tomography to determine their morphology on the micrometer scale. The vessel walls exhibited a larger real part of the refractive index in comparison with the surrounding tissues and PFA solution in the Eppendorf container. Thus, it was rather simple to segment the lumen (see Figure 2) using the region-growing tool in VG Studio Max 2.1 (Volume Graphics, Heidelberg, Germany). The associated 3D renderings in Figure 2 were generated in VG Studio Max 2.1 by means of thresholding [22] and rendered using the settings Volume Renderer (Scatter HQ) (Figure 2, top, bisected artery) and Scatter HQ (v1.2) (Figure 2, bottom left).
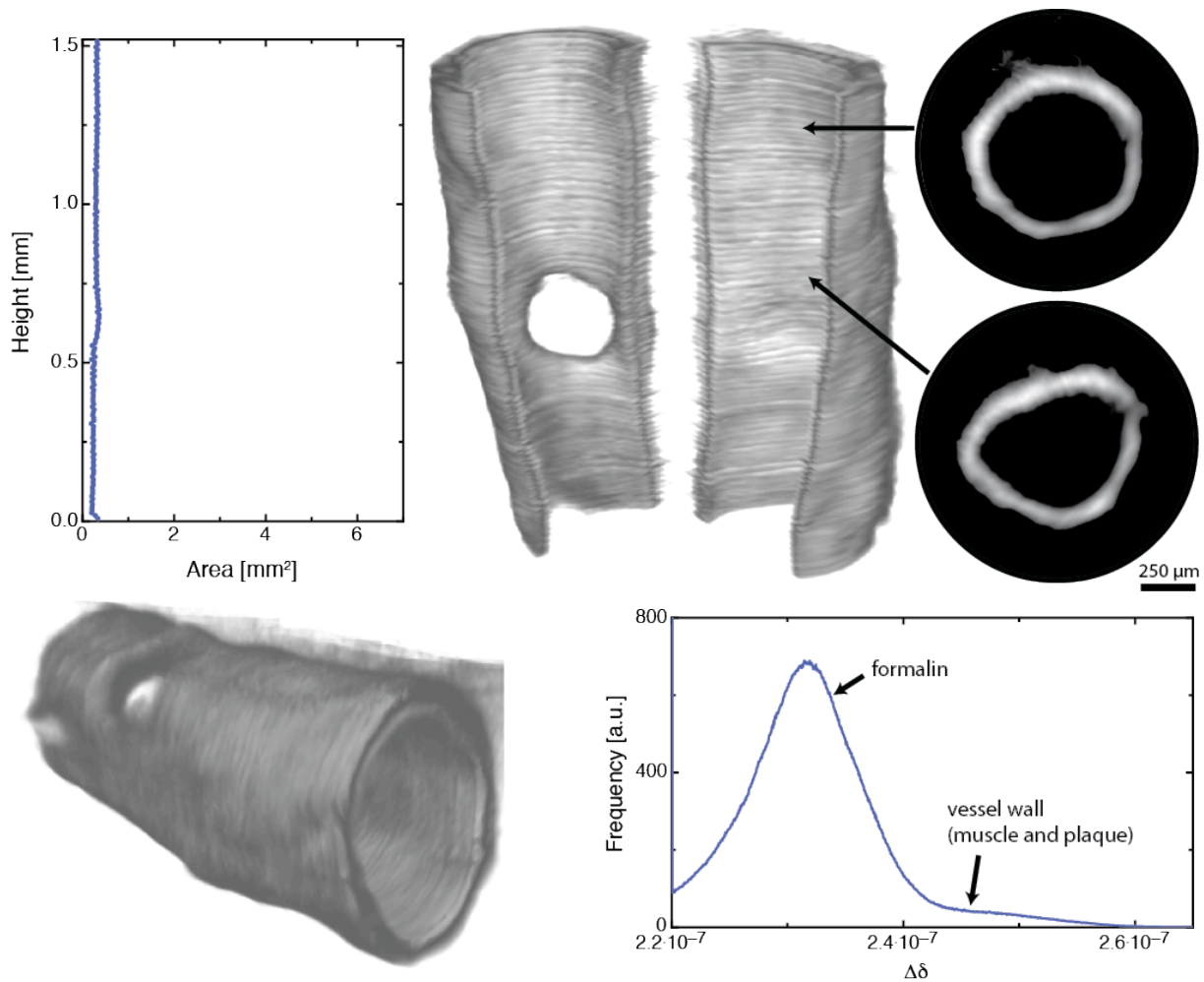
Figure 2: Morphology of a stenosed mouse aorta from a phase SRμCT measurement. Top, left to right: diagram of the cross sectional area of the lumen with axes comparable to the diagrams in Figure 1, 3D rendering of the artery bisected and opened up down the middle, with two selected cross-sectional slices. Bottom left to right: 3D rendering of the entire mouse aorta, histogram of the 3D tomography data to elucidate differences in the real part of the refractive index.

Unfortunately, it was impossible to differentiate between the expected plaque and the arterial wall tissue. The histogram in Figure 2 only exhibits a shoulder of the main peak that might be caused from plaque formed. The hole easily recognized in the artery wall resulted from a bifurcation. Here, the vessel was trimmed off during specimen preparation.

The lumen of the mouse aorta has a cross-sectional area that ranges from 0.19 to 0.37 mm^2. This means that the variation is below 50%. The 3D rendering illustrates that the lumen is rather straight and does not resemble the

morphology of a common stenosis in man. The periodic ripples along the vessel are artifacts that originate from insufficient background correction and can be removed by post-processing, which was not performed for the presented dataset.

3.3 Imaging an atherosclerotic human coronary artery

Three selected slices from the phase tomography and laboratory μCT were successfully registered in 2D space (Figures 3 and 4). This is a prerequisite to directly compare the performance of the two techniques. Registration was performed using a code developed by Kroon and Slump (multimodality non-rigid demon algorithm image registration [23]) in MATLAB 2010b with a scaling factor in the affine non-rigid registration. The two approaches provide similar information about the different tissue types and the paraffin embedding. Comparing the selected slices from the two approaches, however, the distinction is clearer in phase tomography than in the conventional μCT data. This qualitative observation is corroborated using the joint histograms represented between the slices. They are almost symmetric along the diagonal, a sign that both approaches are comparable in performance. One can clearly distinguish the paraffin (a), the soft tissues including muscles (b), and the plaque (c). The peaks of the components, however, have different half widths. For example, the paraffin peak is narrower for the phase tomography than for the advanced laboratory μCT, giving rise to an oval shape in the joint histogram (a).
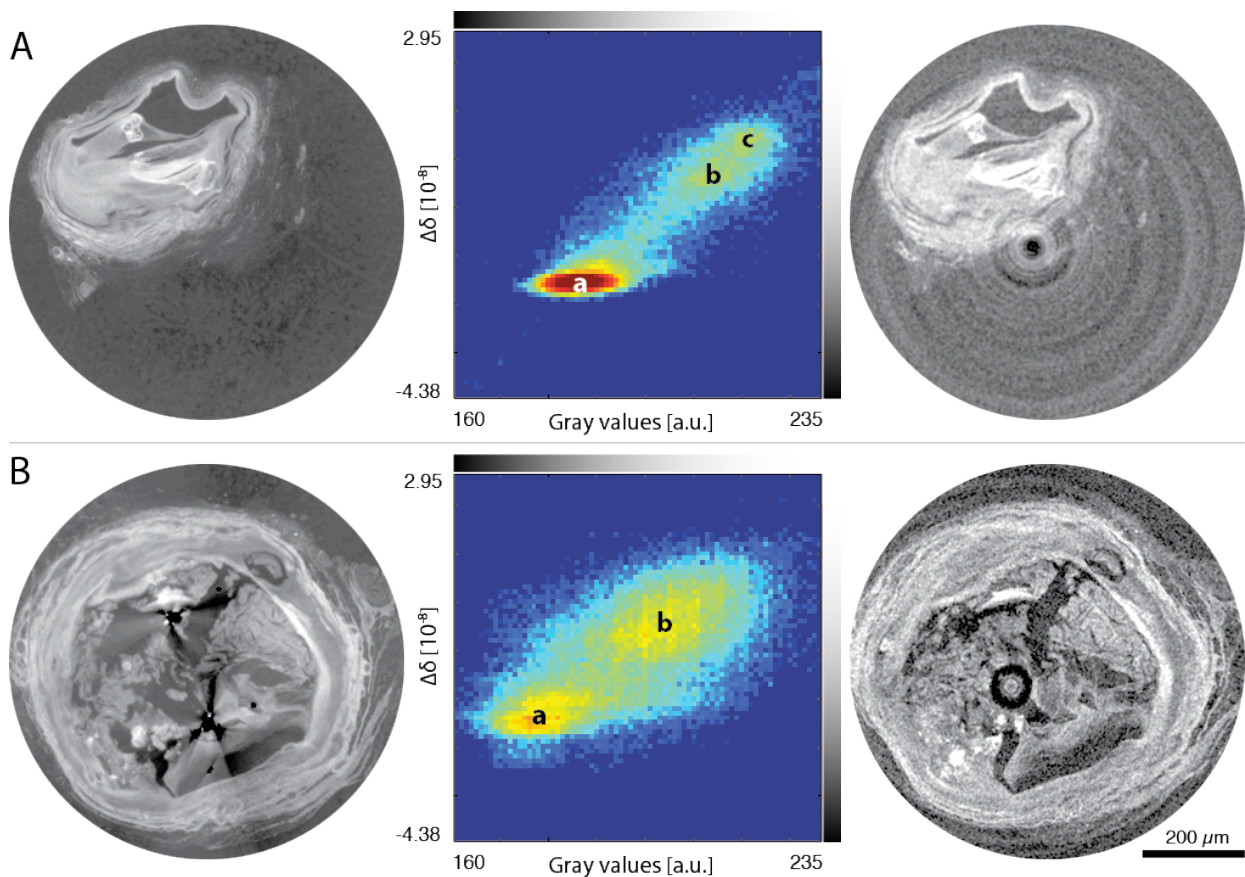
Figure 3. Comparison of phase tomography using synchrotron radiation and laboratory μCT for the extraction of lumen morphology. A and B show for two selected slices of the phase tomography (left), the joint histogram (center) and the laboratory μCT data (right). The joint histograms can be used to segment tissues by comparing the different gray-scale values in the slices, i.e. paraffin (indicated by a), muscle and soft tissues (b), and plaque (c).

The data does not allow an easy identification of different tissue types. Experts in anatomy can differentiate between the tissues because of their expertise and slightly preferred the quality of the phase tomography data. Here, they identified tissue structures such as smooth tissues, foamy cells, muscle walls and cholesterol. It has to be mentioned,

however, that the ring artifacts, which are much more prominent in the laboratory μCT data, create major peak broadening especially for the paraffin. The application of ring artifact corrections led to an inhomogeneous background in the laboratory μCT dataset not observed in the phase tomography data.

For flow simulations in the blood vessel system, the lumen of the stenosed vessels has to be determined. Although the phase tomography provides better contrast for tissue differentiation, the SRμCT in the absorption contrast mode is much better suited for lumen segmentation. This surprising result is due to the nature of the artifacts present. In phase tomography, artifacts from the air bubbles led to such high differences in local Δδ-values that the intensity-based segmentation by region-growing was impossible (cp. slice shown in Figure 4). The ring artifacts observed in laboratory μCT do not interfere with the segmentation procedure in the same manner. Therefore, the lumen from the data of the laboratory μCT was extracted from the 4.9 mm-long section of the artery (one slice given in Figure 4) using the region-growing tool of the software VG Studio Max 2.1 (Volume Graphics, Heidelberg, Germany). The cross-sectional area was analyzed using computer code (MATLAB R2010b). The artery showed a minimal cross-section of 0.83 mm^2 and a maximum cross-section of 5.60 mm^2. This means the constriction corresponds to 85%.
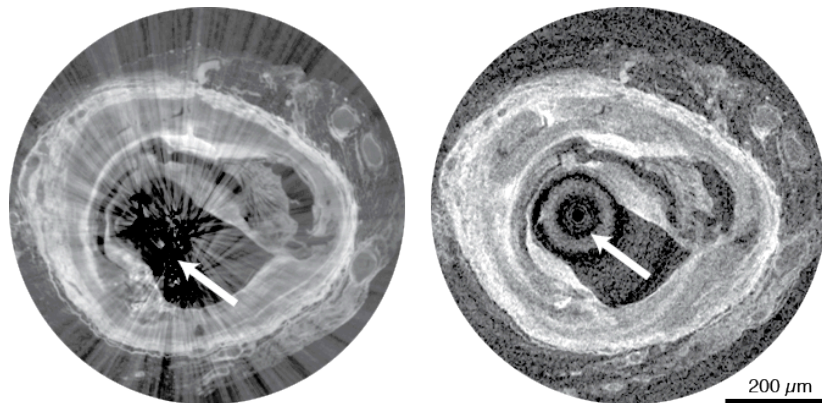
Figure 4. Comparison of phase tomography (left slice) and laboratory μCT (right slice) using a slice that contains an air bubble. The trapped air causes artifacts that prevent the segmentation of the vessel lumen in phase tomography data.

3.4 Multi-modal imaging of a slice of an atherosclerotic human coronary artery

The combination of modalities often yields additional information. Therefore, the combination of the tomography data with the histology might give additional insights into the tissue morphology. While tomography data contain X-ray absorption values and the real part of the refractive index for phase tomography, histology provides functional information depending on the stain applied. The disadvantage of histology, however, is the tremendous effort for serial sectioning and the limited spatial resolution in the third dimension, perpendicular to the slices. As a consequence researchers usually only prepare a limited number of histological slices. A 3D dataset of histological data is rarely generated.

An H&E-stained histological slice was prepared from the atherosclerotic human coronary artery after the decalcification and nondestructive μCT data acquisition. This slice was registered with the datasets from absorption-based SRμCT and phase tomography in the manner described above. The three related slices are displayed in Figure 5: the phase SRμCT data using red color, the absorption SRμCT-data with green color, and the histology slice using the blue color. The superposition of the slices given in the bottom right of Figure 5 supplies an image that highlights the relative contributions.

The phase tomography slice, given in red, exhibits the biggest contrast between tissue types. The foamy cell region specified by the white circle in the RGB composite contains very low Δδ values characterized using dark colors (almost black). In the phase SRμCT slice, the relatively high Δδ values characterized by bright red originate from plaque. An air bubble enclosed in the paraffin created the striking artifact, i.e. the pair of well-localized high brightness streaks highlighted by the white arrow.

Although the contrast between tissue types of the absorption SRμCT-slice (green color) is lower than in phase tomography, one recognizes the artifacts from the residual plaque. This observation indicates that the decalcification

procedure was incomplete. Such an incomplete plaque extraction, however, can be an advantage, since the location of plaque is identified without strong streak artifacts.

The histological slice provides a higher spatial resolution than absorption SRμCT and phase tomography slices. Thus, the details of the anatomical microstructures are more easily visible. The microstructures are similar in the three slices. There are, however, some noteworthy observations. The foamy cells and fat correspond to the green part of the RGB image, since these tissue types show up as black or very dark areas in the phase tomography and histology. The plaque is bright pink, as it is brightest in the phase tomography. The phase tomography and histology contribute mainly to the muscle and vessel walls, so they appear violet. The artifacts from the air bubble in phase tomography are prominent.
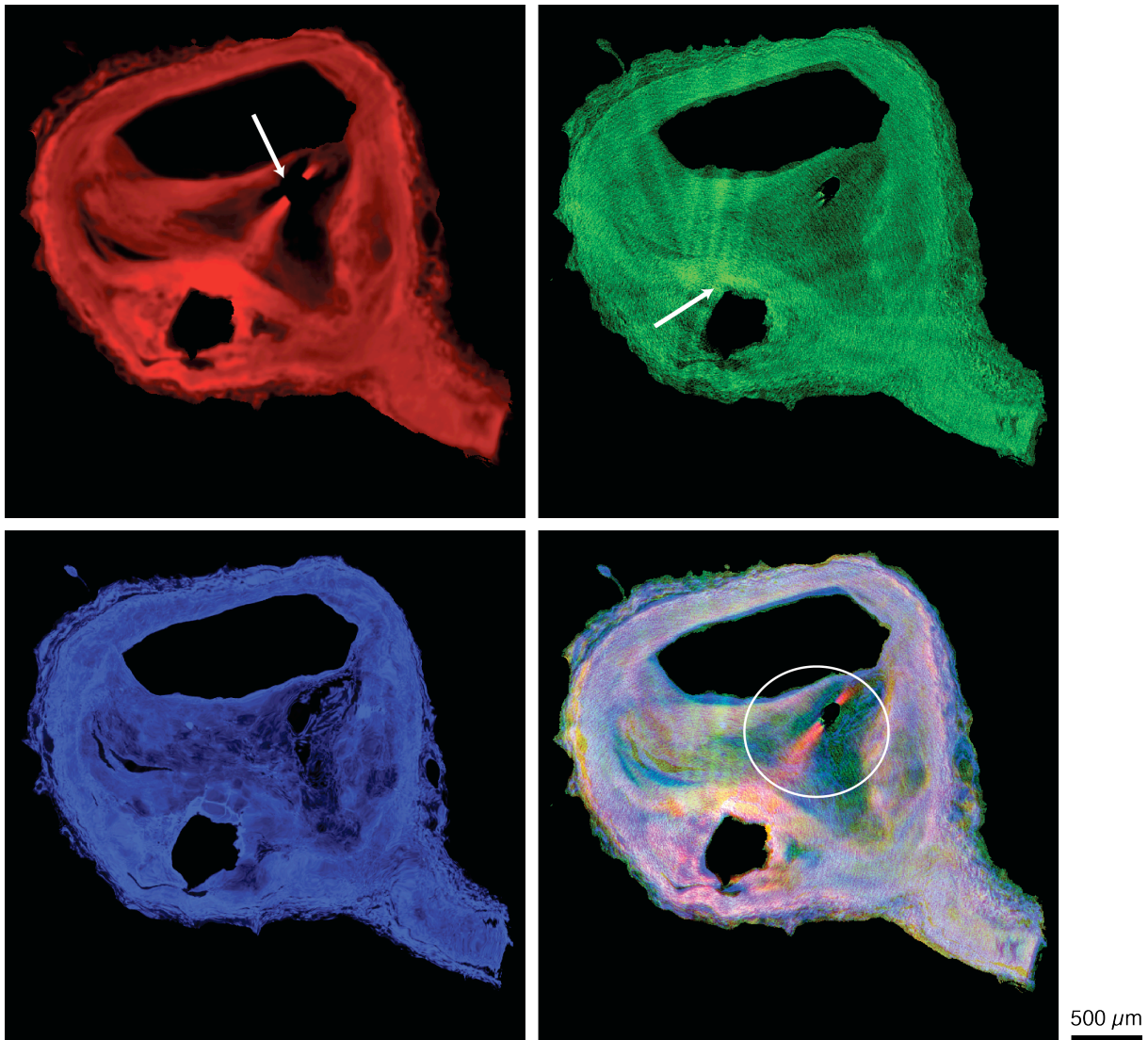
Figure 5: Comparison of phase tomography (red), absorption SRμCT (green) and histology (blue) techniques for visualizing tissue types in a stenosed human coronary artery. Arrows indicate sources of artifacts: air bubble (phase tomography) and residual plaque (absorption SRμCT). Bottom right: RGB composite image of the slices obtained from the three modalities. The white circle indicates the foamy cell region. The slice is situated just before a bifurcation. The protrusion in the bottom right of each image is the wall of the bifurcated artery. Dynamic range: The histogram of each image has been scaled to include only the tissue related peaks with values ranging from 0 to 255.

3.5 Arterial cross-section and extent of constriction

Table 1 lists the cross-sectional areas of the lumens derived from tomography data of the PMMA model, the mouse aorta and the human atherosclerotic artery. The constriction was calculated from the ratio of the cross-sectional areas, i.e. minimal cross-section divided by the maximal cross-section. Assuming a circularly shaped vessel, one finds the radius at the maximum stenosis, which is more common in literature.

Table 1. Morphological parameters of PMMA model, mouse, and atherosclerotic human vessels.

	Cross-section area [mm^2]				Maximum constriction [%]	Minimum radius [mm]
	Average	Maximum	Minimum	Std. dev.		
PMMA-model (healthy)	6.23	6.49	6.04	0.12	6.9	1.39
PMMA-model (diseased)	3.52	6.43	1.17	1.78	81.8	0.61
Mouse aorta	0.27	0.37	0.19	0.04	49.4	0.24
Human artery	2.31	5.60	0.83	1.36	85.2	0.51

4. DISCUSSION

4.1 Morphology of mouse artery

The mouse artery illustrated in Figure 2 show the challenge in the visualization of small specimens using grating-based phase tomography. During the grating interferometry experiment at the beamline W 2 the choice of the parameters was suboptimal. The third Talbot order, for example, leads to less sensitive images compared to the ninth Talbot order at the beamline ID 19. Due to beamtime restrictions, the experiment was carried out at a photon energy of 31 keV and not of 23 keV. The reduction of the energy leads to a higher sensitivity of the experimental setup. Despite these challenges, the phase tomography at the W 2 beamline was sufficient to segment the lumen of the mouse artery, which was the imaging task of the experiment. It was impossible to obtain the same image quality with conventional absorption-contrast tomography.

Although there is no constriction due to disease, the artery tapers to one end, giving rise to a maximum constriction of 49.4%. The average cross-sectional area of 0.27 mm^2 (Table 1) corresponds to a 96% occlusion of a human coronary artery of 2.5 mm diameter. Due to these favorable dimensions, the mouse aorta could potentially be of use in flow studies or *in vivo* experiments for, e. g. testing the localized release of a marker from shear-sensitive nanocontainers. However, unlike the PMMA-model and human arteries, the mouse aorta is a continuous tube with no sudden change in cross-sectional area. The investigated section has a standard deviation of only 0.04 mm^2, approximately 2% that of the PMMA model and human arteries. Additionally, we were unable to identify any calcified plaques. It is possible that the animal's lifetime was insufficient to allow formation of calcified plaques, and that the disease model is not sufficiently representative of the pathology observed in human cases for these studies. This puts into question the usefulness of a mouse model for evaluating the role of shear stress in, e. g. targeted drug delivery in the human heart, cp. the recent paper of D. Ingber's team [24]. Vortex formation and re-flow phenomena have been observed in flow simulations where the morphology has a major role in determining local shear stresses. It must be validated whether the aorta can be successfully connected to a flow system, whether the lack of plaque and diseased tissue could lead to a difference in drug metabolism, and (with flow simulations) whether such a smooth morphology is an appropriate model.

4.2 Micro-morphology of atherosclerotic human coronary arteries

Registered slices of a human coronary artery measured by laboratory µCT and phase tomography (Figures 3 and 4) were examined for their usefulness a) as modalities for identifying different tissues types, and b) for segmenting the non-constricted cross-sectional area. The methods provide complementary results and the nature of the artifacts determined the limits of each dataset.

Laboratory µCT showed ring artifacts, which did not interfere with the segmentation tool (VG Studio Max 2.1, Heidelberg, Germany) used to extract the non-constricted cross-sectional area. This imaging modality is a fast, convenient method for extracting data about the lumen morphology (Table 1). However, the artifacts from the highly

absorbing plaque obscured the morphology of the calcified regions and led to a broadening of the histogram compared to phase tomography (Figure 3). Coupled with the larger pixel size of 17.78 μm, it was impossible to identify all microstructures and therefore different tissue types. In contrast, phase tomography showed starburst artifacts caused by air bubbles in the paraffin formed during the embedding process (see Figures 4 and 5, phase tomography image, white arrow). This made segmentation of the lumen cross-sectional area impossible, but experts could identify different tissue types (foamy cells, calcifications, muscle etc.) and unstable plaques in phase tomography data by comparison with histology (Figure 5).

To see whether identification of different tissue types could be achieved in absorption-based tomography, absorption SRμCT was also used as an imaging modality (Figure 5). Unfortunately, artifacts caused by the highly absorbing residual plaque (Figure 5, absorption SRμCT image, white arrow) also made it impossible for the experts to reliably identify different soft tissue types.

Defining a critical stenosis is non trivial. The constriction is often defined in terms of reduction in diameter or cross-sectional area [25-28], but can also be considered in terms of fractional or coronary flow reserve [29]. Accuracy of detection methods also influences results. For example, synchrotron radiation coronary angiography is able to detect diameters of down to 100 μm in beating hearts versus 400 μm in conventional angiography [25]. Reports of 99% stenosis by diameter in the literature are common [25], although often stenoses are only qualitatively characterized as 'severe'. Nielsen and co-workers define stenosis as >70% constriction and healthy as <30% constriction [30], whereas DeMaria et al. define significant stenosis as >50% [31]. However, such basic criteria may be misleading, since the hemodynamic effect also depends on the lesion length, blood viscosity and laminar flow characteristics that dictate flow velocity and wall shear stresses [32]. Other studies consider ≥75% stenoses by diameter as critical [33]. ST-elevation myocardial infarction (STEMI) occurs when a culprit lesion completely blocks a vessel. Therefore, 81.8% constriction by diameter as seen in this study is a reasonable model for targeting the culprit lesion whilst avoiding most other, non-critical, stenoses.

4.3 PMMA-model to reproduce the morphology of healthy and atherosclerotic human coronary arteries

We were able to show that the PMMA-model presented similar morphology to a stenosed human coronary artery and was within a reasonable range according to the literature, and, therefore, appropriate to use in shear-release experiments as reported previously [4]. The maximum diameter of the healthy and diseased PMMA-model arteries is identical within error bars. The average diameter of the healthy artery PMMA model is 2.82 mm, within the values reported *in vivo* (normally 2 to 3 mm). The diseased artery PMMA-model exhibits a maximum occlusion of 81.8% cross-sectional area, corresponding to a minimum radius of 0.61 mm (Table 1). This is in accordance with constrictions reported in the latter stages of atherosclerosis based on measurements using, for example, angiography [34]. A critically stenosed artery (>80% stenosis) is of interest for studying release of a drug from a shear-stress sensitive nanocontainer [4]. The diseased model artery is within 1.8% of this value. Therefore, it is a reasonable approximation of a stenosed artery for further studies.

The human artery and diseased PMMA-model have similar properties, with the human artery possessing an 85.2% maximum constriction by cross sectional area versus 81.8% in the diseased PMMA model. This corresponds to a minimum radius of 0.51 and 0.61 mm respectively. The human artery has generally 10% smaller dimensions, with a maximum cross-sectional area of 5.60 mm^2 versus 6.27 mm^2 for the PMMA models. However, it shows slightly less range in occlusion, illustrated by a smaller standard deviation in cross-sectional area (1.36 mm^2 versus 1.78 mm^2 in the diseased PMMA model).

The PMMA model has a morphology that shows similar characteristics to the *in vivo* situation and is therefore very helpful for identification of nanocontainer formulations suitable for clinical studies, maybe even without any animal testing.

5. CONCLUSIONS

The PMMA model cross-sectional areas correspond well to the literature values in the case of both the healthy and diseased artery, with the latter falling in the severely stenosed category. Such a model is highly desirable for testing the suitability of shear stress sensitive nanocontainers as drug delivery vectors.

The mouse aorta, although it is not stenosed to 80%, does present the cross-sectional area corresponding to a 96% constriction of a 2.5 mm diameter human coronary artery. This is slightly higher than desired for testing the suitability of

shear stress sensitive nanocontainers. Although the constriction is a model for a critically stenosed artery, such as in, e. g. ST-segment elevation MI (STEMI), its usefulness as a morphological model is limited, since it has a smooth morphology.

Phase tomography gives high contrast images from which different tissues types can be identified by comparison with histology. However, artifacts from air bubbles make segmentation of the lumen unfeasible. This might be overcome by using PFA as a storage medium in place of paraffin. It is a useful tool for identifying the 3D morphology of tissue composition in decalcified human coronary arteries, when compared to histology as a reference. Laboratory μCT and absorption SRμCT do not provide as much resolution of different tissue types, but are more appropriate for the extraction of the artery lumen. Artifacts in phase tomography from air bubbles introduced in the paraffin embedding are more problematic in the segmentation procedure than the ring artifacts caused by residual plaque in laboratory μCT and absorption SRμCT. The various analysis tools provide a complementary analysis of tissue structure and morphology. A decalcified human coronary artery was found to present the desired morphology for testing the suitability of shear stress sensitive nanocontainers as drug delivery vectors.

ACKNOWLEDGEMENTS

REFERENCES

[1]   [Fact sheet N°317, www.who.int] World Health Organisation, (September 2011).

[2]   V. Fuster, P. R. Moreno, Z. A. Fayad *et al.*, "Atherothrombosis and high-risk plaque: Part I: Evolving concepts," J. Am. Coll. Cardiol.*, 46(6), 937-954 (2005).

[3]   C. Cheng, F. Helderman, D. Tempel *et al.*, "Large variations in absolute wall shear stress levels within one species and between species," Atherosclerosis*, 195(2), 225-235 (2007).

[4]   M. N. Holme, I. A. Fedotenko, D. Abegg *et al.*, "Shear-stress sensitive lenticular vesicles for targeted drug delivery," Nature Nanotech.*, 7(8), 536-543 (2012).

[5]   U. Bonse, and F. Busch, "X-ray computed microtomography (μCT) using synchrotron radiation (SR)," Prog. Biophys. Mol. Biol.*, 65(1), 133-169 (1996).

[6]   J. Herzen, F. Beckmann, T. Donath *et al.*, "X-ray grating interferometer for imaging at a second-generation synchrotron radiation source," Proc. SPIE*, 7804, 780407 (2010).

[7]   T. Weitkamp, A. Diaz, C. David *et al.*, "X-ray phase imaging with a grating interferometer," Opt. Express*, 13(16), 6296-6304 (2005).

[8]   V. Braunersreuther, A. Zernecke, C. Arnaud *et al.*, "Ccr5 but not Ccr1 deficiency reduces development of diet-induced atherosclerosis in mice," Arterioscler. Thromb. Vasc. Biol.*, 27(2), 373-379 (2007).

[9]   J. Herzen, T. Donath, F. Beckmann *et al.*, "X-ray grating interferometer for materials-science imaging at a low-coherent wiggler source," Rev. Sci. Instrum.*, 82(11), 113711 (2011).

[10]   S. H. Irsen, B. Leukers, C. Tille *et al.*, "Image based analysis of bone graft samples made by 3D printing using conventional and synchrotron-radiation-based micro-computed tomography," Adv. Med. Eng.*, 114, 121-126 (2007).

[11]   B. Müller, G. Schulz, J. Herzen *et al.*, "Morphology of urethral tissues," Proc. SPIE*, 7804, 78040D (2010).

[12]   F. Beckmann, J. Herzen, A. Haibel *et al.*, "High density resolution in synchrotron-radiation-based attenuation-contrast microtomography," Proc. SPIE*, 7078, 70781D (2008).

[13] A. Lareida, F. Beckmann, A. Schrott-Fischer *et al.*, "High-resolution X-ray tomography of the human inner ear: synchrotron radiation-based study of nerve fibre bundles, membranes and ganglion cells," J. Microsc.*, 234(1), 95-102 (2009).

[14] P. Thurner, F. Beckmann, and B. Müller, "An optimization procedure for spatial and density resolution in hard X-ray micro-computed tomography," Nucl. Instrum. Methods Phys. Res. Sect. B*, 225(4), 599-603 (2004).

[15] T. Weitkamp, C. David, C. Kottler *et al.*, "Tomography with grating interferometers at low-brilliance sources," Proc. SPIE*, 6318, 63180S (2006).

[16] T. Weitkamp, I. Zenette, C. David *et al.*, "Recent developments in X-ray Talbot interferometry at ESRF-ID19," Proc. SPIE*, 7804, 780406 (2010).

[17] G. W. Faris, and R. L. Byer, "Three-dimensional beam-deflection optical tomography of a supersonic jet," Appl. Opt.*, 27(24), 5202-5212 (1988).

[18] F. Pfeiffer, O. Bunk, C. David *et al.*, "High-resolution brain tumor visualization using three-dimensional x-ray phase contrast tomography," Phys. Med. Biol.*, 52, 6923-6930 (2007).

[19] F. Pfeiffer, O. Bunk, C. Kottler *et al.*, "Tomographic reconstruction of three-dimensional objects from hard X-ray differential phase contrast projection images," Nucl. Instrum. Methods Phys. Res. Sect. A*, 580(2), 925-928 (2007).

[20] S. Preibisch, S. Saalfeld, and P. Tomancak, "Globally optimal stitching of tiled 3D microscopic image acquisitions," Bioinformatics*, 25(11), 1463-1465 (2009).

[21] T. Walter, D. W. Shattuck, R. Baldock *et al.*, "Visualization of image data from cells to organisms," Nat. Methods*, 7(6), 479-479 (2010).

[22] B. Müller, F. Beckmann, M. Huser *et al.*, "Non-destructive three-dimensional evaluation of a polymer sponge by micro-tomography using synchrotron radiation," Biomol. Eng.*, 19(2), 73-78 (2002).

[23] D.-J. Kroon, and C. H. Slump, "MRI modalitiy transformation in demon registration," IEEE, 963-966 (2009).

[24] N. Korin, M. Kanapathipillai, B. D. Matthews *et al.*, "Shear-Activated Nanotherapeutics for Drug Targeting to Obstructed Blood Vessels," Science*, 337(6095), 738-742 (2012).

[25] S. Matsushita, K. Hyodo, T. Imazuru *et al.*, "The minimum coronary artery diameter in which coronary spasm can be identified by synchrotron radiation coronary angiography," Eur. J. Radiol.*, 68(3, Supplement), S84-S88 (2008).

[26] T. Hozumi, K. Yoshida, T. Akasaka *et al.*, "Noninvasive assessment of coronary flow velocity and coronary flow velocity reserve in the left anterior descending coronary artery by Doppler echocardiography: Comparison with invasive technique," J. Am. Coll. Cardiol.*, 32(5), 1251-1259 (1998).

[27] D. Hackett, J. Verwilghen, G. Davies *et al.*, "Coronary stenoses before and after acute myocardial infarction," Am. J. Cardiol.*, 63(20), 1517-1518 (1989).

[28] C. M. Gibson, L. Diaz, K. Kandarpa *et al.*, "Relation of vessel wall shear stress to atherosclerosis progression in human coronary arteries," Arterioscler. Thromb. Vasc. Biol.*, 13(2), 310-315 (1993).

[29] E. Shalman, M. Rosenfeld, E. Dgany *et al.*, "Numerical modeling of the flow in stenosed coronary artery. The relationship between main hemodynamic parameters," Comp. Biol. Medicine*, 32(5), 329-344 (2002).

[30] M. Bøttcher, M. M. Madsen, F. Randsbæk *et al.*, "Effect of oral nitroglycerin and cold stress on myocardial perfusion in areas subtended by stenosed and nonstenosed coronary arteries," Am. J. Cardiol.*, 89(9), 1019-1024 (2002).

[31] M. Yamagishi, S. E. Nissen, D. C. Booth *et al.*, "Coronary reactivity to nitroglycerin: Intravascular ultrasound evidence for the importance of plaque distribution," J. Am. Coll. Cardiol.*, 25(1), 224-230 (1995).

[32] E. O. Ofili, M. J. Kern, A. J. Labovitz *et al.*, "Analysis of coronary blood flow velocity dynamics in angiographicaily normal and stenosed arteries before and after endolumen enlargement by angioplasty," J. Am. Coll. Cardiol.*, 21(2), 308-316 (1993).

[33] C. Bertolotti, and V. Deplano, "Three-dimensional numerical simulations of flow through a stenosed coronary bypass," J. Biomech.*, 33(8), 1011-1022 (2000).

[34] F. Ledru, P. Théroux, J. Lespérance *et al.*, "Geometric features of coronary artery lesions favoring acute occlusion and myocardial infarction: a quantitative angiographic study," J. Am. Coll. Cardiol.*, 33(5), 1353-1361 (1999).

2.3 Proof of principle: Mechano-sensitive nano-containers for targeted drug delivery to constricted vessels in the heart

The following highlighted article [73] is the first proof of principle that mechano-sensitive nano-containers can be engineered to release their contents selectively and rapidly at shear stresses such as those found in critically constricted human coronary arteries. In vitro results using a physiologically relevant healthy and critically constricted PMMA model artery show the critically constricted model increases content release from such nano-containers by 25% after only one pass.

Published in Nature Nanotechnology

2.3 Proof of principle: Mechano-sensitive nano-containers for targeted drug delivery to constricted vessels in the heart

43

Shear-stress sensitive lenticular vesicles for targeted drug delivery

Margaret N. Holme[1,2,3], Illya A. Fedotenko[1], Daniel Abegg[1], Jasmin Althaus[2], Lucille Babel[1], France Favarger[1], Renate Reiter[4], Radu Tanasescu[1], Pierre-Léonard Zaffalon[1], André Ziegler[5], Bert Müller[2]*, Till Saxer[3]* and Andreas Zumbuehl[1]*

Atherosclerosis results in the narrowing of arterial blood vessels and this causes significant changes in the endogenous shear stress between healthy and constricted arteries. Nanocontainers that can release drugs locally with such rheological changes can be very useful. Here, we show that vesicles made from an artificial 1,3-diaminophospholipid are stable under static conditions but release their contents at elevated shear stress. These vesicles have a lenticular morphology, which potentially leads to instabilities along their equator. Using a model cardiovascular system based on polymer tubes and an external pump to represent shear stress in healthy and constricted vessels of the heart, we show that drugs preferentially release from the vesicles in constricted vessels that have high shear stress.

Liposomes are well-established drug delivery systems[1] and are vesicular in shape with an aqueous inner cavity. They are formed spontaneously when amphiphatic phospholipids contact water and align into mechanically stable bilayers. The bilayer protects the aqueous cavity and its drug contents from chemical and biological reactions before the vesicle arrives at the target tissue[1].

One way to trigger the release of drugs from liposomes is to engineer liposomes that are sensitive to mechanical stress. Conventional spherical liposomes are highly stable to mechanical stress. Computer simulations have previously shown that lenticular (or lentil-shaped) nanocontainers formulated from membranes with large bending moduli are intrinsically more stable than their spherical counterparts[2]. However, the relationship between vesicle shape, stability to mechanical stress and atomic structure has not been shown experimentally.

Non-spherical vesicles were described more than 30 years ago. For example, unilamellar vesicles (diameter, 30 nm) formulated from dipalmitoyl phosphatidyl choline (DPPC) demonstrate X-ray patterns predicted for faceted particles in the form of truncated icosahedra[3]. This morphology is probably induced by the hexagonal packing of lipids in the gel state, but it is found only at the low ionic strength of dilute salt solutions[4]. However, high curvature in small unilamellar vesicles was found to lead to packing defects that could be eliminated only through spontaneous fusion to form spherical 70 nm unilamellar vesicles[5,6]. Other icosahedral vesicles formed from a mixture of cationic and anionic surfactants also required salt-free conditions to form[7,8], and these vesicles would dissociate at the isotonic sodium chloride concentrations needed for drug delivery.

To make non-spherical vesicles, lipid membranes need to have large bending moduli (that is, exist in a gel phase)[2]. This feature can be introduced by exchanging the ester bonds of natural phospholipids for artificial amides that stabilize the interfacial region through hydrogen bonds. So far, the introduction of amides[9–11] or carbamates[12] has been inspired by the design of serum-stable, phospholipase A-resistant lipids that have potential anti-HIV and anticancer properties. In these approaches, the amido fatty-acid tails replace the esters at the sn-1, sn-2 or both positions. It was not until recently that symmetrical insertion of carbohydrate fatty amides at the 1- and 3-positions and a residual phosphate ester at the 2-position was reported[13,14]. The shear-stress resistance of the amido-phospholipids is unknown but some data suggest that additional hydrogen bonding may make the vesicles more stable and less prone to drug release[11,12].

Based on these considerations, we hypothesized that endogenous shear stress in critically constricted blood vessels (such as those found in atherosclerotic patients) might lead to transient pore formation in lenticular vesicles. Our results show that the lenticular vesicles preferentially release drugs in a model cardiovascular system, suggesting that such vesicles may potentially be used to treat cardiovascular diseases in a targeted manner.

A new diamidophosphocholine forms faceted vesicles

A recent publication reported the synthesis of amide-bearing phosphoethanolamines[13]. As most of these molecules are insoluble in organic solvents, the terminal amines were quaternized, which greatly improved the solubility. The synthesis of amide-bearing 1,3-dipalmitamidopropan-2-yl 2-(trimethylammonio)ethyl phosphate (Pad–PC–Pad, **1**) (Fig. 1, see ref. 13 for nomenclature) was achieved by exhaustive methylation with dimethylsulphate from the corresponding ethanolamine precursor (see Methods and Supplementary Section S1.1). The final compound was purified by silica gel and gel permeation column chromatography.

The artificial phospholipid Pad–PC–Pad contains two amide bonds, intended to stabilize the polar region of the membrane through additional hydrogen bonds. Indeed, a shorter 1,2-dimyristamidopropan-2-yl 3-(trimethylammonio)ethyl phosphate Mad–Mad–PC

[1]University of Geneva, Department of Organic Chemistry, Quai Ernest-Ansermet 30, 1211 Geneva, Switzerland, [2]Biomaterials Science Center (BMC), University of Basel, c/o Universitätsspital, 4031 Basel, Switzerland, [3]University Hospitals of Geneva, Cardiology Division, Department of Medicine, Rue Gabrielle-Perret-Gentil 4, 1211 Geneva, Switzerland, [4]University of Freiburg, Experimental Polymer Physics, Hermann Herder Strasse 3, 79104 Freiburg, Germany, [5]Biozentrum, University of Basel, Klingelbergstrasse 50/70, 4056 Basel, Switzerland. *e-mail: bert.mueller@unibas.ch; till.saxer@unige.ch; andreas.zumbuehl@unige.ch
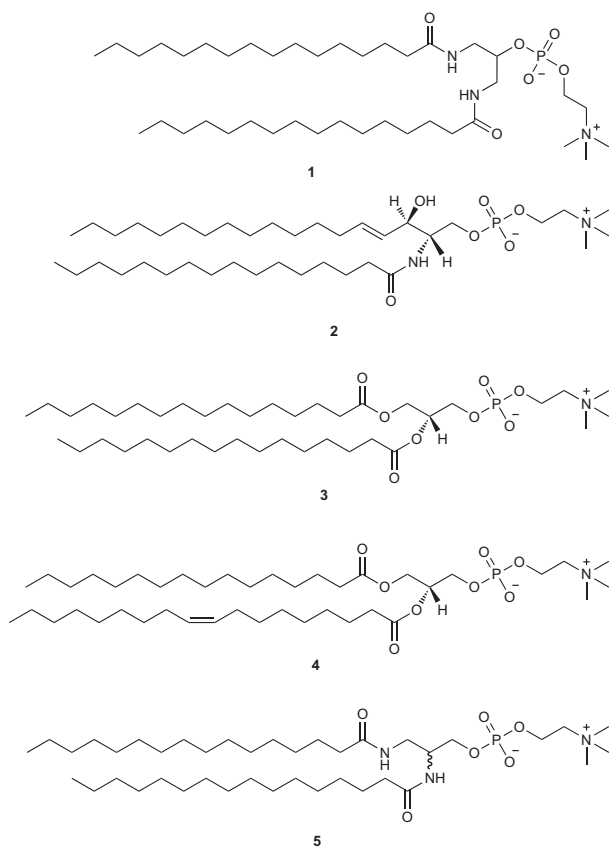
Figure 1 | Chemical structures of phospholipids. 1, Pad–PC–Pad, an artificial phospholipid containing two amide bonds at positions 1 and 3 of the original glycerol backbone. **2**, *N*-palmitoyl-D-*erythro*-sphingosylphosphorylcholine (16:0 SM), containing one amide bond. **3**, DPPC. **4**, 1-Palmitoyl-2-oleoyl-*sn*-glycero-3-phosphocholine (POPC), the dominant component of EggPC, contains no amide bonds, but ester bonds instead. **5**, Pad–Pad–PC, the asymmetric variant of **1**.

phospholipid with two C 14:0 amido chains in a 1,2-position did show reduced membrane fluidity at the polar interface[11]. The Pad–PC–Pad substitution at both the 1- and 3-positions should therefore yield amide groups with better steric alignment for directionally dependent hydrogen-bond formation in the polar hydrated region. This 1,3-configuration renders the lipid insensitive to metabolization by phospholipase A_2 (Supplementary Fig. S1).

Pad–PC–Pad was compared with *N*-palmitoyl-D-*erythro*-sphingosyl-phosphorylcholine (16:0 SM, **2**), a natural lipid containing one amide bond, and to dipalmitoylphosphatidylcholine (**3**), which contains no amides (Fig. 1). Differential scanning calorimetry (DSC) measurements of 100 nm unilamellar vesicles prepared by the extrusion method (LUVET$_{100}$) in buffer showed that Pad–PC–Pad has a phase transition temperature T_m of 35 °C ($\Delta H = 7{,}260$ cal mol^{-1}; $t_{1/2} = 3.2$ K; Supplementary Fig. S2), which is lower than the T_m of 16:0 SM (39.2 °C, $\Delta H = 7{,}586$ cal mol^{-1}; $t_{1/2} = 2.5$ K) and DPPC (40.9 °C, $\Delta H = 6{,}001$ cal mol^{-1}; $t_{1/2} = 1.9$ K)[15,16]. Analogously, earlier literature on Mad–Mad–PC ($T_m = 18$ °C) reported a comparable 5 K decrease in T_m compared to the natural dimyristoyl phosphatidylcholine ($T_m = 23$ °C)[11]. In contrast, reducing the *N*-acyl chain length by two carbons results in a much larger change in T_m (~13–25 K, ref. 17), suggesting that changes in the acyl chain length contribute more to the chain melting

temperature than a shift of the substitution pattern from 1,2 to 1,3 in the polar interface[18].

To visualize the morphology of the liposomes with fluorescence microscopy, we prepared giant unilamellar vesicles (GUVs) by the electroformation method[19,20]. The fluorescent lipid lissamine rhodamine DOPE (rho-DOPE) was used as fluorescent marker at 1 mol% of the total lipid content. The dye is expected to accumulate preferentially in the fluid membrane phase and will not penetrate into solid domains.

Several of the observed vesicles were faceted and differed distinctively from the spherical geometry of conventional vesicles. Figure 2a shows an example of a GUV resembling a higher-order polyhedron with a co-existence of liquid-ordered and fluid domains (Supplementary Fig. S2). The fluorescent probe rho-DOPE is not observed in areas of flat faceted liquid-ordered domains, but is sequestered into the curved fluid domains in the middle and edges of these facets. The addition of cholesterol (Fig. 2b) results in a more fluid membrane and spherical vesicles. Theory[2] predicts the accumulation of the dye in the fluid-phase region of high curvature. As the flat facets are connected by boundaries of higher curvature, one would also expect to find fluorescent dye molecules in this region, as confirmed by our experiments.

Cryo-transmission electron microscopy (TEM) was carried out for LUVET$_{100}$ as described previously[21]. A snapshot of the vesicle morphology shows that, in this size regime, lenticular rather than spherical or faceted vesicles are formed (Fig. 2c,d). These LUVET$_{100}$ were initially prepared above the T_m of Pad–PC–Pad. After cooling to 20 °C, they could relax to non-spherical shapes because of the propensity of Pad–PC–Pad to form flat membranes. The lenticular morphology is regarded as an intermediate state of minimized energy between a spherical vesicle and a flat surface[2].

Non-spherical vesicles demonstrate a lower encapsulated volume per surface area than a sphere with the same surface. It is therefore expected that lenticular vesicles will encapsulate less material per surface area than spherical vesicles. However, calculations showed the encapsulation efficiency of a representative Pad–PC–Pad lenticular vesicle selected from a cryo-TEM image was only 3% lower than a spherical vesicle of the same surface area (Supplementary Fig. S3). This was corroborated experimentally by measuring the total entrapped volume of carboxyfluorescein in vesicles formulated from a known total concentration of Pad–PC–Pad (Supplementary Section S5). We therefore conclude that the loss in encapsulation efficiency is negligible.
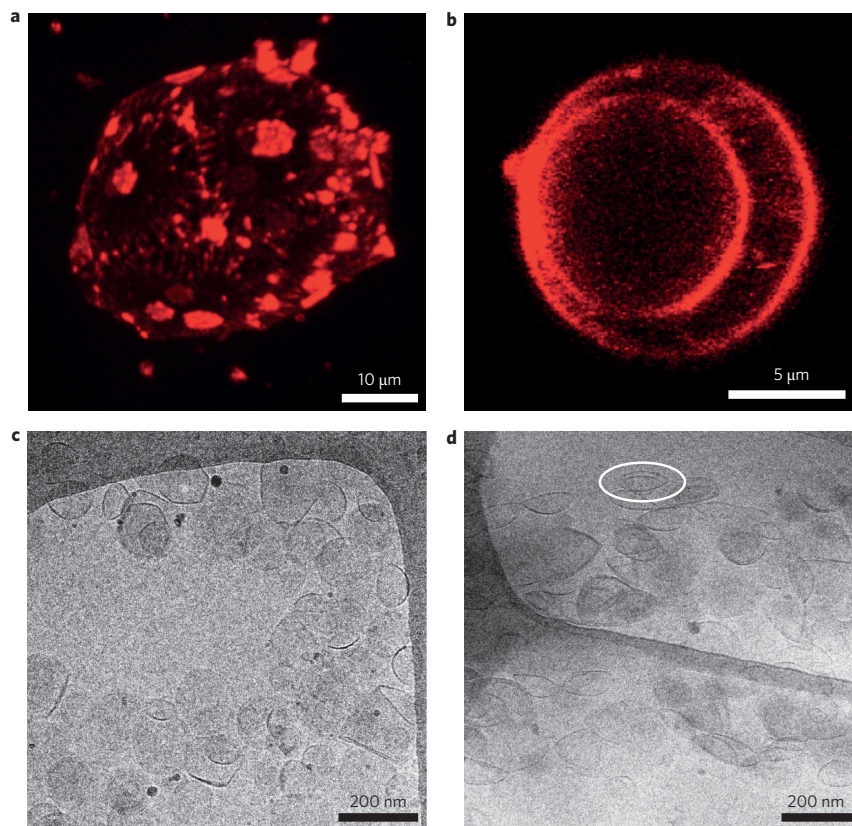
The equators of lenticular vesicles probably represent breaking points, suggesting that Pad–PC–Pad vesicles might exhibit special properties, that is, leaking under mechanical stress. First preliminary cytotoxicity and complement activation tests (Supplementary Fig. S4 and Table S1) revealed no negative effects from the non-spherical form factor, as were reported for doxorubicin-loaded liposomes[22].

Pad–PC–Pad vesicles are mechanosensitive
To test the mechanical properties of the corresponding nanocontainers, we prepared LUVET$_{100}$ (1–2 orders of magnitude smaller than GUVs) of artificial and natural phospholipids **1** to **5**. We hydrated a thin film of lipids and extruded the multilamellar vesicles through a 100-nm-pore filter membrane to produce uniform LUVET$_{100}$ (ref. 23). The liposomes contained 5(6)-carboxyfluorescein at a self-quenching concentration during encapsulation. When the dye is released from the liposome into the medium it dilutes, leading to fluorescence dequenching, and is therefore detectable using fluorescence spectroscopy[24].

Figure 3a shows the stability of vesicles that were left untouched on the laboratory bench for the indicated periods of time (Supplementary Fig. S5). At 25 °C, lipids **1** to **3**, which were in the gel state[25–27], released less than 12% of their cargo over one

2.3 Proof of principle: Mechano-sensitive nano-containers for targeted drug delivery to constricted vessels in the heart

45

ARTICLES

Figure 2 | Confocal micrographs of GUVs and cryo-TEM micrographs of LUVET₁₀₀s formulated from Pad–PC–Pad. a, GUVs made from 100% Pad–PC–Pad (doped with rho-DOPE) have various shapes, including this polyhedron (see Supplementary Movie). **b**, Adding 30 mol% cholesterol to the membrane is expected to induce a more fluid membrane state, which is corroborated by the spherical morphology of the GUVs and homogeneous distribution of rho-DOPE. Both measurements were made at 25 °C. **c**, Cryo-TEM of LUVET$_{100}$ formulated from Pad–PC–Pad, seen from the top and from an angle of 45°. **d**, The lenticular morphology of the 100 nm vesicles is clearly visible. An example of this lenticular shape, with two spherical segments joined by a discontinuity around the diameter, is highlighted. Also, straight edges contrast with the round morphology typically found in vesicles formulated from natural phospholipids such as EggPC.

week, typically at a rate of <1% per day. In contrast, lipid **4**, which was in the liquid state, did release cargo over time. It remains to be seen to what extent lipid chain interdigitation adds to the stability of the described bilayers. However, neither 16:0 SM (**2**) nor DPPC (**3**) shows interdigitation[28].

The vesicle formulations were then placed into a glass vial and shaken on a vortex at 2,500 r.p.m. at 25 °C for up to 60 s. Figure 3b shows that neither 16:0 SM (**2**) nor DPPC (**3**) vesicles release their carboxyfluorescein cargo. In contrast, Pad–PC–Pad (**1**) vesicles release their cargo to a significant extent. Together with the data in Fig. 3a, it is obvious that Pad–PC–Pad demonstrates a characteristic behaviour in which the vesicles are perfectly stable at rest but release their contents on shaking (leakage was induced even when agitating the vial in the experimenter's hand). We postulate that these vesicles respond to the applied shear forces with transient leakage, similar to the shear-induced release from L-α-phosphatidylcholine (EggPC) vesicles[29,30]. Furthermore, the alignment of amides in the 1,3-diamidophospholipid Pad–PC–Pad is of paramount importance. We synthesized the corresponding asymmetric 1,2-diamidophospholipid Pad–Pad–PC (**5**, Supplementary Sections S1.2–1.4), and vesicles formulated from this lipid demonstrated a significantly reduced shear sensitivity (Fig. 3b).

One can define three classes of vesicles with distinct release properties. First, natural vesicles in the liquid state (EggPC) show

spontaneous leakage that is accelerated by shear stress (Fig. 3a–c, **4**). Second, natural vesicles in the gel state (16:0 SM (**2**) and DPPC (**3**)) show no spontaneous release and are insensitive to mechanostimulation. Here, we present a third class of vesicles made from the artificial Pad–PC–Pad (**1**). In the gel state they show no spontaneous release, but they are mechanosensitive. In the liquid state, immediate total spontaneous release of vesicle cargo is observed (Fig. 3c). Both release patterns are beneficial for drug delivery.

Figure 3d shows that the shear-induced leakage from Pad–PC–Pad vesicles at room temperature is inversely proportional to the concentration of liposomes in suspension. We find that the vesicles do not fuse but instead aggregate within 5 s, especially above a vesicle concentration of 54 μM, reducing the probability of vesicle leakage (Supplementary Fig. S6). Under shear stress, these aggregates break down to their 100 nm vesicle components (Fig. 6c,d).

Biphasic nature of Pad–PC–Pad monolayers

Monolayer studies give a first approximation of the biophysical characteristics of a phospholipid. Pad–PC–Pad demonstrates a sharp inflection at the phase transition from the gaseous analogue to the liquid expanded phase (Fig. 4a), similar to the reported pressure–area isotherms of N-myristoylethanolamine, where the importance of hydrogen bonding has been emphasized[31]. This

ARTICLES
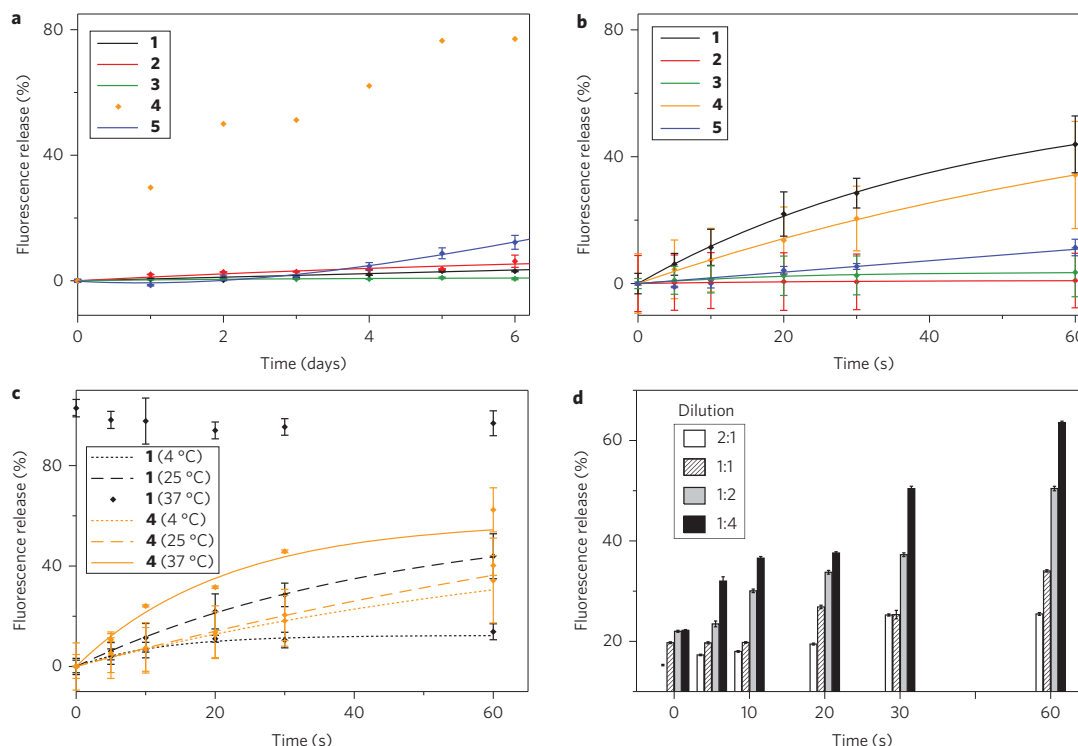
Figure 3 | Release of carboxyfluorescein from vesicles made of phospholipids 1 to 5. a, Spontaneous release of vesicle cargo on prolonged storage at 25 °C. **b**, Release of vesicle cargo on shaking the vial on a vortex shaker at 25 °C. It is apparent that vesicles prepared from EggPC (**4**) release their cargo in either situation, whereas Pad–PC–Pad (**1**) vesicles only release cargo when shaken. **c**, Effect of temperature on vesicle cargo release on shaking on a vortex shaker. **d**, Effect of Pad–PC–Pad vesicle suspension dilution (stock phosphoplipid concentration, 54 μM) on vesicle cargo release on shaking on a vortex shaker at room temperature. Release increases with time and dilution. Error bars are standard deviations of triplicates.
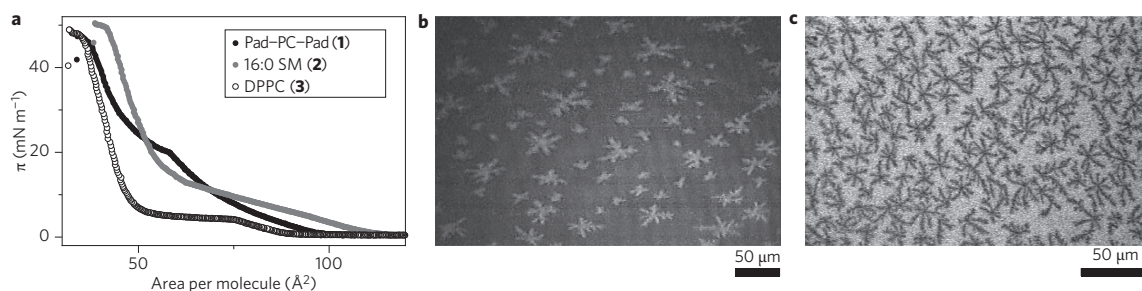
Figure 4 | Monolayer studies of Pad–PC–Pad. a, Pressure–area isotherms for the lipids studied at 20 °C. A clear inflection point is visible for Pad–PC–Pad but not for the other lipids. **b,c**, Micrographs showing the ramified morphology of crystallized Pad–PC–Pad islands in a liquid Pad–PC–Pad matrix. The presence of crystallized regions is clearly visible at >20 mN m^{-1} and 20 °C. The formation of crystals in the fluid phase shows the coexistence of a biphasic system. Snapshot (**b**) of a Brewster-angle micrograph at 23 mN m^{-1}. Crystallites merge and form more complex forms within minutes[40,41]. Fluorescent microscopy (**c**) of a Pad–PC–Pad monolayer (doped with 1 mol% of the fluorescent probe 1-palmitoyl-2-{6-[(7-nitro-2-1,3-benzoxadiazol-4-yl)amino]hexanoyl}-*sn*-glycero-3-phosphocholine) at 23 mN m^{-1} and 20 °C.

phase transition is followed by a plateau region, characteristic of a liquid expanded/liquid condensed two-phase coexistence[32] and the onset of two-dimensional crystallization[33]. The minimal area per molecule was approximated by extrapolating the pressure–area isotherm at its highest slope to zero surface pressure[34]. This resulted in a value of ~49 Å^2 for DPPC, ~56 Å^2 for Pad–PC–Pad and ~59 Å^2 for 16:0 SM (Supplementary Fig. S7), in agreement with literature values[35–37].

Brewster-angle microscopy confirmed the coexistence of solid crystallization domains present in the liquid phase (Fig. 4b) of single-component Pad–PC–Pad monolayers. The microstructures

observed resemble the fractal or dendritic domains formed by pure sphingomyelin[37]. However, the reported domains for sphingomyelin stop growing at 12 mN m^{-1} and 40–50 μm, at equilibrium between the forces of line tension and long-range dipole–dipole repulsion[38]. In the present experiments, domains of Pad–PC–Pad keep growing and fusing, similar to DMPE domains[39–41]. This evidence for coexisting domains was corroborated by monolayer fluorescent microscopy experiments using 1 mol% of a fluorescent phospholipid (Fig. 4c).

The fact that Pad–PC–Pad crystallizes at higher surface pressure and below T_m hints at a heightened bending modulus at room

2.3 Proof of principle: Mechano-sensitive nano-containers for targeted drug delivery to constricted vessels in the heart

47

temperature leading to faceted vesicles. The GUV experiments (Fig. 2) essentially corroborate this explanation of the predicted non-spherical morphologies[2].

Shear force-based drug delivery

We went on to test whether lenticular vesicles might have potential in shear-induced drug delivery to constricted arteries for the treatment of atherosclerosis, a generalized inflammatory process of the artery wall[42]. Lipid deposition on the artery wall begins at the age of 25 years in humans, with the blood vessels slowly becoming increasingly narrow until, finally, some plaques can occupy up to ~90% of the lumen[43], with myocardial infarction occurring with stenoses well above 70% (ref. 44). Such a vessel narrowing fundamentally changes the blood flow pattern: healthy coronary arteries show average shear stresses of ~1.5 Pa, and this value rises to 7–10 Pa, or even well above 10 Pa, in constricted vessels[45].

So far, there has been no report of shear stress-induced drug delivery. However, fundamental rheological studies have shown that shearing of EggPC vesicles is concomitant with an increased efflux of entrapped Ca^{2+} compared with the slower release of entrapped ions from non-sheared vesicles[29,30,46]. Similarly, the release of a fluorescent dye is also increased by shearing of small and large unilamellar vesicles made from EggPC and Brij 76 (deca-ethylene glycol octadecyl ether, known as Brij S10)[29].

To assess the feasibility of drug release from a vesicle through shearing, carboxyfluorescein-loaded vesicles of varying formulations were subjected to *in vitro* shear conditions in haemodynamic flow conditions (Fig. 5a). To simulate physiological conditions, a model cardiovascular system was used that consisted of healthy and constricted lumens formed from poly(methyl methacrylate) (Fig. 5b). Both artery models were formed from tubes with an inlet diameter of 2.5 mm, one of which was provided with constrictions of up to 75% cross-sectional area along a 2.5 cm segment. The shear stress in each arterial model was estimated from two-dimensional images, and was found to be ~40 Pa in the constricted model and 2 Pa in the healthy model. These values are within reported physiological ranges (Supplementary Fig. S8).

An extracorporeal circulation pump was used to simulate the heart. This pump is a validated medical device for use in coronary bypass and aortic valve replacement surgery and was chosen because of its reputed low intrinsic shear stress[47,48]. Flexible tubes with an inner diameter of 10 mm connected the pressure gauge, flow reader and temperature bath. The pressure and flow rate in the entire *in vitro* system were controlled by regulating the pump speed. Pressures, flow rates, osmolarity and temperature were strictly maintained within physiological ranges (details below). The model was kept intentionally simple to investigate the contributing effects of the endogenous shear stresses in healthy and constricted models, providing a proof-of-concept for the hypothesis.

The vesicle suspension was first diluted to a lipid concentration of 15 µM in external buffer. Both the buffer and carboxyfluorescein media were adjusted to pH 7.4 to avoid pH-gradient-induced carboxyfluorescein leakage[49]. The diluted suspension was then loaded into the *in vitro* pump set-up with either the healthy or the
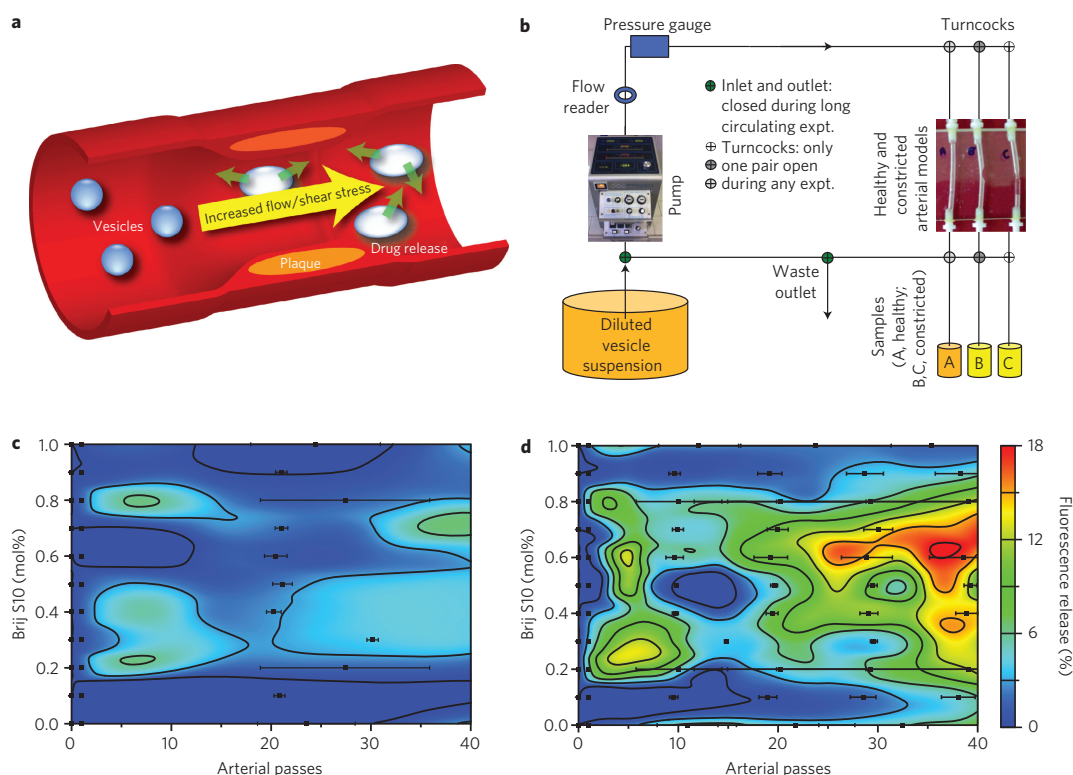
Figure 5 | Release of entrapped fluorescent dye after passage through an extracorporeal pump flow set-up. a, Schematic of the hypothesis using changes in endogenous shear stresses as a physical trigger for drug delivery. **b**, Experimental set-up. An extracorporeal heart pump is connected to a plastic model of healthy or constricted arteries. The system is closed once the product is loaded and the vesicles are allowed to circulate in the system for 20 min. **c,d**, Fluorescence release patterns of EggPC vesicles with 0–1 mol% Brij S10 at 37 °C. Release in the healthy arterial model (**c**) and release in the constricted artery model (**d**). Brij S10 concentration is plotted against number of passes through the arterial model, with fluorescence release along the z-axis. Background fluorescence release is subtracted for each set. The results therefore represent the fractional additional release after circulation in the arterial model.

ARTICLES
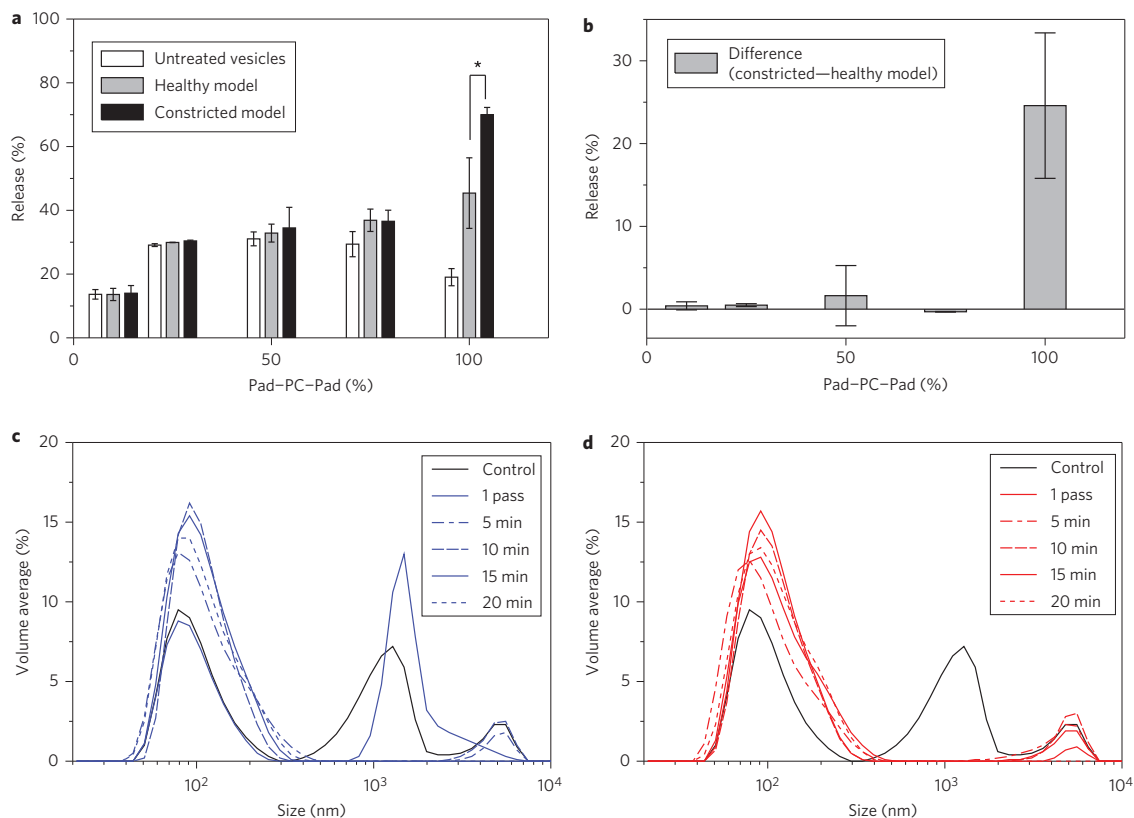
Figure 6 | Fluorescence release patterns of EggPC vesicles with 10–100 mol% Pad–PC–Pad at 37 °C. a, Fluorescence release before (Untreated) and after one pass only through either the healthy or constricted arterial models. **b**, Difference in fluorescence release for healthy and constricted models. **c,d**, DLS analysis of particle size of Pad–PC–Pad vesicles after one pass and 5, 10, 15 and 20 min circulation through the healthy (**c**) and constricted (**d**) artery models. At low or limited shear stresses (control measurement, healthy model after one pass), aggregation of vesicles is observed. TEM analysis (Supplementary Fig. S6) shows that aggregation of vesicles is a probable explanation for these observations. After prolonged circulation, aggregates are broken down into their 100 nm vesicle components, illustrated by an increase in the peak height at 100 nm and decrease in aggregate peaks at 1.1 and 1.5 μm.

constricted poly(methyl methacrylate) artery model connected. During the experiments, flow rates of ∼700 ml min^{-1} (healthy) or 350 ml min^{-1} (constricted artery model) were used, the pressure was 60 mmHg and the buffer temperature was 37 °C for long-circulating and 34 °C for single-pass experiments (Supplementary Fig. S9). Osmolarity was constant at 308 mOsm. Fluorescence release from vesicles was analysed by a fluorescence 96-well-plate reader. The error corresponds to the standard deviation of the triplicates.

To assess shear-induced release after a single pass through the pump, the vesicle suspension was pumped through the model artery and collected directly after the first pass (Fig. 5b). To assess release as a function of number of circulations, a closed loop was built. Aliquots of the circulating vesicle suspension were collected after 5, 10, 15 and 20 min. Flow was stopped for aliquot extraction using a syringe by closing the tap in the loop. With each aliquot extraction, an equivalent amount of buffer was injected.

Vesicle formulations reported in previous rheology studies were adapted and optimized[28]. The surfactant Brij S10 was admixed to EggPC at low concentrations (Fig. 5c,d). The optimized Brij S10 concentration led to high differences in the fluorescence release in the healthy and constricted lumens. This occurred at a concentration of 0.6 mol%, with $17 \pm 1\%$ of the entrapped dye being released after 40 passes through the constricted model but only $3.0 \pm 0.8\%$ release after passing through the healthy artery

(Supplementary Fig. S10). At Brij S10 concentrations of 0 and 1% there was no appreciable difference in the release in the constricted and healthy arteries, so the shear stress-induced release is unspecific.

Compared with the EggPC/Brij S10 vesicles, vesicles consisting entirely of Pad–PC–Pad demonstrated an even clearer distinction between release in the healthy and constricted vessel models. A low level of leakage occurred before treatment ($19.0 \pm 2.7\%$; release resulting from the formulation procedure and handling), but, after only one pass, a total leakage of $45.5 \pm 11.0\%$ was observed in the healthy artery model and $70.0 \pm 2.3\%$ in the constricted model (Fig. 6a,b).

Pad–PC–Pad was then admixed with EggPC to mitigate the release effect. Up to concentrations of 75% Pad–PC–Pad, the background fluorescence increased, but there is no statistically significant increase in release after one pass in either the healthy or constricted model (Fig. 6a, Supplementary Fig. S11). Therefore, one has to conclude that these formulations become unstable, or leaky, with an increase in Pad–PC–Pad concentration, but do not significantly increase their susceptibility to shear-induced release. The pure Pad–PC–Pad vesicles, however, are susceptible to shear-induced release, and show an appreciable preference for release in the high-shear-stress constricted-artery model (Fig. 6b). In contrast, in all formulations containing EggPC, shear-induced release was always <10% after one pass, and increases with concentration of Pad–PC–Pad.

Steinberg and co-workers[50] reported that isolated vesicles tank-tread and tumble in shear flow, but do not form pores. However, we postulate that the investigated Pad–PC–Pad vesicles may exhibit different behaviour under shear stress, given their smaller size and the secondary effects of vesicle collisions. Dynamic light scattering (DLS) investigation of Pad–PC–Pad vesicles established whether the vesicles were destroyed or simply deformed during release of their payload. Samples were measured after one pass and continuous circulation through the healthy- and constricted-artery models (Fig. 6c,d). Freshly prepared vesicles (not shown) showed no aggregates in the range 1–10 μm; however, even in the control measurement (constituting vesicles left on the bench for the duration of the experiment), vesicle aggregation was observed (Fig. 6c,d). After exposure to low shear environments—for example, one pass through the healthy artery (Fig. 6c)—the peak at 1 μm increased, indicating vesicle aggregation or fusion according to literature precedence[29]. However, after being subject to higher shear stresses (Fig. 6d) or repeated circulation (Fig. 6c; 10–20 min), these aggregates were broken into LUVET$_{100}$. The area under each curve remained constant, suggesting there was no significant loss in overall vesicle concentration. Furthermore, TEM showed that Pad–PC–Pad nanocontainers are prone to aggregation and not fusion (Supplementary Fig. S6). Aggregation and separation is therefore a likely explanation for the changes in mean size measured. These findings show that the release mechanism is most probably due to shear-induced transient pore formation at high shear rates, and not shear-induced destruction of the vesicles.

Conclusions

In conclusion, we have shown that the specially designed lenticular Pad–PC–Pad phospholipid vesicles could shift current paradigms of drug release from biochemical to endogenous mechanical triggers. The lenticular shape of the liposomes leads to preferential breaking points along the equator that make them sensitive to increased shear stresses. Furthermore, we have shown, using a model cardiovascular system, that the Pad–PC–Pad vesicles preferentially release drugs in areas of high shear stress such as those that mimic constricted blood vessels in heart attack patients. If successfully applied, this could eliminate the side effects arising from systemic injection of drugs. The release of a fluorophore from Pad–PC–Pad vesicles is an order of magnitude higher than that of its natural counterparts, such as EggPC. This observation might lead to significant innovations in targeted drug delivery using purely physical triggers.

Methods

Synthesis of Pad–PC–Pad (1). Pad–PE–Pad (non-methylated phosphoethanolamine, 1 g, 1.45 mmol) was dissolved in 100 ml of methanol. Dimethyl sulphate (1 ml, 1.33 g, 10.5 mmol) was added and the mixture was warmed to 40 °C, then a solution of 1.45 g (10.5 mmol) potassium carbonate in 20 ml water was added over 1 min. The mixture was vigorously stirred for 30 min then cooled to 20 °C. The solvent was removed under reduced pressure. The solid was then purified on a silica gel column (75% CH$_2$Cl$_2$, 22% MeOH, 3% aq. NH$_4$OH (25%)), yielding 0.56 g of the product (0.81 mmol, 53%) (Supplementary Section S1.1).

Production of vesicles and loading with active compounds. All compounds were purchased from Sigma-Aldrich or Avanti Polar Lipids and used without further purification unless otherwise stated. Liposome formulation was based on the techniques described by Olson *et al.*[23].

LUVET$_{100}$ were prepared as follows. Lipid (30 μmol; for example, egg yolk phosphatidylcholine (EggPC, Avanti Polar Lipids), Pad–PC–Pad (1) or a combination of lipids) was weighed into a 25 ml round-bottomed flask and dissolved in 1 ml chloroform. Any required additive was added at this point. After evaporation to dryness, the film was dried for 12 h under high vacuum. Internal buffer (1 ml, 50 mM 5(6)-carboxyfluorescein, 10 mM HEPES buffer (AppliChem), 10 mM NaCl dissolved in pure water, pH 7.4 (NaOH)) was added to the flask to hydrate the film for 30 min. The suspension was sequentially frozen (liquid nitrogen bath) and melted (water bath, 40–65 °C, depending on constituent lipid T_m) five times, then extruded 11 times using a mini-extruder (Avanti Polar Lipids) and a track-etched filter (100 nm, Whatman). Purification by size exclusion chromatography (1.5 × 20 cm Sephadex G-50 column) in external buffer (107 mM NaCl, 10 mM HEPES dissolved in ultrapure water, pH 7.4 (NaOH)) afforded the pure 5(6)-carboxyfluorescein-loaded vesicles. Vesicles were stored at 5 °C in the dark until use. All experiments were conducted within 24 h of vesicle formulation.

GUVs were preared as follows. Pad–PC–Pad (1, 0.5 mg) was dissolved in 1 ml CHCl$_3$. To this, 10 μl of Liss-Rho-DPPE solution (0.25 mg of lipid in 1 ml CHCl$_3$) was added. ITO-coated glass plates were washed with water and EtOH, then CHCl$_3$. A volume of 20 μl of the lipid solution was deposited on the conductive face of the plate. CHCl$_3$ was evaporated in the oven (room temperature) for 1 h at reduced pressure. A second ITO slide was put on top of the first using Vitrex as sealant. The void was filled with iso-osmolar sucrose solution (224 mOs). Vesicles were then grown for 2 h at 55 °C at 1 V and 10 Hz.

An 'observation chamber' was made from two glass microscopy slides that were washed with water and EtOH. A square of parafilm was laid out between the two plates and melted at 100 °C. The chamber was washed with casein solution (2 mg ml^{-1}) and left to dry for 15 min. The solution was then replaced with HEPES buffer of the same osmolarity (200 mOs) as the sucrose solution. A volume of 10 μl of lipid solution was added and the chamber was sealed with varnish.

Spontaneous release and vortex release. LUVET$_{100}$ were prepared using 2 mg Pad–PC–Pad (1), DPPC (AvantiLipids) or *N*-palmitoyl sphingomyelin (AvantiLipids) in 0.5 ml of carboxyfluorescein buffer (10 mM HEPES, NaOH pH 7.4, 10 mM NaCl, 50 mM carboxyfluorescein). The extrusion procedure and size exclusion chromatography purification are described above. The purified liposomal suspension was diluted to 100 ml with a second buffer (10 mM HEPES, NaOH pH 7.4, 10 mM NaCl). Five 3 ml aliquots were filled into 20 ml vials with polystyrene caps and vortexed for a discrete amount of time (0, 5, 10, 20 and 60 s) at 2,500 r.p.m. Release of contents was measured by a plate reader at wavelengths of 492 nm (excitation) and 517 nm (emission).

Spontaneous release was measured daily over 6 days for each sample. As a control for maximum dye release, a second sample of the liposomal suspension was mixed with a small volume of detergent (Triton-X100).

Influence of vesicle concentration on the release by vortex. LUVET$_{100}$ were formulated using the procedure described above (2 mg of Pad–PC–Pad (1) in 0.5 ml of carboxyfluorescein buffer (10 mM HEPES, NaOH pH 7.4, 10 mM NaCl, 50 mM carboxyfluorescein)). The purified suspension was diluted to 50 ml with a second buffer (10 mM HEPES, NaOH pH 7.4, 10 mM NaCl). The suspension was then diluted (2:1, 1:1, 1:0.5, 1:0.25). Five 3 ml aliquots were filled into 20 ml vials with polystyrene caps and vortexed for a discrete amount of time (0, 5, 10, 20 and 60 s) at 2,500 r.p.m. Release of the content was measured by a plate reader at wavelengths of 492 nm (excitation) and 517 nm (emission).

References

1. Torchilin, V. P. Recent advances with liposomes as pharmaceutical carriers. *Nature Rev. Drug Discov.* **4**, 145–160 (2005).
2. Noguchi, H. Polyhedral vesicles: a Brownian dynamics simulation. *Phys. Rev. E* **67**, 041901 (2003).
3. Blaurock, A. E. & Gamble, R. C. Small phosphatidylcholine vesicles appear to be faceted below the thermal phase transition. *J. Membr. Biol.* **50**, 187–204 (1979).
4. Phillips, M. C. & Chapman, D. Monolayer characteristics of saturated 1,2-diacyl phosphatidylcholines (lecithins) and phosphatidylethanolamines at the air–water interface. *Biochim. Biophys. Acta* **163**, 301–313 (1968).
5. Lichtenberg, D. *et al.* Effect of surface curvature on stability, thermodynamic behavior, and osmotic activity of dipalmitoylphosphatidylcholine single lamellar vesicles. *Biochemistry* **20**, 3462–3467 (1981).
6. Lichtenberg, D. & Schmidt, C. F. Molecular packing and stability in the gel phase of curved phosphatidylcholine vesicles. *Lipids* **16**, 555–557 (1981).
7. Dubois, M. *et al.* Self-assembly of regular hollow icosahedra in salt-free catanionic solutions. *Nature* **411**, 672–675 (2001).
8. Dubois, M. *et al.* Shape control through molecular segregation in giant surfactant aggregates. *Proc. Natl Acad. Sci. USA* **101**, 15082–15082 (2004).
9. De Haas, G. H., Dijkman, R., van Oort, M. G. & Verger, R. Competitive inhibition of lipolytic enzymes. III. Some acylamino analogues of phospholipids are potent competitive inhibitors of porcine pancreatic phospholipase A2. *Biochim. Biophys. Acta* **1043**, 75–82 (1990).
10. Jia, C. & Haines, A. H. Diamide analogues of phosphatidyl choline as potential anti-aids agents. *J. Chem. Soc. Perkin Trans.* **1**, 2521–2523 (1993).
11. Sunamoto, J., Goto, M., Iwamoto, K., Kondo, H. & Sato, T. Synthesis and characterization of 1,2-dimyristoylamido-1,2-deoxyphosphatidylcholine as an artificial boundary lipid. *Biochim. Biophys. Acta* **1024**, 209–219 (1990).
12. Gupta, C. M. & Bali, A. Carbamyl analogs of phosphatidylcholines: synthesis, interaction with phospholipases and permeability behavior of their liposomes. *Biochim. Biophys. Acta* **663**, 506–515 (1981).
13. Fedotenko, I. A., Zaffalon, P.-L., Favarger, F. & Zumbuehl, A. The synthesis of 1,3-diamidophospholipids. *Tetrahedron Lett.* **51**, 5382–5384 (2010).

ARTICLES

14. Liu, H. *et al.* DNA-based micelles: synthesis, micellar properties and size-dependent cell permeability. *Chem. Eur. J.* **16,** 3791–3797 (2010).

15. Heimburg, T. Mechanical aspects of membrane thermodynamics. Estimation of the mechanical properties of lipid membranes close to the chain melting transition from calorimetry. *Biochim. Biophys. Acta* **1415,** 147–162 (1998).

16. Maulik, P. R. & Shipley, G. G. *N*-palmitoyl sphingomyelin bilayers: structure and interactions with cholesterol and dipalmitoylphosphatidylcholine. *Biochemistry* **35,** 8025–8034 (1996).

17. Vance, D. E. *Biochemistry of Lipids, Lipoproteins and Membranes* (Elsevier Science, 1991).

18. Seelig, J., Dijkman, R. & De Haas, G. H. Thermodynamic and conformational studies on *sn*-2-phosphatidylcholines in monolayers and bilayers. *Biochemistry* **19,** 2215–2219 (1980).

19. Holopainen, M. J., Angelova, M. & Kinnunen, P. K. J. Giant liposomes in studies on membrane domain formation. *Methods Enzymol.* **367,** 15–23 (2003).

20. Walde, P., Cosentino, K., Engel, H. & Stano, P. Giant vesicles: preparations and applications. *ChemBioChem* **11,** 848–865 (2010).

21. Ishikawa, T., Sakakibara, H. & Oiwa, K. The architecture of outer dynein arms *in situ*. *J. Mol. Biol.* **368,** 1249–1258 (2007).

22. Szebeni, J. *et al.* Liposome-induced complement activation and related cardiopulmonary distress in pigs: factors promoting reactogenicity of Doxil and AmBisome. *Nanomedicine* **8,** 176–184 (2012).

23. Olson, F., Hunt, C. A., Szoka, F. C., Vail, W. J. & Papahadjopoulos, D. Preparation of liposomes of defined size distribution by extrusion through polycarbonate membranes. *Biochim. Biophys. Acta* **557,** 9–23 (1979).

24. Weinstein, J., Yoshikami, S., Henkart, P., Blumenthal, R. & Hagins, W. Liposome–cell interaction: transfer and intracellular release of a trapped fluorescent marker. *Science* **195,** 489–492 (1977).

25. Blok, M. C., van Deenen, L. L. M. & de Gier, J. Effect of the gel to liquid crystalline phase transition on the osmotic behaviour of phosphatidycholine liposomes. *Biochim. Biophys. Acta* **433,** 1–12 (1976).

26. Inoue, K. Permeability properties of liposomes prepared from dipalmitoyllecithin, dimyristoyllecithin, egg lecithin, rat liver lecithin and beef brain sphingomyelin. *Biochim. Biophys. Acta* **339,** 390–402 (1974).

27. Magin, R. L. & Niesman, M. R. Temperature-dependent permeability of large unilamellar liposomes. *Chem. Phys. Lipids* **34,** 245–256 (1984).

28. Barenholz, Y & Thompson, T. E. Sphingomyelins in bilayers and biological membranes. *Biochim. Biophys. Acta* **604,** 129–158 (1980).

29. Bernard, A. L. *et al.* Shear-induced permeation and fusion of lipid vesicles. *J. Colloid Interface Sci.* **287,** 298–306 (2005).

30. Chakravarthy, S. R. & Giorgio, T. D. Shear stress-facilitated calcium ion transport across lipid bilayers. *Biochim. Biophys. Acta* **1112,** 197–204 (1992).

31. Brezesinski, G., Dobner, B., Stefaniu, C. & Vollhardt, D. Monolayer characteristics of an *N*-acylated ethanolamine at the air/water interface. *J. Phys. Chem. C* **115,** 8206–8213 (2011).

32. Fainerman, V. B., Vollhardt, D. & Melzer, V. Kinetics of two-dimensional phase transition of amphiphilic monolayers at the air/water interface. *J. Chem. Phys.* **107,** 243–251 (1997).

33. Phillips, M. C., Graham, D. E. & Hauser, H. Lateral compressibility and penetration into phospholipid monolayers and bilayer membranes. *Nature* **254,** 154–156 (1975).

34. Gaines, G. L. *Insoluble Monolayers at Liquid–Gas Interfaces* (Wiley, 1966).

35. Duncan, S. L. & Larson, R. G. Comparing experimental and simulated pressure-area isotherms for DPPC. *Biophys. J.* **94,** 2965–2986 (2008).

36. Lund-Katz, S., Laboda, H. M., McLean, L. R. & Phillips, M. C. Influence of molecular packing and phospholipid type on rates of cholesterol exchange. *Biochemistry* **27,** 3416–3423 (1988).

37. Prenner, E., Honsek, G., Hönig, D., Möbius, D. & Lohner, K. Imaging of the domain organization in sphingomyelin and phosphatidylcholine monolayers. *Chem. Phys. Lipids* **145,** 106–118 (2007).

38. McConnell, H. M. & De Koker, R. Equilibrium thermodynamics of lipid monolayer domains. *Langmuir* **12,** 4897–4904 (1996).

39. Hoenig, D. & Moebius, D. Direct visualization of monolayers at the air–water interface by Brewster angle microscopy. *J. Phys. Chem.* **95,** 4590–4592 (1991).

40. Müller, B. Natural formation of nanostructures: from fundamentals in metal heteroepitaxy to applications in optics and biomaterials science. *Surf. Rev. Lett.* **8,** 169–228 (2001).

41. Müller, B. *et al.* Island shape transition in heteroepitaxial metal growth on square lattices. *Phys. Rev. Lett.* **80,** 2642–2645 (1998).

42. Berridge, B. R. *et al.* A translational approach to detecting drug-induced cardiac injury with cardiac troponins: consensus and recommendations from the Cardiac Troponins Biomarker Working Group of the Health and Environmental Sciences Institute. *Am. Heart J.* **158,** 21–29 (2009).

43. Slysh, S., Goldberg, S., Dervan, J. P. & Zalewski, A. Unstable angina and evolving myocardial infarction following coronary bypass surgery: pathogenesis and treatment with interventional catheterization. *Am. Heart J.* **109,** 744–752 (1985).

44. Pijls, N. H. J. Acute myocardial infarction and underlying stenosis severity. *Am. J. Cardiol.* **103,** 1204–1205 (2009).

45. Cheng, C. *et al.* Large variations in absolute wall shear stress levels within one species and between species. *Atherosclerosis* **195,** 225–235 (2007).

46. Giorgio, T. D. & Yek, S. H. The effect of bilayer composition on calcium ion transport facilitated by fluid shear stress. *Biochim. Biophys. Acta* **1239,** 39–44 (1995).

47. Curtis, J. J. *et al.* Centrifugal pumps: description of devices and surgical techniques. *Ann. Thorac. Surg.* **68,** 666–671 (1999).

48. Paparella, D. *et al.* Blood damage related to cardiopulmonary bypass: *in vivo* and *in vitro* comparison of two different centrifugal pumps. *ASAIO J.* **50,** 473–478 (2004).

49. Clerc, S. & Barenholz, Y. Loading of amphipathic weak acids into liposomes in response to transmembrane calcium acetate gradients. *Biochim. Biophys. Acta* **1240,** 257–265 (1995).

50. Kantsler, V. & Steinberg, V. Transition to tumbling and two regimes of tumbling motion of a vesicle in shear flow. *Phys. Rev. Lett.* **96,** 036001 (2006).

Acknowledgements

Author contributions

B.M., T.S. and A.Z. contributed the original idea, secured the financing and supervised the project. M.N.H., B.M., T.S. and A.Z. designed the experiments. I.A.F. synthesized Pad–PC–Pad. M.N.H., I.A.F., D.A., J.A., L.B., F.F., R.R., R.T., P-L.Z., A.Zi. and A.Z. performed the experiments. M.N.H., R.R., A.Zi., B.M., T.S. and A.Z. wrote the paper.

Additional information

Shear-stress Sensitive Lenticular Vesicles for Targeted Drug Delivery

Margaret N. Holme, Illya A. Fedotenko, Daniel Abegg, Jasmin Althaus, Lucille Babel, France Favarger, Renate Reiter, Radu Tanasescu, Pierre-Léonard Zaffalon, André Ziegler, Bert Müller, Till Saxer, Andreas Zumbuehl

1. Synthesis of phospholipids and their characterisation

Starting compounds and solvents were purchased from Sigma-Aldrich/Fluka or Acros and were used without further purification. The precursor Pad-PE-Pad and its homologues were synthesised using the procedures from Fedotenko et al.[1].

Column chromatographic separation was carried out using 230-400 mesh silica gel. TLC plates were developed either with potassium permanganate mixture (1 g of $KMnO_4$, 2 g of Na_2CO_3, 100 mL of H_2O) or ethanolic solution of phosphomolybdic acid. ^{1}H, ^{13}C and ^{31}P NMR spectra were recorded (as indicated) on either a Bruker 300 MHz or 400 MHz spectrometer and are reported as chemical shifts (δ) in ppm relative to TMS ($\delta = 0$). Spin multiplicities are reported as a singlet (s) or triplet (t) with coupling constants (J) given in Hz, or multiplet (m). Electron-spray ionisation mass spectroscopy (ESI-MS) for the characterisation of compounds was performed on a ESI API 150EX and are reported as mass-per-charge ratio. IR spectra were recorded on a Perkin Elmer Spectrum One FT-IR spectrometer (ATR, Golden Gate). The melting points are uncorrected. For the experiments with vortex we used an IKA Vortex Genius 3.

Monolayers were measured on a Langmuir Film Balance (Riegler & Kierstein, Germany). Pressure-area isotherms were calculated using the following equation[2]:

$$\kappa_T = (-1/A)(\partial A/\partial \pi)_T$$

Where κ_T is the 2D isothermal lateral compressibility; A is the surface area per molecule and π is the surface pressure.

BAM was recorded on a Multiskop (Optrel). The fluorescent microscope was made by Riegler & Kierstein, Germany. DSC thermograms were recorded on a Microcal VP-DSC (Microcal, Northampton, UK). The artificial blood-vessel model was made by Elastrat Sàrl, Switzerland. The extracorporeal circulation pump was a gift from Medtronic Bio-Pump, Bio Console 540, Medtronic, Switzerland.

Cryo-TEM was carried out for $LUVET_{100}$ using a Tecnai F20 TEM (FEI, USA) at the Electron Microscopy Center, ETH Zurich.

1.1 Characterisation of 1,3-dipalmitamidopropan-2-yl 2-(trimethylammonio)ethyl phosphate (Pad-PC-Pad, 1)

Rf= 0.32 (75% CH_2Cl_2, 22% MeOH, 3% aq. NH_4OH (25%)).

^{1}H NMR (400 MHz, $CDCl_3$) δ 7.58 (s, 2H), 4.39 (s, 2H), 4.12 (s, 1H), 3.89 (s, 2H), 3.48 (s, 2H), 3.36 (s, 9H), 3.25 – 3.02 (m, 2H), 2.18 (t, J = 7.3 Hz, 4H), 1.56 (s, 4H), 1.24 (s, 48H), 0.87 (t, J = 6.7 Hz, 6H).

^{13}C NMR (101 MHz, $CDCl_3$) δ 174.7 (C=O), 72.2 (CH), 66.7, 59.6, 54.7(CH3s at the headgroup), 41.0, 36.9, 32.1, 29.89, 29.84, 29.72, 29.70, 29.59, 26.2, 22.9, 14.3 (CH3s of the tails).

^{31}P NMR (121 MHz, $CDCl_3$) δ 2.97.

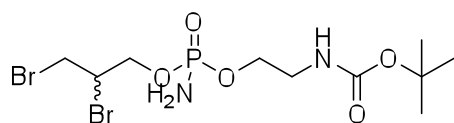**LRMS (ESI+)**m/z calcd for $C_{40}H_{83}N_3O_6P$ [M+H]$^+$ 732.6, found 732.7.

FTIR (cm^{-1}): 3285, 2917, 2850, 1651, 1545, 1468, 1239, 1088, 1058, 967, 720.

mp 203°C.

Zeta Potential HEPES buffer: -5.46 mV ± 0.4281 mV Pad-PC-Pad (**1**): -4.04 mV ± 0.334 mV

1.2 (rac) *tert*-Butyl (2-((amino((1,2-dibromooropropan-3-yl)oxy)phosphoryl)oxy)ethyl)-carbamate (6)

0.514 mL (1.09 g, 5 mmol) of *rac*-1,2-dibromopropanol were added to 0.458 mL POCl$_3$ (0.770 g, 5 mmol) and 1.39 mL NEt$_3$ (1.01 g, 10 mmol) in 50 mL of dry CH$_2$Cl$_2$ and the resulting solution was stirred for 2 h. To this was added 0.810 g (5 mmol) of Boc-protected ethanolamine.[1] The mixture was stirred for 4 h, after that solvent was removed under reduced pressure, and the product was purified over a silica gel column (2% MeOH-CH$_2$Cl$_2$) to give **6** as a white solid (0.52 g, 1.22 mmol, 24%).

Rf=0.5 (EtOAc)

^{1}H NMR (500 MHz, CDCl$_3$) δ 5.30 – 5.04 (m, 1H), 4.48 – 4.35 (m, 2H), 4.35 – 4.24 (m, 1H), 4.23 – 3.98 (m, 2H), 3.87 – 3.71 (m, 2H), 3.53 – 3.21 (m, 4H), 1.44 (s, 9H).

^{13}C NMR (126 MHz, CDCl$_3$) δ 156.0, 118.9, 79.7, 69.5, 69.5, 67.0, 67.0, 66.91, 66.87, 66.3, 48.0, 48.0, 47.9, 40.9, 32.1, 32.0, 28.4.

^{31}P NMR (121 MHz, CDCl$_3$) δ 13.3.

HRMS (ESI+) C$_{10}$H$_{22}$Br$_2$N$_2$O$_5$P *m/z* calcd [M+H]$^+$ 438.9627 obs. 438.9626
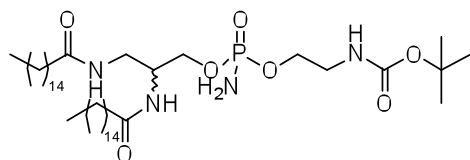
FTIR (cm^{-1}): 3279, 2977, 1671, 1518, 1238, 1166, 1029, 858, 780

Mp=70-75°C

---

[1] I. A. Fedotenko; P. L Zaffalon; Favarger, F.; Zumbuehl, A. *Tetrahedron Lett.***2010**, *51*, 5382–5384.

fed412p2/1
1H Spectrum

fed412
APC13CPD CDCl3 opt/topspin nmr 7
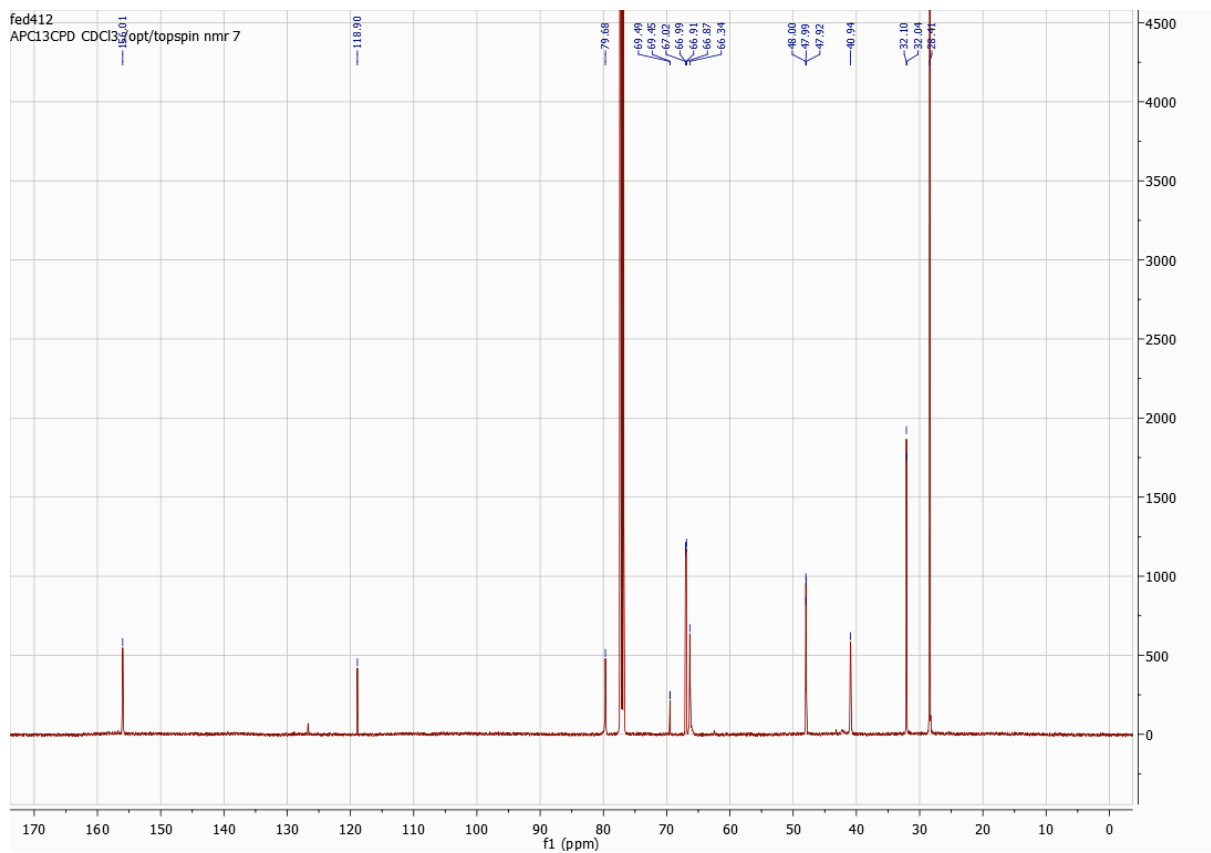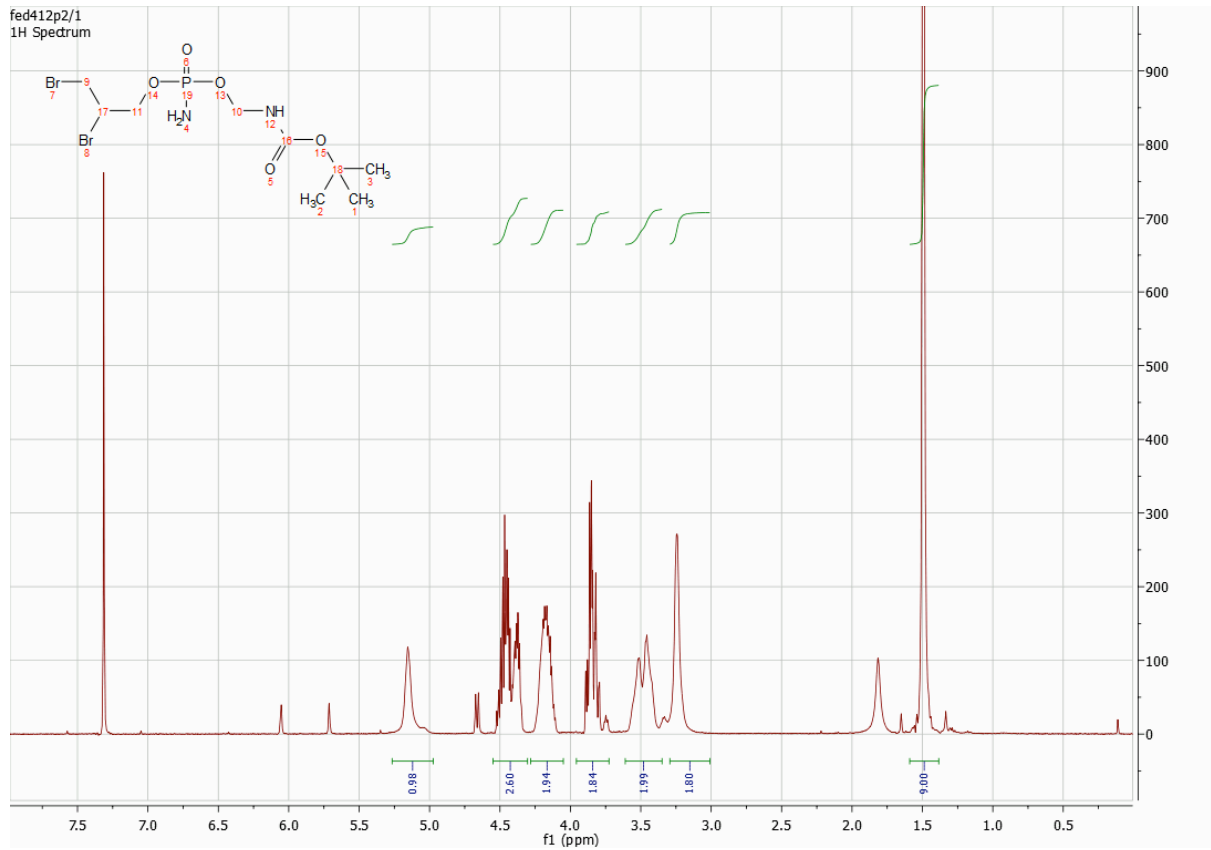
1.3 *rac*-tert-butyl (2-((amino(2,3-dipalmitamidopropoxy)phosphoryl)oxy)ethyl)carbamate (Pad-Pad-PEBoc) (7)

520 mg (1.22 mmol) of dibromide (**6**) and 199 mg (3.05 mmol) of NaN$_3$ were dissolved in dry DMF and stirred at 100 °C for 10 h. After that DMF was removed in vacuo. Any residual DMF was removed by co-evaporation with MeOH under reduced pressure. The dry crude product was separated over a silica gel column (5% MeOH-CH$_2$Cl$_2$) to give 220 mg of an oil, which crystallized upon standing. It was further dissolved in 40 mL of MeOH, and a catalytic amount of 10 weight% Pd/C (15 mg, 1 mol%) was added and H$_2$ (1 atm) was passed through the solution for 10 minutes. The solution was then stirred for 4-6 h. Then the reaction mixture was filtered through a celite-filled sintered glass funnel and washed with 50 mL of MeOH. The MeOH was removed under reduced pressure to give 187 mg of a colorless oily residue. The latter and 123 mg (1.22 mmol) of NEt$_3$ were dissolved in 20 mL of dry CH$_2$Cl$_2$. 0.373 mL (335 mg, 1.22 mmol) of palmitoyl chloride were added and the resulting mixture was stirred for 3 h. The organic solvent was removed under reduced pressure and the crude product was purified over a silica gel column (MeOH-CH$_2$Cl$_2$ 5%) to give 248 mg of a white solid (26% yield over three steps).

Rf=0.53 (MeOH-CH$_2$Cl$_2$ 5%)

^{1}H NMR (500 MHz, CDCl$_3$) δ 7.40 – 7.27 (m, 1H), 4.18 – 4.02 (m, 4H), 4.03 – 3.86 (m, 1H), 3.78 – 3.18 (m, 6H), 2.26 – 2.11 (m, 4H), 1.60 (s, 4H), 1.44 (s, 9H), 1.25 (s, 48H), 0.99 – 0.71 (m, 6H).
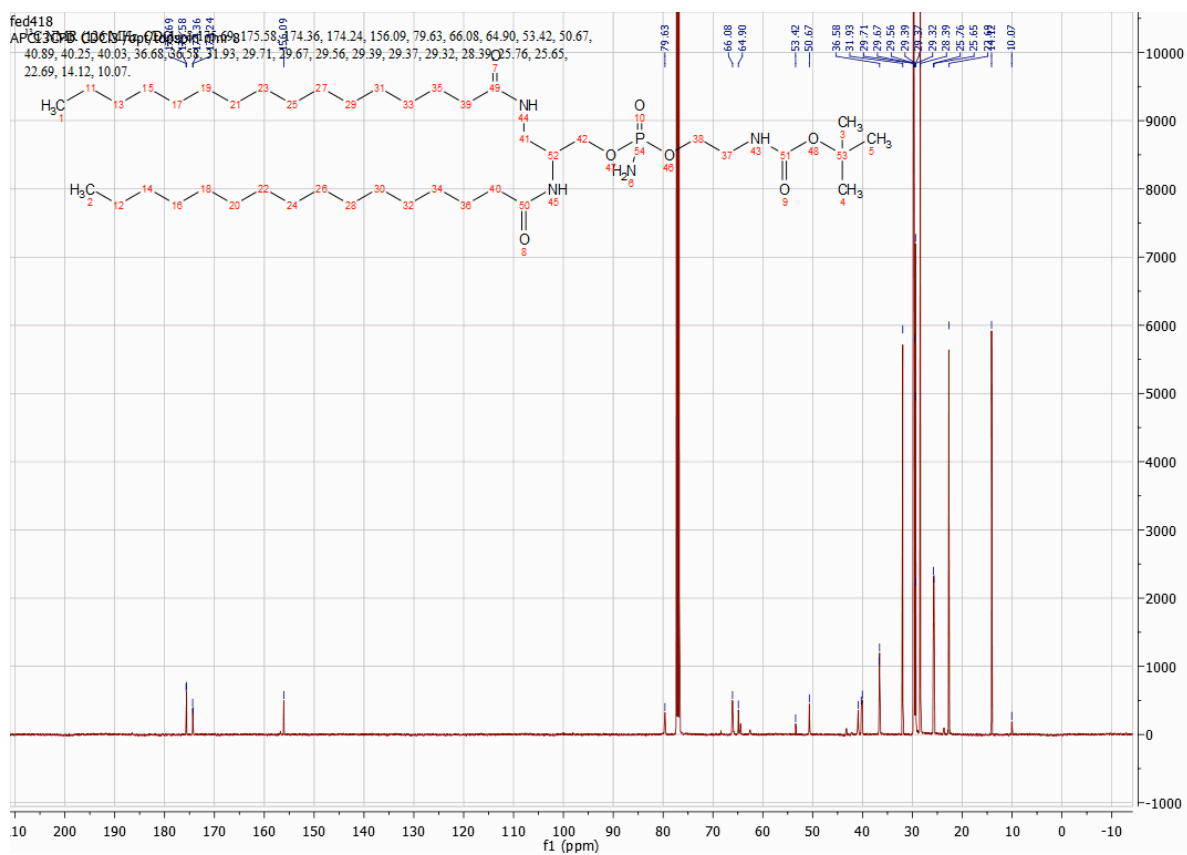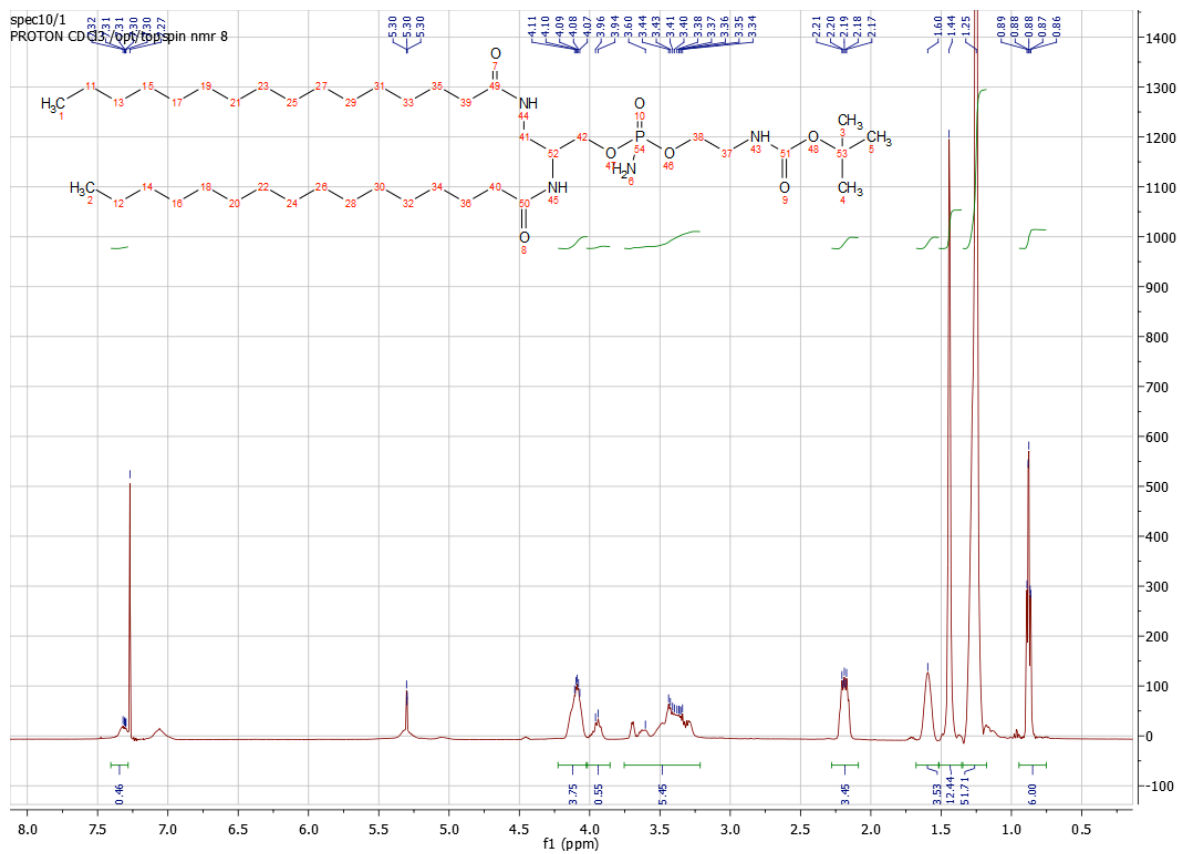
^{13}C NMR (126 MHz, CDCl$_3$) δ 175.7, 175.6, 174.4, 174.2, 156.1, 79.6, 66.1, 64.9, 53.4, 50.7, 40. 9, 40.3, 40.0, 36.7, 36.6, 31.9, 29.71, 29.67, 29.6, 29.39, 29.37, 29.3, 28.4, 25.8, 25.7, 22.7, 14.1, 10.1.

^{31}P NMR (121 MHz, CDCl$_3$) δ 15.2.

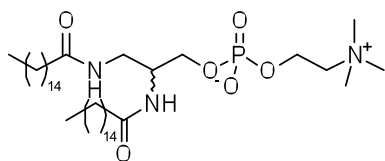**HRMS (ESI+)** C$_{42}$H$_{86}$N$_4$O$_7$P *m/z* calcd [M+H]$^{+}$789.6228 obs. 789.6206

FTIR (cm^{-1}): 3309, 2917, 2850, 1689, 1636, 1534, 1466, 1366, 1239, 1172, 1034, 1000, 723, 690

Mp=98-102°C

1.4 *rac*-2,3-dipalmitamidopropyl (2-(trimethylammonio)ethyl) phosphate (Pad-Pad-PC, 5)

To the protected phosporamidate Pad-Pad-PEBoc (**7**) (88 mg, 0.127 mmol) were added 5 mL of 1 M solution of HCl in dioxane until **7** was completely dissolved. The solution was stirred for 1.5 h. The product precipitated out of this solution and the solvent was removed under reduced pressure providing a yellow solid. It was redissolved in 15 mL of MeOH, heated up to 40°C and treated with an excess of of dimethylsulfate (120 μL, 160 mg, 1.27 mmol). After stirring for 30 min, K_2CO_3 (176 mg, 1.27 mmol) in 2 mL of H_2O was added in 15 s using a syringe. The solution was left stirring for 30 min, then the solvents were removed under a flow of nitrogen. The crude mixture was purified using a SEPHADEX LH-20 column (CH_2Cl_2-CH_3-OH-H_2O 65:25:4) giving 39 mg of a white powder (53μmol, 42% over two steps).

Rf=0.36 (CH_2Cl_2-CH_3-OH-H_2O 65:25:4)

^{1}H NMR (400 MHz, $CDCl_3$) δ 8.02 – 7.75 (m, 2H), 4.39 (s, 2H), 4.11 – 3.67 (m, 7H), 3.59 – 3.44 (m, 2H), 3.41 (s, 9H), 2.20 (dt, *J* = 8.3, 6.8 Hz, 4H), 1.60 (d, *J* = 5.9 Hz, 4H), 1.31 (s, 47H), 0.92 (t, *J* = 6.8 Hz, 6H).
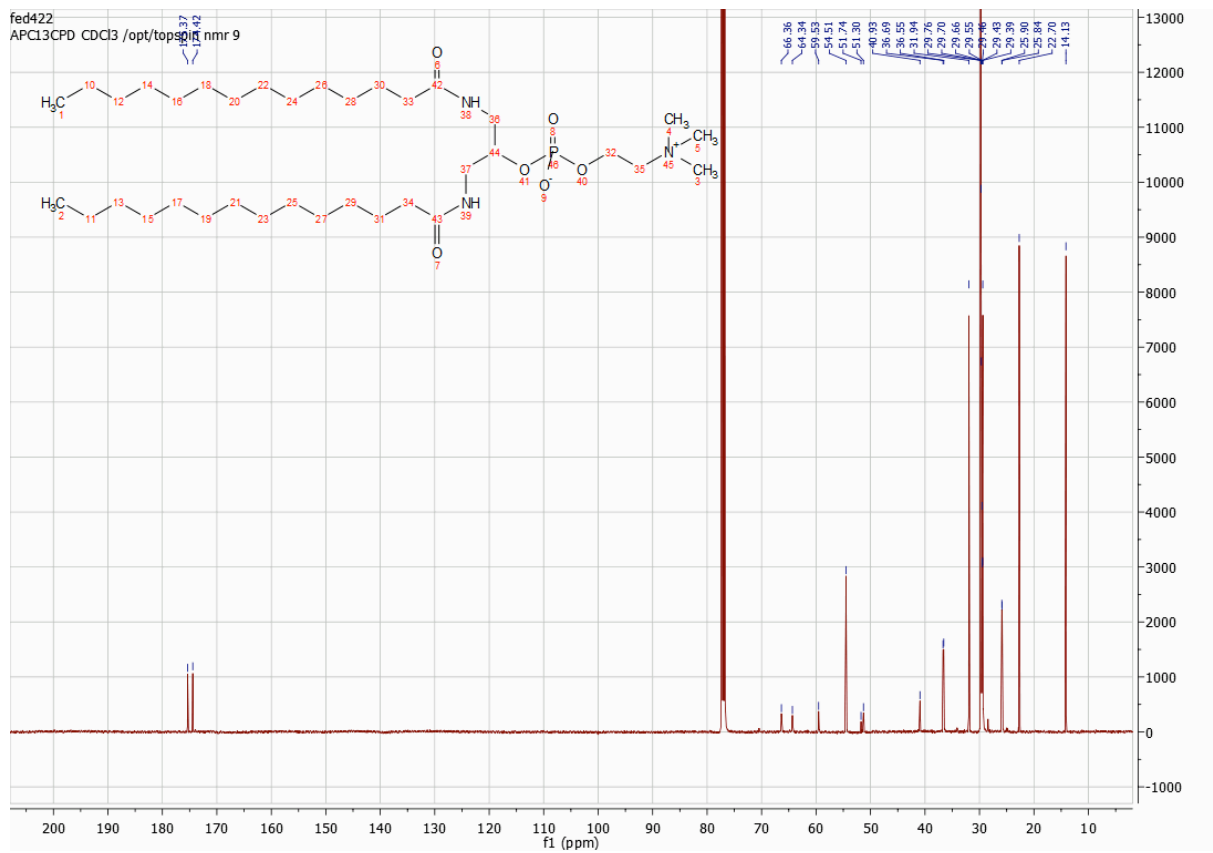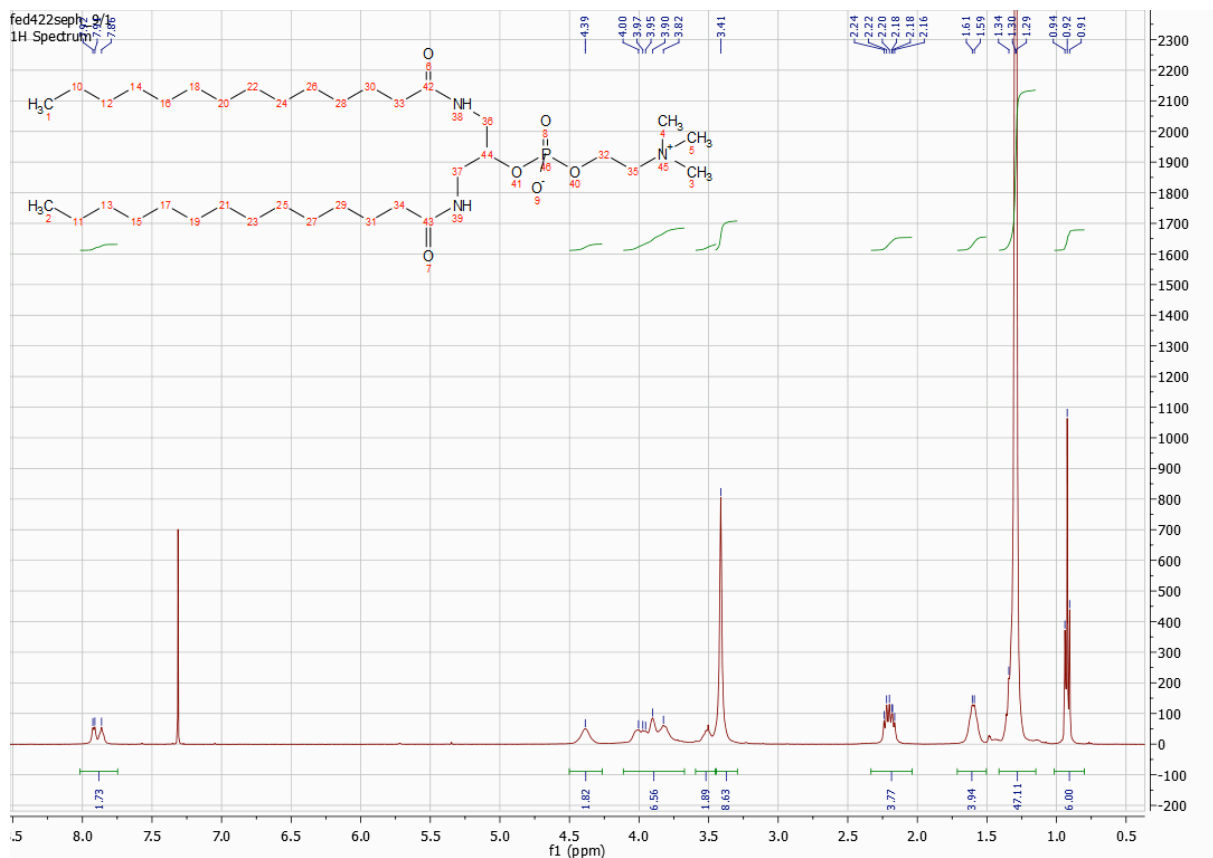
^{13}C NMR (126 MHz, $CDCl_3$) δ 175.4, 174.4, 66.4, 64.3, 59.5, 54.5, 51.7, 51.3, 40.9, 36.7, 36.6, 31.9, 29.8, 29.70, 29.66, 29.55, 29.46, 29.43, 29.39, 25.9, 25.84 22.7, 14.1.

^{31}P NMR (162 MHz, $CDCl_3$) δ 0.7.

HRMS (ESI+)*m/z* calcd [M+H]$^+$ 732.6014 obs. 732.6029

FTIR (cm^{-1}): 3287, 2917, 2850, 1634, 1544, 1468, 1232, 1055, 969, 925, 830, 722

Mp=195-198°C

2. Metabolism of Pad-PC-Pad by Phospholipase A$_2$

An experiment was carried out according to the procedure of Sunamoto *et al.*[9] A buffer solution containing 10 mM Tris.HCl, 10 mM CaCl$_2$ and 154 mM NaCl was prepared. To 50 mL of this solution, 5 mg of Phospholipase A2 (PLA2, Bee venom, 600-2400 U/mg) was added.

Dipalmitoylphosphocholine (DPPC) (5.0 mg) was dissolved in diethyl ether-ethanol (3 mL, 80:20 by vol) and the solution was divided into 20 mL glass vials in two equal portions. To one vial, buffer solution was added (200 μL, TLC spot 1, Figure S9, below). To the other, PLA2-containing buffer solution was added (200 μL, spot 2,). Pad-PC-Pad (**1**) (5.0 mg) was dissolved in diethyl ether-ethanol (3 mL, 80:20 by vol), divided into two vials and diluted with the buffer solution (spot 4) and PLA2-containing buffer solution (spot 5) in the same manner.

The solutions were stirred for 18 hours. At given time intervals, 3 μL of solution was withdrawn and submitted to TLC analysis developed by dichloromethane:methanol:water (65:25:4 by vol). Plates (Figure S9) were visualised using potassium permanganate solution.
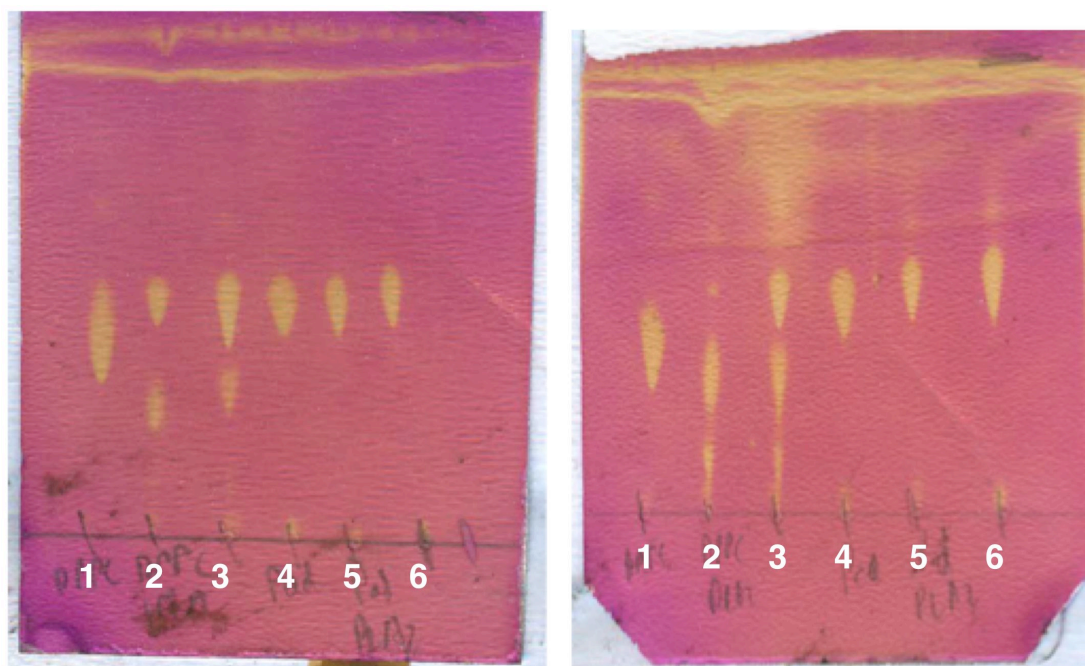
Figure S1 | Metabolism of phospholipase A by Pad-PC-Pad. TLC spots, 1-6: 1, DPPC and buffer; 2, DPPC and PLA2-containing buffer; 3, co-spot 1 and 2; 4, Pad-PC-Pad and buffer; 5, Pad-PC-Pad and PLA2-containing buffer; 6, co-spot 4 and 5.

3. DSC studies of Pad-PC-Pad
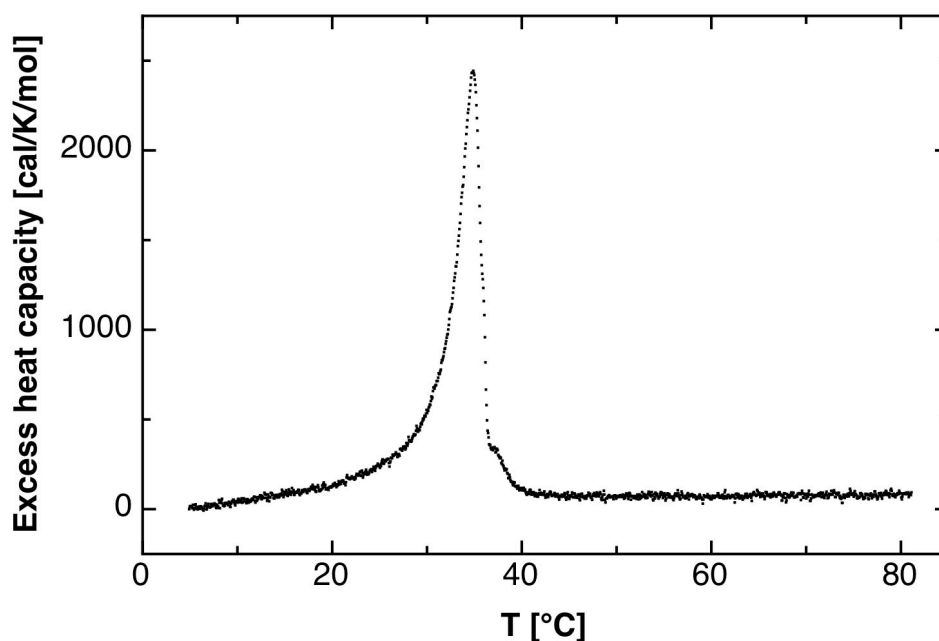
Figure S2 | DSC of Pad-PC-Pad. It is interesting to note that while the confocal image of GUVs shows a polyhedral population of vesicles with ≈30% of a liquid phase surrounded by a solid phase, DSC data show (i) a sharp transition from gel to fluid phase at 35 °C, and (ii) the *dH* corresponds to clear transitions between a solid phase and a liquid phase. One explanation for such a discrepancy could be the different packing density in GUVs/monolayer as compared to LUVs. From this figure, one would expect coexisting gel and fluid domains between ~25-40 °C. This could explain the discrepancy between the DSC melting behavior and confocal images and why coexisting domains were observed in GUVs.

4. Calculation of encapsulation efficiency of a typical non-spherical phospholipid vesicle

We assumed that the vesicle forms a lenticular shape. A typical vesicle with maximum diameter of 114 nm and maximum height of 80 nm was selected (Figure S1). It was presumed that the vesicle was symmetrical and that the discontinuity round the diameter was circular when viewed from the top. The total surface area of the vesicle was calculated as 3×10^4 nm^2 and volume was calculated

as 4.75×10^5 nm^3. For a spherical vesicle of the same surface area (i.e. lipid content), the volume was calculated as 4.90×10^5 nm^3.
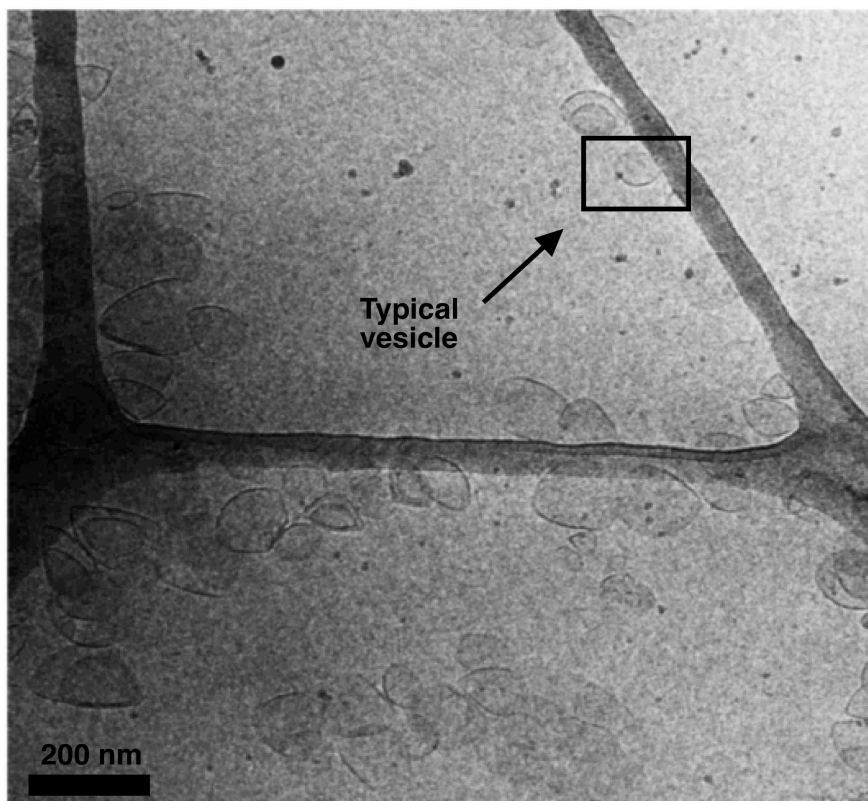
Figure S3: Pad-PC-Pad LUVET$_{100}$ Cryo-TEM image. The lenticular shape has a maximum diameter at 114 nm across the discontinuity and 80 nm at the maximum height. The vesicle is approximated to be symmetrical above and below the discontinuity.

5. Measurement of vesicle-encapsulated volume

A phosphate assay was used according to Sauder, R. et al., Meth Mol Biol 2011, 683: 129-155:

The phospholipid content is measured as phosphate content after oxidation of the phospholipids with perchloric acid. The liberated inorganic phosphate ion reacts with ammonium molybdate to phospho-molybdic acid which is measured spectrophotometrically. The sensitivity of the detection is increased in the presence of cationic malachite green. Dried KH$_2$PO$_4$ at 5-20 nmol is used for calibration. The assay is thus incompatible with phosphate based buffers. When using higher phosphate concentrations and readings later than 20 min. after reagent addition, stabilization of the colored complex with surfactants such as Tween20 is required .

1. Wear protection glasses, gloves and lab coat.

2. Coloring reagent: 1.05 g of ammonium molybdate $((NH_4)_6MoO_{24} \cdot 4H_2O)$ is dissolved in 15 mL of 6 N HCl; this is added to 0.12 g of Malachite Green previously dissolved in 85 mL of H_2O. After 30 min of stirring, the reagent is filtered (filter paper #1,Whatman; Maidstone, UK). The reagent is stored at room temperature and is freshly filtered prior to use (0.2·µm PTFE syringe filter, Whatman; Maidstone, UK). The reagent is stable for 6 weeks. Thereafter, the assay leads to increased OD values and non-linearity in the standard curve.

3. An aliquot of ~150 nmol of phospholipids (e.g. 30 µL of a 5 mM POPC suspension) is placed into a 8x60 mm borosilicate glass tube (art. 26.013.201, Glas Keller; Basel; Switzerland)

4. 100 µL of perchloric acid (70%) are added.

5. Behind a protection shield and in a fumehood, the vial is hold with a forceps (tube opening opposed to the body) and is gently boiled with a bunsen burner for approximately 3-4 min, so that the solution first turns yellow and, after a short burst of white smoke, gets clear again leaving ~1/2 of the original volume. After cooling, the solution is completed with water to 1.0 mL.

6.1. A tenth of it (100 µL; triplicate) is placed into a disposable plastic cuvette (1 cm path length), and 900 µL of the freshly filtered coloring reagent is added and immediately mixed.

6.2 For the blank, 100 µL of water are placed in a cuvette and 900 µL of the coloring reagent are added and mixed.

6.3. For the standard curve, 5, 10, 15 ad 20 µL of a 1 mM KH_2PO_4 solution are placed into a cuvette, followed by completion with water to 100 µL and addition of 900 µL of the coloring reagent.

7. A time-scan (light absorbance at 660 nm) of the most concentrated standard is recorded (i.e. 20 nmol of KH_2PO_4) , where the OD signal will increase after ~10 min to a ΔOD of ~ 0.9 (with regard to the blank) and will stay stable for ~30 min.

8. The interval between addition of the coloring reagent and achievement of stable signal (i.e. ~10 min) is kept equal for all samples.

The following results were obtained:

constants

vesicle diameter	1.14E-07	m
bilayer thickness	3.70E-09	m
Head Group area Pad-PC-Pad	5.60E-19	m^2

experimental values

[PO$_4$], assay	4.36E-06	M	± 9E-8
entrapped CF, min	7.60E-05	frxnl volume	
entrapped CF, max	1.04E-04	frxnl volume	

1. [PO$_4$] assay : predicted entrapped vol. for spherical vesicles

n° molecules in outer sphere	7.29E+04	
n° molecules in inner sphere	6.37E+04	
total molecules in spherical vesicle	1.37E+05	
moles of lipid in 1 vesicle	2.27E-19	M
predicted n° spherical vesicles	1.92E+13	in 1 L
encapsulated vol of 1 vesicle	5.07E-21	m^3
	5.07E-18	L

total expected encapsulated volume for spherical vesicles 9.75E-05 frxnl volume

within the range of entrapped CF (calc'd experimentally, results above)

2. CF assay : predicted [PO$_4$] for spherical vesicles

From entrapped CF, max:
Number of vesicles 2.05E+13 in 1 L

total expected [PO4] for spherical vesicles (CF max): 4.65E-06 M

From entrapped CF, min:
Number of vesicles 1.50E+13 in 1 L

total expected [PO$_4$] for spherical vesicles (CF min): 3.40E-06 M

within the range of [PO$_4$] assay (calc'd experimentally, results above)

6. Cytotoxicity assay

Cytotoxicity of the liposomes was investigated by the *in vitro* MTS assay (according to ISO 10993-5) and determination of cell number. L929 cells (ATCC CCL-1) and MG63 cells (ATCC CRL-1427) were seeded at a density of 1 x 10^4 cells/cm^2 in a 96 well plate format for 24 hours in standard cell culture medium. Egg-PC and Pad-PC-Pad liposomes were diluted from a 1000 μg/mL stock

(isotonic 10 mM HEPES, 10 mM NaCl, pH 7.4 buffer) in cell culture medium to concentrations of

200 μg/mL, 100 μg/mL, 20 μg/mL and 10 μg/mL. For all liposome dilutions, the HEPES/NaCl buffer

was adjusted to 20%. L929 cells were cultured for 24 or 48 hours with the liposome dilutions and

cytotoxicity was assessed in triplicate by the MTS assay (Promega), following manufacturers'

instructions (Figure S11a,b, below).

To additionally determine the cell number, crystal violet staining was performed on the MTS test

plate containing the cells (Figure S11c,d). For this, the cells were washed with PBS, fixed for 10

minutes in isopropanol, permeabilised with 0,05% Tween and stained with 0.1% crystal violet for 15

minutes. After washing with de-ionised water, the crystal violet was dissolved with 33% acetic acid

and the supernatant was measured at 600 nm to quantify cell numbers[10].
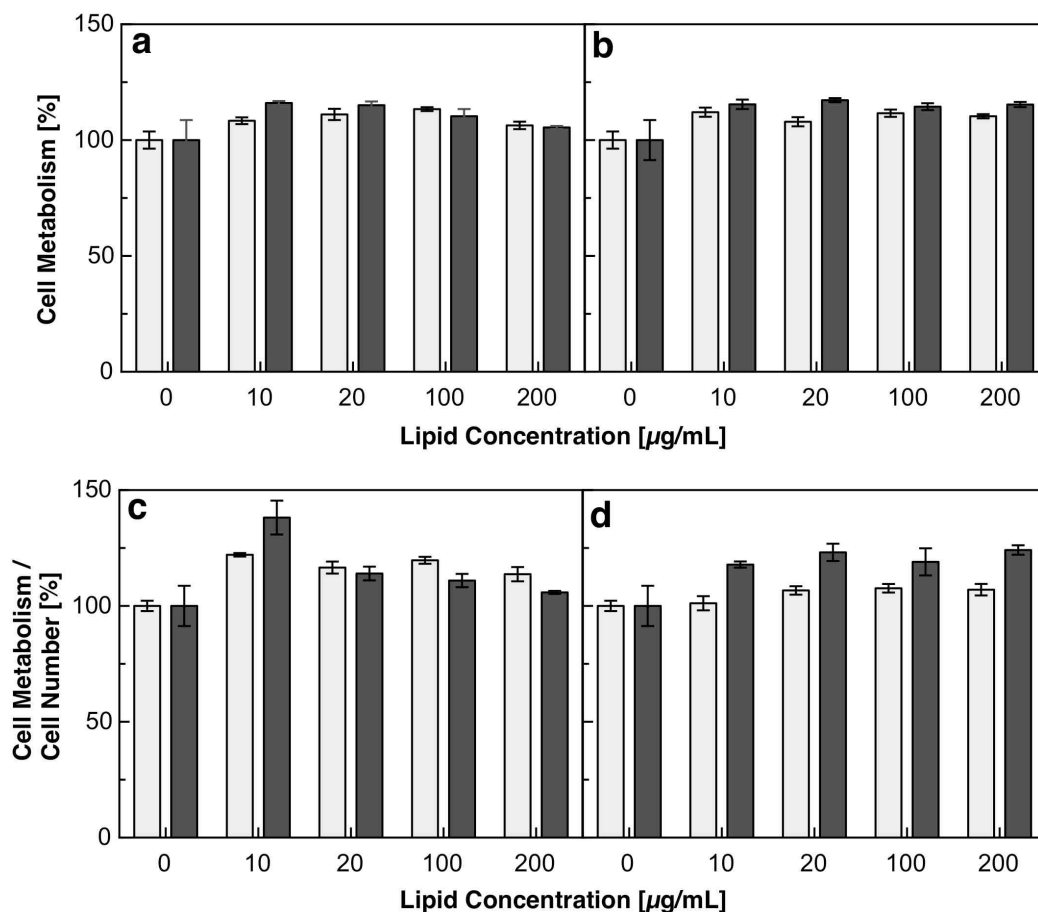
Figure S4 I Cytotoxicity assay for Pad-PC-Pad and Egg-PC liposomes at 24 hours (light gray) and 48 hours (dark gray). MTS assay of Pad-PC-Pad (**a**) and Egg-PC (**b**). MTS conversion normalised for cell number of Pad-PC-Pad (**c**) and Egg-PC (**d**) vesicles. None of the vesicle dilutions show a cytotoxic effect on L929 cells after 24 and 48 hours: MTS conversion and cell numbers were not reduced compared to the medium control, in the contrary, they where slightly

increased. A 24 hours cytotoxicity assay for MG-63 cells revealed the same results (data not shown).

7. Complement activation test

Sample	C3	C4
	g/l	g/l
Without incubation	1.05	0.198
Incubated with blank (NaCl 0.9%)	0.993	0.226
Incubated with 4.5 µM Pad-PC-Pad	0.945	0.23
Incubated with 15 µM Pad-PC-Pad	0.99	0.23
Incubated with 45 µM Pad-PC-Pad	0.988	0.229
Incubated with 0.45 µM Pad-PC-Pad	0.981	0.225

Table S1 | C3 and C4 complement pathway activation for naked Pad-PC-Pad LUVET$_{100}$ measured in the supernatants by nephelometry (Beckman Image analyser). C3 measurement investigates the common complement pathway activation. C4 measurement investigates the classical complement pathway activation. Results are mean of duplicates. There are no significant differences between the samples and the results do not suggest complement activation.

Naked Pad-PC-Pad LUVET$_{100}$ with NaCl (0.9%, pH 7.4) as both the internal and external buffer, were prepared in the usual manner. Human blood plasma(1 mL) was mixed with a 50 µL of the Pad-PC-Pad liposome suspension diluted to the appropriate concentration and incubated at 37°C for 45 min to allow complement activation. Plasma was then centrifuged at 2500g for 10 min.

8. Vesicle age
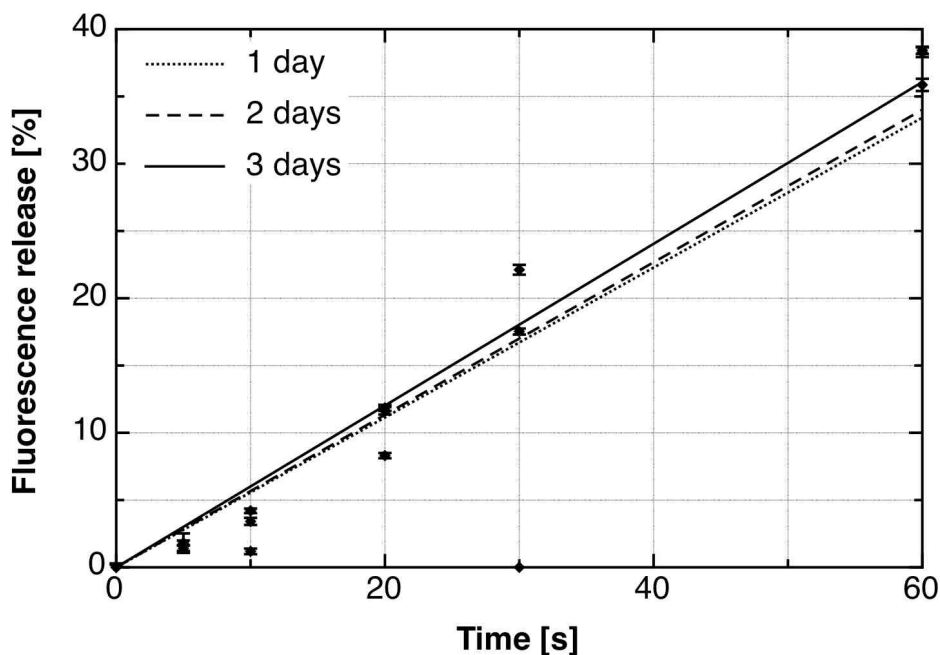
Figure S5 I Age of vesicles. After the extrusion, vesicles were stored at room temperature for 1-3 days. After this, they were subjected to vortex shaking for up to 60 s at 20 °C. No effect of prolonged storage was visible in this experiment.

9. Mechanosensitivity

In contrast to Pad-PC-Pad (**1**), EggPC (**4**) vesicles leak both at rest and being mechanically stressed. One possible explanation for this leaking could be the critical temperature which was found to be 21-26 °C for an EggPC bilayer membrane. In this temperature window a 25% lower shear force was sufficient to induce membrane leakage[3]. However, Figure 3c shows that under the conditions used in the present work, the carboxyfluorescein release from EggPC (**4**) upon shearing is independent of the applied temperature in the range between 4-45 °C. Earlier studies also concluded that the release from vesicles made from unsaturated phospholipids, such as EggPC, is less temperature dependent than from vesicles made from saturated ones[22]. We find the opposite for Pad-PC-Pad (**1**) vesicles: below their T_m of 35 °C they are equally labile to mechanical stress as EggPC vesicles. However, we observe that EggPC (**4**) vesicles are unstable resting at room temperature, whereas Pad-PC-Pad (**1**) vesicles are stable. One explanation for the intrinsic stability

could be the relative T_m of the two lipids. EggPC has a T_m of -2 °C so exists in the liquid phase at room temperature. It is easier to transport a molecule through this liquid phase than a solid phase, such as the Pad-PC-Pad (**1**) bilayer. All experiments at room temperature are therefore dealing with different phases so the release mechanism will be different.

10. Vesicle aggregation

Unlabeled LUVET$_{100}$ were formulated from pure Pad-PC-Pad (**1**) and subjected to vortex shaking. For each time point a TEM micrograph was taken. Figure S2 shows the aggregation of vesicles over time.
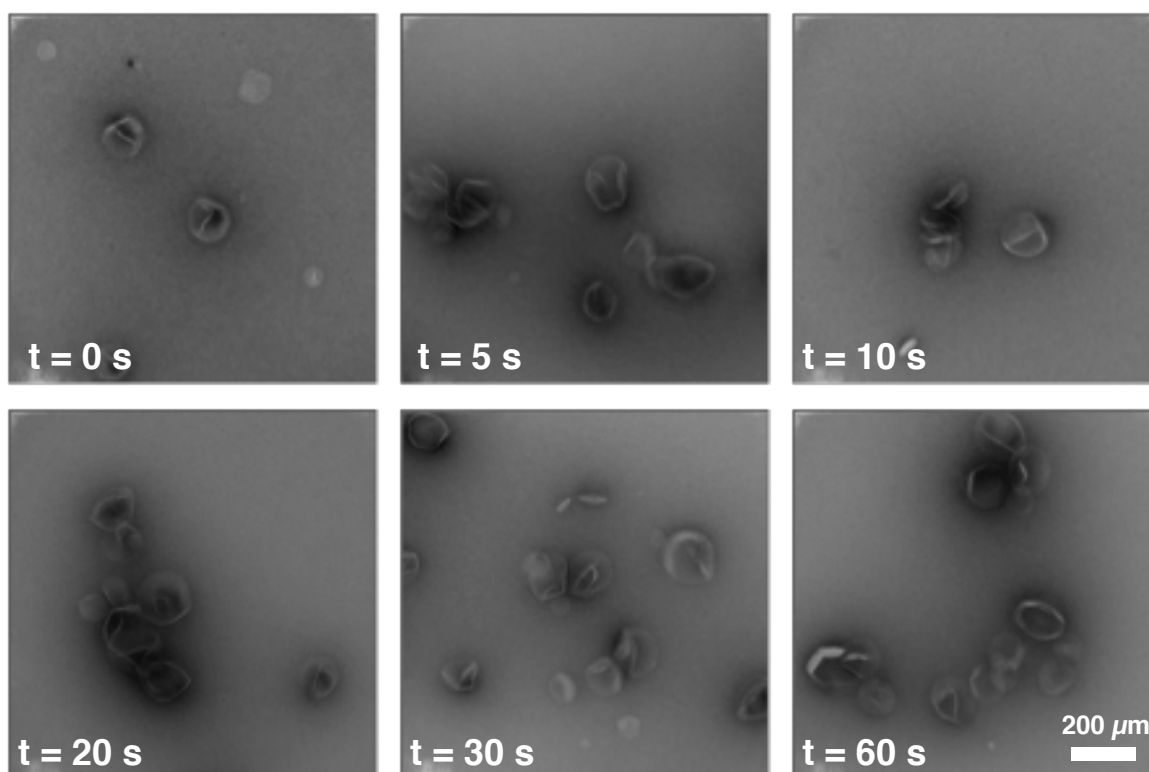
Figure S6l Transition electron micrographs of LUVs formulated from Pad-PC-Pad. The aggregation of vesicles after shaking of the vesicle suspension on a vortex shaker.

11. Additional monolayer studies of Pad-PC-Pad reveal a two-phase coexistence

A likely explanation for the shear-sensitive instability of Pad-PC-Pad vesicles compared to the natural phospholipids 2 and 3 is the propensity for phase separation in the membrane leading to an increased isothermal lateral compressibility[2]. Indeed, Pad-PC-Pad in monolayer experiments had a region of >0.1 mN/m compressibility at 20 mN/m surface pressure that was lacking for the natural phospholipids (Figure S5). The crystalline regions form ramified islands, with branches protruding from the starburst structure. The extent of crystalline island coverage is around 40%. The branch width of the primary starburst structure is constant and corresponds to about 2.2 μm or 2,700

molecules (52 Å^2 per head group). The branches do not appear to taper at the periphery. The secondary branches have a width of up to 1.3 μm. The island distribution is heterogeneous and at regions of higher island density the termini of branches fuse.

The ramified islands show a characteristic morphology, independent of the imaging technique used (BAM and fluorescence microscopy, Figure 4b,c). This indicates that the presence of the fluorescence marker does not significantly influence the island formation. The images were taken under similar experimental settings in different institutes. The captured stages of island growth are not identical.

The nature of such islanding should be studied in more detail to reveal the underlying processes as done for epitaxial metal, semiconductor and organic materials, see e.g., Müller's[5] review. A starting point could be the observation that the smaller islands are rather compact, whereas the larger ones are ramified. Therefore, the island perimeter versus island size might give rise to a similar behavior as observed for Cu/Ni(100)[6].
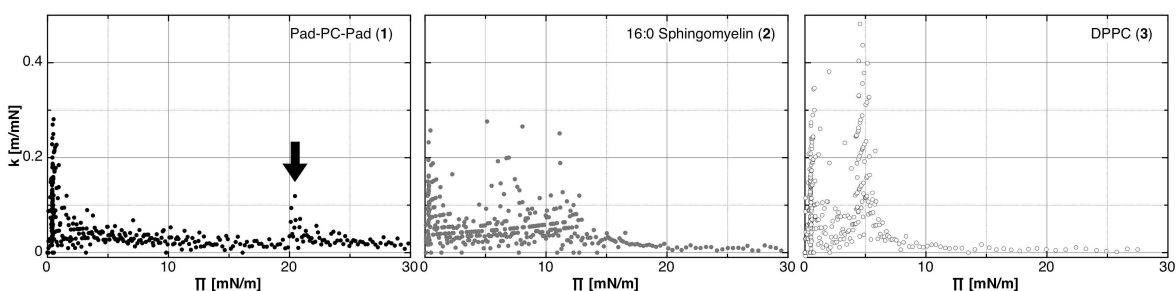
Figure S7l Additional monolayer studies of Pad-PC-Pad. The isothermal lateral compressibility of the lipids extracted from the pressure-area isotherms. The arrow points at a high compressibility found for Pad-PC-Pad that is absent at such high pressures for the other lipids tested. Negative values (decreasing slope of the isotherm) were suppressed.

**12. Influence of shearing during preparation and performing the experiments**
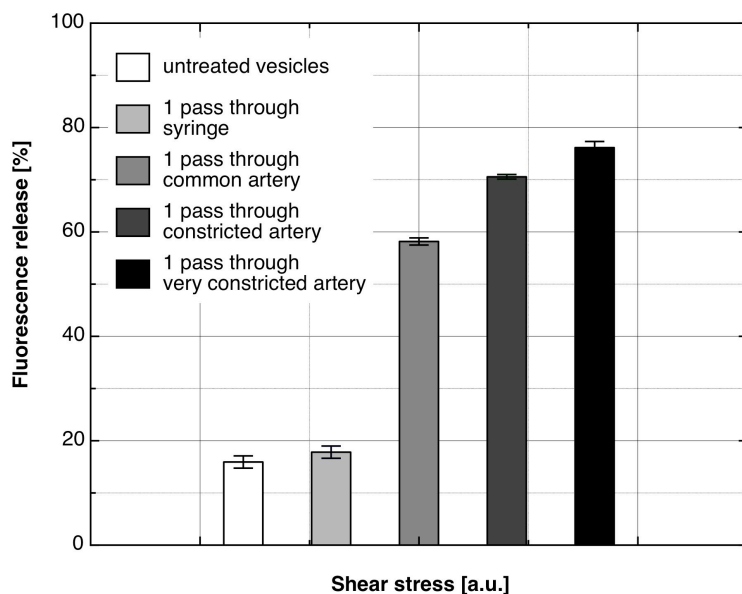
Figure S8 |Dependence of fractional release on shear stress. Increased severity of stenosis leads to an increase in observed fractional release of liposome contents. Shear stresses were calculated as ~2 Pa (common) and ~40 Pa (constricted artery) using the formula[7]: $\tau = 4\mu Q/\pi r^3$, where μ is viscosity of water at 35 °C (7.1×10^{-4} Pa·s)[8], Q is flow rate (common, 8.3×10^{-6} m^3/s; constricted 5.8×10^{-6} m^3/s), r is radius (common, 1.25 mm; constricted, 0.5 mm). Results are from one experiment and error bars represent the standard deviation of the fluorescence release in 6 200 μL samples read on a 96 well plate reader.

13. Rheology experiments with Pad-PC-Pad: Shear-stress induced release

Release studies with the *in vitro* setup (above) give a reasonable approximation of the physical forces in the body. Of course, the system represents an *in vitro* model of the physical forces in the heart, and all release observed cannot be attributed entirely to the changes in shear stress within the system. Effects such as reflow and turbulence are also present. We investigated the leakage of carboxyfluorescein from a sample of vesicles in human serum albumin (HSA, 40 g/L) and HEPES buffer after applying a pre-defined shear stress. The use of HSA in the external media also allows us to observe the effect of proteins on liposome stability. At 34 °C we found an increase in

20

fluorescence release by raising the shear stress. The presence of HSA led to an apparent stabilisation of the vesicles to shear stress induced release. Vesicles in HEPES buffer have been shown to release all their cargo on heating to 34 °C whereas vesicles in HSA-containing HEPES external buffer only release 80 %.A Bohlin CS 120 Rheometer with Casson cup and bob sample holder was used for the following experiments. Briefly, the sample was equilibrated for 2 minutes to 34 or 37 °C in the sample holder then a shear stress of 0.5–5 Pa was applied to a sample of vesicles in HEPES buffer with 40 g/L HSA for 1 minutes. The release was then measured by fluorescence spectroscopy using a 96-well plate and 200 μL samples incubated with or without Triton X-100 (4 μL) for half an hour at 25 °C. Each bar in Figure S10 is an average of six samples.
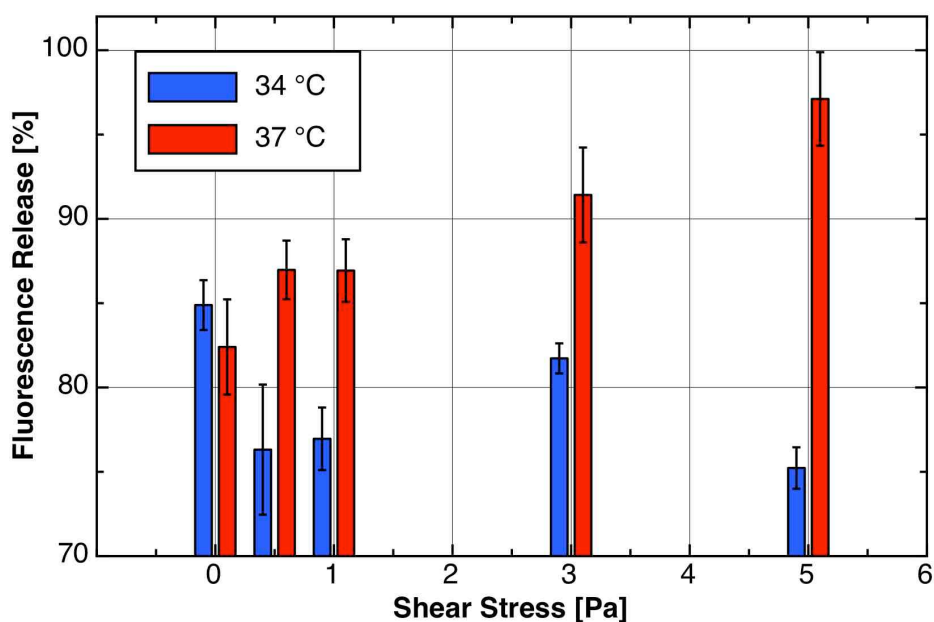
Figure S9 I Shear-stress induced release from Pad-PC-Pad vesicles. Data is at 37 °C (red) and 34 °C (blue). With increased shear stress there is a clear increase in release from the vesicles at 37 °C, just above their T_m. At 34 °C the vesicles are just below their T_m and no such correlation is observed. At 34 °C, the control at 0 Pa releases more than the vesicles subjected to shear-stress. We postulate that this is due to an effect of the HSA, which shows slightly milky solutions after heating which could lead to difraction in the spectrofluorometer.

When Triton X-100 is added to HSA at these concentrations we observe a 50% decrease in expected fluorescence intensity. The raw data in these samples are therefore multiplied by two to take this phenomenon into account. The results are shown above.

14. Release after prolonged recirculation
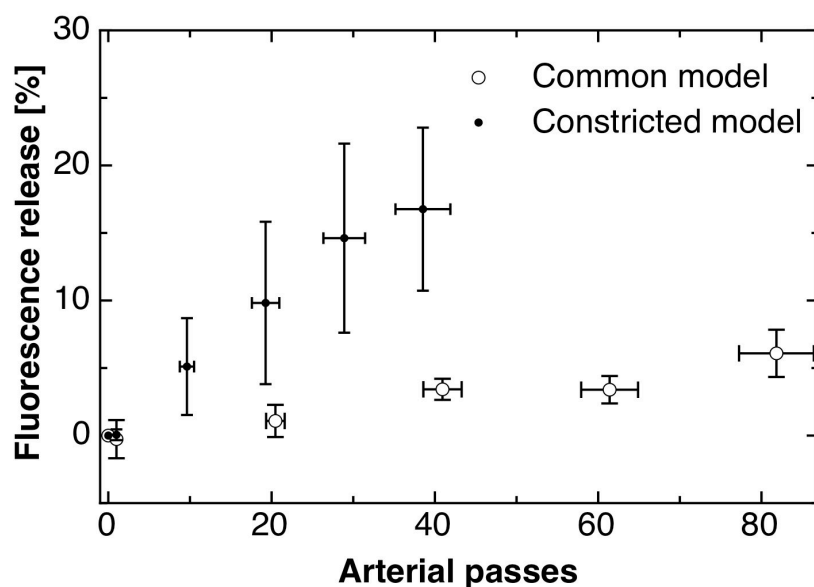
Figure S10 | Release of the Egg-PC with 0.6 mol% Brij S10. Bars indicate the standard deviation from the three experiments. The x-axis shows number of passes through the model artery. Flow rate is twice as fast in the common model. Therefore, in 20 minutes the vesicles pass an average to 80 times though this model compared to 40 times for the constricted model. It can be seen that, even though circulation for 20 minutes leads to double the number of arterial passes, the release in the common model is still smaller than that of the constricted model after 40 passes.
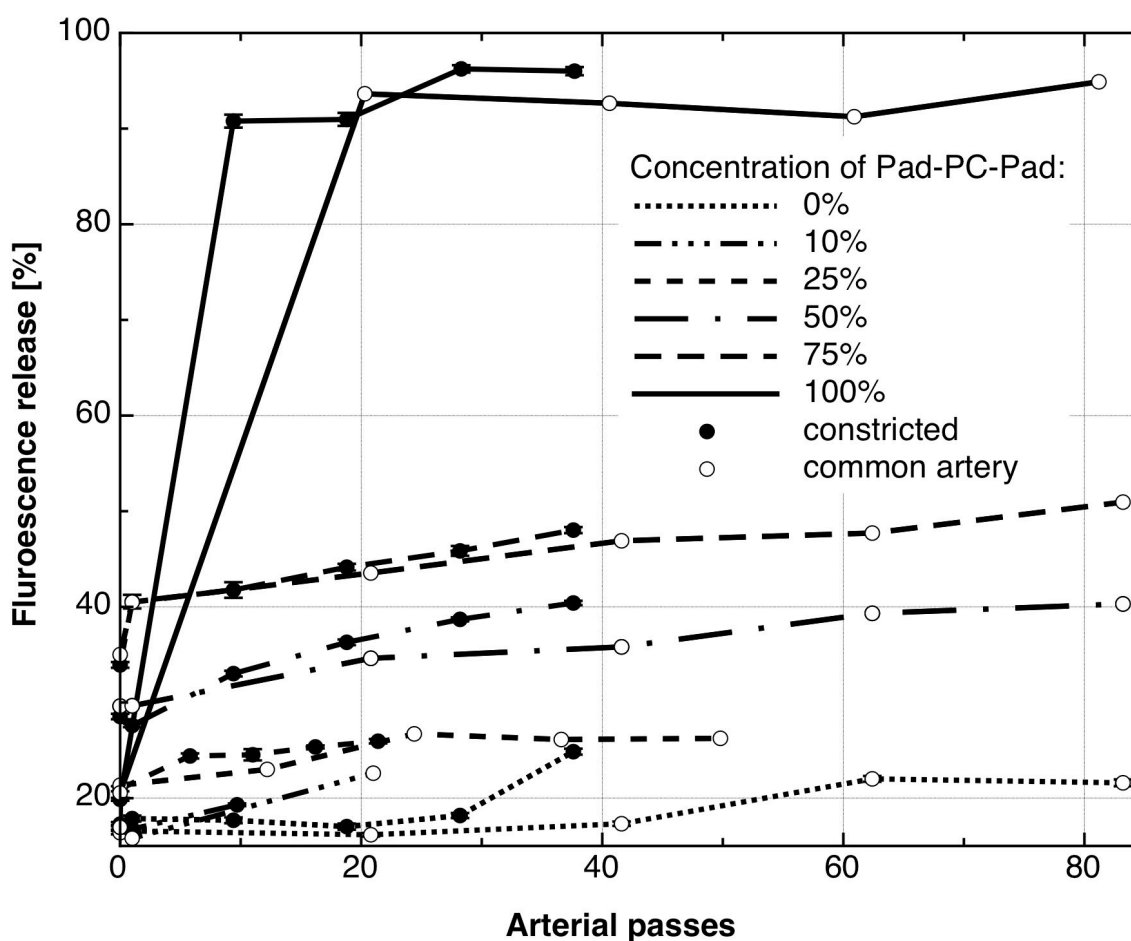
Figure S11 IFluorescent release from Egg-PC liposomes with a defined percentage of Pad-PC-Pad concentration. 100% implies 100% Pad-PC-Pad liposomes. Results from all experiments are presented as fluorescence release as a function of number of passes through the arterial model (Figure 3). The data are not normalised to zero at the zero passes so that the inherent "leakiness" of the vesicles during the preparation of the sample is also observable. It is clear that increasing the concentration of Pad-PC-Pad leads to an increase in overall release, but not to a targeted release at the stenosis over long time scales.

15. References

[1]   Fedotenko, I.A., Zaffalon, P.-L., Favarger, F. & Zumbuehl, A. The synthesis of 1,3-diamidophospholipids. *Tetrahedron Lett.***51**, 5382-5384.

[2]   Nagle, J.F. & Scott Jr, H.L. Lateral compressibility of lipid mono- and bilayers. Theory of membrane permeability. *Biochim. Biophys. Acta* **513**, 236-243 (1978).

[3]   Paparella, D. *et al.* Blood damage related to cardiopulmonary bypass: in vivo and in vitro comparison of two different centrifugal pumps. *ASAIO Journal***50**, 473-478 (2004).

[4]   Olson, F., Hunt, C.A., Szoka, F.C., Vail, W.J. & Papahadjopoulos, D. Preparation of liposomes of defined size distribution by extrusion through polycarbonate membranes. *Biochim. Biophys. Acta***557**, 9-23 (1979).

[5] Müller, B. Natural formation of nanostructures: from fundamentals in metal heteroepitaxy to applications in optics and biomaterials science. *Surf. Rev. Lett.* **8**, 169-228 (2001).

[6] Müller, B. *et al.* Island Shape Transition in Heteroepitaxial Metal Growth on Square Lattices. *Phys. Rev. Lett.* **80**, 2642-2645 (1998).

[7] Vita, J.A. *et al.* Control of shear stress in the epicardial coronary arteries of humans: Impairment by atherosclerosis. *J. Am. Coll. Cardiol.* **14**, 1193-1199 (1989).

[8] Korson, L., Drost-Hansen, W. & Millero, F.J. Viscosity of water at various temperatures. *J. Phys. Chem.* **73**, 34-39 (1969).

[9] Sunamoto, J., Goto, M. & Akiyoshi, K. Structural Stability of Lecithin Liposomes as Improved by Adding an Artificial Boundary Lipid. *Chem. Lett.* **19**, 2141-2144 (1990).

[10] van Kooten, T.G., Klein, C. L., Wagner, M. & Kirkpatrick, C.J. Focal adhesions and assessment of cytotoxicity. *J. Biomed. Mater. Res.* **46**, 33-43 (1999).

3 Conclusions and Outlook

A combination of μCT imaging techniques was most effective for building a full picture of the morphology and tissue composition of critically constricted human coronary arteries.

Advanced laboratory μCT (Phoenix|x-ray, GE Sensing & Inspection Technologies GmbH, Wunstorf, Germany) was sufficient for segmenting and extracting the lumen mesh from datasets of decalcified human coronary arteries and PMMA plastic models of a healthy and diseased human coronary artery. Laboratory μCT confirmed that the morphology of these PMMA models was in agreement with measurements performed on a human coronary artery, with the diseased PMMA model artery exhibiting a critical constriction ($>80\%$ by cross-sectional area). Both PMMA models were incorporated into an in vitro flow system with extra-corporeal circulation pump to simulate the heart. This model was used in experiments to assess the suitability of shear-stress sensitive liposome formulations as drug delivery vectors.

Absorption-SRμCT data gave a higher density and spatial resolution than laboratory μCT, and was also suitable for the extraction of a lumen mesh from decalcified human coronary afteries. Streak artifacts caused by residual plaque did not interfere with the lumen segmentation procedures. A mesh extracted from absorption-SRμCT data of a critically constricted human coronary artery was used for flow simulations, which calculated a maximum shear stress of 18 Pa, an order of magnitude higher than shear stresses observed in the normal vascular system. Such simulations are critical for determining the required shear stress "break-point" of mechano-sensitive nano-containers for targeted release at the site of critical constricted human coronary arteries.

Phase-SRμCT gives high contrast images from which different tissues types can be identified by comparison with histology. However, phase-SRμCT datasets are unsuitable for lumen segmentation and ex-

traction, due to artifacts arising from air bubbles encapsulated in the paraffin embedding material. This might be overcome by using formaldehyde as a storage medium in place of paraffin. Coupled with histology reference slices, phase-SRμCT is an indispensable tool for identifying the 3D morphology of tissue composition in decalcified human coronary arteries.

Lenticular Pad-PC-Pad liposomes contain preferential breaking points along their equators that make them sensitive to increased shear-stresses. In vitro experiments, using the above-described PMMA model of healthy or critically constricted arteries, showed that Pad-PC-Pad vesicles preferentially release encapsulated contents in areas of high shear stress such as those found in the critically constricted arteries of heart attack sufferers. The difference between release of the fluorophore carboxyfluorescein from Pad-PC-Pad vesicles passed through either a healthy or critically constricted PMMA model was 25% after one pass only. This was an order of magnitude larger than the best identified natural liposome formulation, EggPC with 0.6 mol% Brij S10, which showed 14% difference in release after 40 passes. This finding could lead to significant innovations in targeted drug delivery using solely physics-based triggers.

The project is still far from seeing a product on the market, and there are several important areas of investigation that must first be addressed. To achieve the necessary level of in vivo specificity, the minimum required corresponding percentage increase in release of encapsulated contents from mechano-sensitive nano-containers at sites of increased shear stress (i.e. critically constricted arteries) must be defined on a case by case basis, for specific drugs and applications. To achieve this, one must quantify the dose-response curves of the free drugs (in consultation with medical doctors) and the rate at which they permeate through the vesicle membrane bilayer. Additionally, a library of meshes of critically constricted human coronary arteries should be constructed, using the protocol presented in Chapter 2.1. The calculated shear stresses would quantify the required "break points" for optimal drug delivery from mechano-sensitive nano-containers. Then, by building on these findings, an optimal vesicle formulation should be identified. Using for example microfluidic devices capable of exerting a defined shear-stress on vesicles, one could subsequently measure the

"break points" of potential vesicle formulations to within 0.1 Pa. Finally, in vivo toxicology and dose-response experiments using suitable animal models are required before progressing to human trials.

Bibliography

[1] Lloyd-Jones, D., Adams, R., Carnethon, M., Simone, G. D., Ferguson, T. B., Flegal, K., Ford, E., Furie, K., Go, A., Greenlund, K., Haase, N., Hailpern, S., Ho, M., Howard, V., Kissela, B., Kittner, S., Lackland, D., Lisabeth, L., Marelli, A., McDermott, M., Meigs, J., Mozaffarian, D., Nichol, G., O'Donnell, C., Roger, V., Rosamond, W., Sacco, R., Sorlie, P., Stafford, R., Steinberger, J., Thom, T., Wasserthiel-Smoller, S., Wong, N., Wylie-Rosett, J., and Hong, Y., "Heart disease and stroke statistics-2009 update a report from the american heart association statistics committee and stroke statistics subcommittee," *Circulation* **119**(3), e21–e181 (2009).

[2] "WHO | cardiovascular diseases (CVDs)." http://www.who.int/mediacentre/factsheets/fs317/en/index.html (2012).

[3] Fuster, V., Moreno, P. R., Fayad, Z. A., Corti, R., and Badimon, J. J., "Atherothrombosis and high-risk plaque: Part i: Evolving concepts," *Journal of the American College of Cardiology* **46**(6), 937–954 (2005).

[4] Torchilin, V. P., "Recent advances with liposomes as pharmaceutical carriers," *Nature Reviews Drug Discovery* **4**(2), 145–160 (2005).

[5] Blume, G. and Cevc, G., "Liposomes for the sustained drug release in vivo," *Biochimica et Biophysica Acta (BBA) - Biomembranes* **1029**(1), 91–97 (1990).

[6] Klibanov, A. L., Maruyama, K., Torchilin, V. P., and Huang, L., "Amphipathic polyethyleneglycols effectively prolong the circulation time of liposomes," *FEBS Letters* **268**(1), 235–237 (1990).

[7] Xu, H., Wang, K. Q., Deng, Y. H., and Chen, D. W., "Effects of cleavable peg-cholesterol derivatives on the accelerated blood clearance of pegylated liposomes," *Biomaterials* **31**(17), 4757–4763 (2010).

[8] Gabizon, A., Barenholz, Y., and Bialer, M., "Prolongation of the circulation time of doxorubicin encapsulated in liposomes containing a polyethylene glycol-derivatized phospholipid - pharmacokinetic studies in rodents and dogs," *Pharmaceutical Research* **10**(5), 703–708 (1993).

[9] Gabizon, A., Shmeeda, H., and Barenholz, Y., "Pharmacokinetics of pegylated liposomal doxorubicin - review of animal and human studies," *Clinical Pharmacokinetics* **42**(5), 419–436 (2003).

[10] Gabizon, A., Shmeeda, H., Horowitz, A. T., and Zalipsky, S., "Tumor cell targeting of liposome-entrapped drugs with phospholipid-anchored folic acid-peg conjugates," *Advanced Drug Delivery Reviews* **56**(8), 1177–1192 (2004).

[11] Clayton, R., Ohagen, A., Nicol, F., Del Vecchio, A. M., Jonckers, T. H. M., Goethals, O., Van Loock, M., Michiels, L., Grigsby, J., Xu, Z., Zhang, Y. P., Gutshall, L. L., Cunningham, M., Jiang, H., Bola, S., Sarisky, R. T., and Hertogs, K., "Sustained and specific in vitro inhibition of hiv-1 replication by a protease inhibitor encapsulated in gp120-targeted liposomes," *Antiviral Research* **84**(2), 142–149 (2009).

[12] Yang, F., Jin, C., Jiang, Y., Li, J., Di, Y., Ni, Q., and Fu, D., "Liposome based delivery systems in pancreatic cancer treatment: From bench to bedside," *Cancer Treatment Reviews* **37**(8), 633–642 (2011).

[13] Aoki, K., Furuhata, S., Hatanaka, K., Maeda, M., Remy, J. S., Behr, J. P., Terada, M., and Yoshida, T., "Polyethylenimine-mediated gene transfer into pancreatic tumor dissemination in the murine peritoneal cavity," *Gene Therapy* **8**(7), 508–514 (2001).

[14] Dass, C. R. and Choong, P. F. M., "Selective gene delivery for cancer therapy using cationic liposomes: In vivo proof of applicability," *Journal of Controlled Release* **113**(2), 155–163 (2006).

[15] Endou, M., Mizuno, M., Nagata, T., Tsukada, K., Nakahara, N., Tsuno, T., Osawa, H., Kuno, T., Fujita, M., Hatano, M., and Yoshida, J., "Growth inhibition of human pancreatic cancer cells by human interferon-beta gene combined with gemcitabine," *International Journal of Molecular Medicine* **15**(2), 277–283 (2005).

[16] Li, S. D. and Huang, L., "Gene therapy progress and prospects: non-viral gene therapy by systemic delivery," *Gene Therapy* **13**(18), 1313–1319 (2006).

[17] Simões, S., Filipe, A., Faneca, H., Mano, M., Penacho, N., Düzgünes, N., and Pedroso de Lima, M., "Cationic liposomes for gene delivery," *Expert Opinion on Drug Delivery* **2**(2), 237–254 (2005).

[18] Katritsis, D., Kaiktsis, L., Chaniotis, A., Pantos, J., Efstathopoulos, E. P., and Marmarelis, V., "Wall shear stress: Theoretical considerations and methods of measurement," *Progress in Cardiovascular Diseases* **49**(5), 307–329 (2007).

[19] Johnston, B. M., Johnston, P. R., Corney, S., and Kilpatrick, D., "Non-newtonian blood flow in human right coronary arteries: steady state simulations," *Journal of Biomechanics* **37**(5), 709–720 (2004).

[20] Johnston, B. M., Johnston, P. R., Corney, S., and Kilpatrick, D., "Non-newtonian blood flow in human right coronary arteries: Transient simulations," *Journal of Biomechanics* **39**(6), 1116–1128 (2006).

[21] Rikhtegar, F., Knight, J. A., Olgac, U., Saur, S. C., Poulikakos, D., Marshall, W., Cattin, P. C., Alkadhi, H., and Kurtcuoglu, V., "Choosing the optimal wall shear parameter for the prediction of plaque location-a patient-specific computational study in human left coronary arteries," *Atherosclerosis* **221**(2), 432–437 (2012).

[22] Katritsis, D. G., Theodorakakos, A., Pantos, I., Andriotis, A., Efstathopoulos, E. P., Siontis, G., Karcanias, N., Redwood, S., and Gavaises, M., "Vortex formation and recirculation zones in left

anterior descending artery stenoses: computational fluid dynamics analysis," *Physics in Medicine and Biology* **55**(5), 1395–1411 (2010).

[23] Katritsis, D. G., Pantos, I., Korovesis, S., Hadjipavlou, M., Tzanalaridou, E., Lockie, T., Redwood, S., Voridis, E., and Efstathopoulos, E. P., "Three-dimensional analysis of vulnerable segments in the left anterior descending artery," *Coronary Artery Disease* **20**(3), 199–206 (2009).

[24] Galonska, M., Ducke, F., Kertesz-Zborilova, T., Meyer, R., Guski, H., and Knollmann, F. D., "Characterization of atherosclerotic plaques in human coronary arteries with 16-slice multidetector row computed tomography by analysis of attenuation profiles," *Academic Radiology* **15**, 222–230 (2008).

[25] Yamagishi, M., Terashima, M., Awano, K., Kijima, M., Nakatani, S., Daikoku, S., Ito, K., Yasumura, Y., and Miyatake, K., "Morphology of vulnerable coronary plaque: Insights from follow-up of patients examined by intravascular ultrasound before an acute coronary syndrome," *Journal of the American College of Cardiology* **35**(1), 106–111 (2000).

[26] Ambrose, J., Tannenbaum, M., Alexopoulos, D., Hjemdahlmonsen, C., Leavy, J., Weiss, M., Borrico, S., Gorlin, R., and Fuster, V., "Angiographic progression of coronary-artery disease and the development," *Journal of the American College of Cardiology* **12**(1), 56–62 (1988).

[27] Xin-ming, L., Cong-xin, H., Tian-song, W., Shao-wei, Z., Hua, Z., and Bei, T., "Comparison of coronary plaque composition among patients with acute coronary syndrome and stable coronary artery disease," *Chinese Medical Journal* **121**(6), 534–539 (2008).

[28] Hamdan, A., Asbach, P., Wellnhofer, E., Klein, C., Gebker, R., Kelle, S., Kilian, H., Huppertz, A., and Fleck, E., "A prospective study for comparison of mr and ct imaging for detection of coronary artery stenosis," *Journal of the American College of Cardiology: Cardiovascular Imaging* **4**(1), 50–61 (2011).

[29] Fishbein, M. C., "The vulnerable and unstable atherosclerotic plaque," *Cardiovascular Pathology* **19**(1), 6–11 (2010).

[30] Virmani, R., Burke, A. P., Farb, A., and Kolodgie, F. D., "Pathology of the vulnerable plaque," *Journal of the American College of Cardiology* **47**(8), C13–C18 (2006).

[31] Uren, N., Melin, J., Debruyne, B., Wijns, W., Baudhuin, T., and Camici, P., "Relation between myocardial blood-flow and the severity of coronary-artery stenosis," *New England Journal of Medicine* **330**(25), 1782–1788 (1994).

[32] Kranjec, I., "Atherosclerotic burden in coronary and peripheral arteries in patients with first clinical manifestation of coronary artery disease," *Journal of Cardiovascular Medicine* **12**(4), 297–299 (2011).

[33] Cerne, A. and Kranjec, I., "Atherosclerotic burden in coronary and peripheral arteries in patients with first clinical manifestation of coronary artery disease," *Heart and Vessels* **16**(6), 217–226 (2002).

[34] Huang, W.-C., Liu, C.-P., Wu, M.-T., Mar, G.-Y., Lin, S.-K., Hsiao, S.-H., Lin, S.-L., and Chiou, K.-R., "Comparing culprit lesions in st-segment elevation and non-st-segment elevation acute coronary syndrome with 64-slice multidetector computed tomography," *European Journal of Radiology* **73**(1), 74–81 (2010).

[35] Manoharan, G., Ntalianis, A., Muller, O., Hamilos, M., Sarno, G., Melikian, N., Vanderheyden, M., Heyndrickx, G. R., Wyffels, E., Wijns, W., and De Bruyne, B., "Severity of coronary arterial stenoses responsible for acute coronary syndromes," *American Journal of Cardiology* **103**(9), 1183–1188 (2009).

[36] Dettmer, M., Glaser-Gallion, N., Stolzmann, P., Glaser-Gallion, F., Fornaro, J., Feuchtner, G., Jochum, W., Alkadhi, H., Wildermuth, S., and Leschka, S., "Quantification of coronary artery stenosis with high-resolution ct in comparison with histopathology in an ex vivo study," *European Journal of Radiology* **82**(2), 264–269 (2013).

[37] Leber, A. W., Knez, A., von Ziegler, F., Becker, A., Nikolaou, K., Paul, S., Wintersperger, B., Reiser, M., Becker, C. R., Steinbeck, G., and Boekstegers, P., "Quantification of obstructive and nonobstructive coronary lesions by 64-slice computed tomography - a comparative study with quantitative coronary angiography and intravascular ultrasound," *Journal of the American College of Cardiology* **46**(1), 147–154 (2005).

[38] Ibañez, B., Badimon, J. J., and Garcia, M. J., "Diagnosis of atherosclerosis by imaging," *The American journal of medicine* **122**(1), S15–S25 (2009).

[39] Cademartiri, F., La Grutta, L., Palumbo, A., Maffei, E., Aldrovandi, A., Malago, R., Alberghina, F., Pugliese, F., Runza, G., Belgrano, M., Midiri, M., Cova, M. A., and Krestin, G. P., "Imaging techniques for the vulnerable coronary plaque," *Radiologia Medica* **112**(5), 637–659 (2007).

[40] Sun, Z., Lin, C., Davidson, R., Dong, C., and Liao, Y., "Diagnostic value of 64-slice ct angiography in coronary artery disease: A systematic review," *European Journal of Radiology* **67**(1), 78–84 (2008).

[41] Chiribiri, A., Ishida, M., Nagel, E., and Botnar, R. M., "Coronary imaging with cardiovascular magnetic resonance: Current state of the art," *Progress in Cardiovascular Diseases* **54**(3), 240–252 (2011).

[42] Chadderdon, S. M. and Kaul, S., "Myocardial contrast echocardiography in coronary artery disease," *Journal of Cardiovascular Echography* **21**(1), 1–11 (2011).

[43] Zachrisson, H., Engström, E., Engvall, J., Wigström, L., Smedby, O., and Persson, A., "Soft tissue discrimination ex vivo by dual energy computed tomography," *European journal of radiology* **75**(2), e124–128 (2010).

[44] Deyhle, H., Bunk, O., Buser, S., Krastl, G., Zitzmann, N., Ilgenstein, B., Beckmann, F., Pfeiffer, F., Weiger, R., and Müller, B., "Bio-inspired dental fillings," *Proceedings of SPIE* **7401**, 74010E–11 (2009).

[45] Rack, A., Weitkamp, T., Riotte, M., Grigoriev, D., Rack, T., Helfen, L., Baumbach, T., Dietsch, R., Holz, T., Kraemer, M., Siewert, F., Meduna, M., Cloetens, P., and Ziegler, E., "Comparative study of multilayers used in monochromators for synchrotron-based coherent hard x-ray imaging," *Journal of Synchrotron Radiation* **17**, 496–510 (2010).

[46] Schulz, G., Weitkamp, T., Zanette, I., Pfeiffer, F., Beckmann, F., David, C., Rutishauser, S., Reznikova, E., and Müller, B., "High-resolution tomographic imaging of a human cerebellum: comparison of absorption and grating-based phase contrast," *Journal of the Royal Society Interface* **7**(53), 1665–1676 (2010).

[47] Germann, M., Morel, A., Beckmann, F., Andronache, A., Jeanmonod, D., and Müller, B., "Strain fields in histological slices of brain tissue determined by synchrotron radiation-based micro computed tomography," *Journal of Neuroscience Methods* **170**(1), 149–155 (2008).

[48] Lareida, A., Beckmann, F., Schrott-Fischer, A., Glueckert, R., Freysinger, W., and Müller, B., "High-resolution x-ray tomography of the human inner ear: synchrotron radiation-based study of nerve fibre bundles, membranes and ganglion cells," *Journal of Microscopy* **234**(1), 95–102 (2009).

[49] Grodzins, L., "Optimum energies for x-ray transmission tomography of small samples - applications of synchrotron radiation to computerized-tomography .1," *Nuclear Instruments & Methods in Physics Research* **206**(3), 541–545 (1983).

[50] Thurner, P., Beckmann, F., and Müller, B., "An optimization procedure for spatial and density resolution in hard x-ray micro-computed tomography," *Nuclear Instruments & Methods in Physics Research Section B* **225**(4), 599–603 (2004).

[51] Beckmann, F., Bonse, U., Busch, F., and Günnewig, O., "X-ray microtomography (microct) using phase contrast for the investigation of organic matter," *Journal of computer assisted tomography* **21**(4), 539–553 (1997).

[52] Cloetens, P., Ludwig, W., Baruchel, J., Van Dyck, D., Van Landuyt, J., Guigay, J. P., and Schlenker, M., "Holotomography: Quantitative phase tomography with micrometer resolution using hard synchrotron radiation x rays," *Applied Physics Letters* **75**(19), 2912–2914 (1999).

[53] Davis, T., Gao, D., Gureyev, T., Stevenson, A., and Wilkins, S., "Phase-contrast imaging of weakly absorbing materials using hard x-rays," *Nature* **373**(6515), 595–598 (1995).

[54] Förster, E., Goetz, K., and Zaumseil, P., "Double crystal diffractometry for the characterization of targets for laser fusion experiments," *Kristall und Technik* **15**(8), 937–945 (1980).

[55] Koch, A., Raven, C., Spanne, P., and Snigirev, A., "X-ray imaging with submicrometer resolution employing transparent luminescent screens," *Journal of the Optical Society of America a-Optics Image Science and Vision* **15**(7), 1940–1951 (1998).

[56] Momose, A., Takeda, T., Itai, Y., and Hirano, K., "Phase-contrast x-ray computed tomography for observing biological soft tissues," *Nature Medicine* **2**(4), 473–475 (1996).

[57] Koyama, I., Momose, A., Wu, J., Lwin, T. T., and Takeda, T., "Biological imaging by x-ray phase tomography using diffraction-enhanced imaging," *Japanese Journal of Applied Physics Part 1-Regular Papers Brief Communications & Review Papers* **44**(11), 8219–8221 (2005).

[58] Weitkamp, T., Diaz, A., David, C., Pfeiffer, F., Stampanoni, M., Cloetens, P., and Ziegler, E., "X-ray phase imaging with a grating interferometer," *Optics Express* **13**(16), 6296–6304 (2005).

[59] Schulz, G., Morel, A., Imholz, M. S., Deyhle, H., Weitkamp, T., Zanette, I., Pfeiffer, F., David, C., Müller-Gerbl, M., and Müller, B., "Evaluating the microstructure of human brain tissues using synchrotron radiation-based micro-computed tomography," *Proceedings of SPIE* **7804**, 78040F (2010).

[60] Holme, M. N., Schulz, G., Deyhle, H., Weitkamp, T., Beckmann, F., Lobrinus, J. A., Rikhtegar, F., Kurtcuoglu, V., Zanette, I.,

Saxer, T., and Müller, B., "Complementary x-ray tomography techniques for histology-validated 3D imaging of soft and hard tissues using plaque-containing blood vessels as examples," *Nature Protocols* **9**, 1401–1415 (June 2014).

[61] Holme, M. N., Schulz, G., Deyhle, H., Hieber, S. E., Weitkamp, T., Beckmann, F., Herzen, J., Lobrinus, J. A., Montecucco, F., Mach, F., Zumbuehl, A., Saxer, T., and Müller, B., "Morphology of atherosclerotic coronary arteries," *Proceedings of SPIE* **8506**, 850609 (2012).

[62] Pratt, W. K., [*Digital Image Processing: PIKS Scientific Inside*], John Wiley & Sons (2007).

[63] Holme, M. N., Fedotenko, I. A., Abegg, D., Althaus, J., Babel, L., Favarger, F., Reiter, R., Tanasescu, R., Zaffalon, P.-L., Ziegler, A., Müller, B., Saxer, T., and Zumbuehl, A., "Shear-stress sensitive lenticular vesicles for targeted drug delivery," *Nature Nanotechnology* **7**(8), 536–543 (2012).

[64] Stockman, G. and Shapiro, L. G., [*Computer Vision*], Prentice Hall PTR, Upper Saddle River, NJ, USA (2001).

[65] Chakravarthy, S. R. and Giorgio, T. D., "Shear stress-facilitated calcium ion transport across lipid bilayers," *Biochimica et Biophysica Acta* **1112**(2), 197–204 (1992).

[66] Giorgio, T. D. and Yek, S. H., "The effect of bilayer composition on calcium ion transport facilitated by fluid shear stress," *Biochimica et Biophysica Acta (BBA) - Biomembranes* **1239**(1), 39–44 (1995).

[67] Bernard, A. L., Guedeau-Boudeville, M. A., Marchi-Artzner, V., Gulik-Krzywicki, T., di Meglio, J. M., and Jullien, L., "Shear-induced permeation and fusion of lipid vesicles," *Journal of Colloid and Interface Science* **287**(1), 298–306 (2005).

[68] Olson, F., Hunt, C. A., Szoka, F. C., Vail, W. J., and Papahadjopoulos, D., "Preparation of liposomes of defined size distribution by extrusion through polycarbonate membranes," *Biochimica et Biophysica Acta (BBA) - Biomembranes* **557**(1), 9–23 (1979).

[69] Weinstein, J., Yoshikami, S., Henkart, P., Blumenthal, R., and Hagins, W., "Liposome-cell interaction: transfer and intracellular release of a trapped fluorescent marker," *Science* **195**(4277), 489–492 (1977).

[70] Noguchi, H., "Polyhedral vesicles: A brownian dynamics simulation," *Physical Review E* **67**(4), 041901–041901 (2003).

[71] Fedotenko, I. A., Zaffalon, P.-L., Favarger, F., and Zumbuehl, A., "The synthesis of 1,3-diamidophospholipids," *Tetrahedron Letters* **51**(41), 5382–5384 (2010).

[72] Korin, N., Kanapathipillai, M., Matthews, B. D., Crescente, M., Brill, A., Mammoto, T., Ghosh, K., Jurek, S., Bencherif, S. A., Bhatta, D., Coskun, A. U., Feldman, C. L., Wagner, D. D., and Ingber, D. E., "Shear-activated nanotherapeutics for drug targeting to obstructed blood vessels," *Science* **337**(6095), 738–742 (2012).

[73] Barenholz, Y., "Nanomedicine: Shake up the drug containers," *Nature Nanotechnology* **7**(8) (2012).

Acknowledgments

Bert Müller, Andreas Zumbuehl and Till Saxer, my PhD supervisor and co-supervisors, for the invaluable guidance, discussions and scientific input throughout the PhD, and the opportunity to work on such a fascinating and diverse project.

The National Research Project 62 'Smart Materials' funded by the Swiss National Science Foundation for financing the project, and ongoing training both academically and in the world of industry.

Colleagues at the Universities of Basel, Geneva and Fribourg for interesting discussions, scientific advice and support, especially when the project led me in new directions. Special thanks to Hans Deyhle and Georg Schulz for crystal clear explanations and saint-like patience, and Pierre Zaffalon and Illya Fedotenko for synthesising a steady supply of Pad-PC-Pad.

The researchers at beamlines W2 and BW2 at DESY, Hamburg, Germany and ID19 at ESRF, Grenoble, France for the introduction to synchrotron-based μCT, and data collection and reconstruction. In particular, Timm Weitkamp and Felix Beckmann for their thoughtful discussions.

Thomas Pfohl for kindly agreeing to chair the PhD defence.

Mepha Pharma AG for funding in the initial stages of the project.

UniTec of the University of Geneva for funding and assistance in patent preparation and submission.

Curriculum Vitae

Education

2009 - 2013 – Doctorate, University of Basel

A Shear-Stress Responsive Nano-Container To Target Critically Constricted Arteries.

Supervisors: Prof. Bert Müller (University of Basel), Prof. Andreas Zumbuehl (University of Fribourg), Dr. med. Till Saxer (University Hospitals of Geneva).

Winner of the National Research Project 62 PhD Award from the Swiss National Science Foundation.

2004 - 2009 – Masters in Chemistry with a Year in Industry (First Class Honours), Imperial College London

Masters Thesis: *Fishing For New Drug Targets With Synthetic Chemistry Hooks.*

Supervisor: Prof. Andrew Miller, Genetic Therapies Centre (Imperial College London).

Shortlisted for the Salter's Prize 2009 (for candidates with potential to become leaders in the chemical or related industries that support UK industry).

1998 - 2004 – Secondary Education, North Berwick High School, Scotland

School Dux (best academic performance).

Professional Experience

2007 - 2008 – F. Hoffmann-La Roche, Basel

Intern, Medicinal Chemistry Lead Generation Department.

Presentations

Oral Presentations

5. M. N. Holme, T. Saxer, A. Zumbuehl, B. Müller, "Shear stress sensitive nanocontainers with tunable release properties."
   Nano-Med 2012, London, United Kingdom, 7-9 November 2012.

4. **Invited seminar**
   M. N. Holme, "Mechano-sensitive nano-conatiners for targeted drug delivery in atherosclerosis : the importance of imaging vessel morphology."
   Synchrotron SOLEIL, Gif-sur-Yvette, France, 14 October 2012.

3. **1st Prize - Young Research's Award (best oral presentation)**
   M. N. Holme, T. Saxer, A. Zumbuehl, B. Müller, "Shear stress sensitive nano-containers for targeted drug delivery."
   9th International Conference on Nanosciences and Nanotechnologies (NN12), Thessaloniki, Greece, 6 July 2012.

2. M. N. Holme, B. Müller, T. Saxer, A. Zumbuehl, "Shear stress sensitive nano-containers for targeted drug delivery."
   Swiss Chemical Society Fall Meeting 2011, EPFL Lausanne, 9 September 2011.

1. M. N. Holme, A. Zumbuehl, T. Saxer, B. Müller, "Shear stress sensitive nanocontainers for targeted drug delivery."
   Swiss National Science Foundation, NRP 62 Meeting, University of Fribourg, 22 August 2011.

Poster Presentations

7. M. N. Holme, B. Müller, A. Zumbuehl, T. Saxer, "Shear stress sensitive nanocontainers for targeted drug delivery."
Swiss Chemical Society Fall Meeting, ETH Zurich, 13 September 2012.

6. **2nd prize - Poster Award**
M. N. Holme, T. Weitkamp, F. Beckmann, J. A. Lobrinus, A. Zumbuehl, T. Saxer, B. Müller, "Revealing the morphology of coronary arteries to design nanocontainers for targeted drug delivery."
5th European Conference for Clinical Nanomedicine (CLINAM), Basel, 7-9 May 2012.

5. M. N. Holme, I. A. Fedotenko, T. Saxer, A. Zumbuehl, B. Müller, "Shear stress sensitive nanocontainers for targeted drug delivery."
Swiss Soft Days, Gevena, 12 June 2012.

4. M. N. Holme, A. Zumbuehl, T. Saxer, B. Müller, "Shear stress sensitive nanocontainers for targeted drug delivery."
Swiss National Science Foundation, NRP 62 Meeting, University of Fribourg, 22 August 2011.

3. M. N. Holme, B. Müller, A. Zumbuehl, T. Saxer, "Shear stress sensitive nanocontainers for targeted drug delivery."
4th European Conference for Clinical Nanomedicine (CLINAM), Basel, 23-25 May 2011.

2. M. N. Holme, A. Zumbuehl, T. Saxer, B. Müller, "Shear stress sensitive nanocontainers for targeted drug delivery."
17th Swiss Conference on Biomaterials, Yverdon-les-Bains, 4 May 2011.

1. M. N. Holme, B. Müller, A. Zumbuehl, T. Saxer, "Nanocontainers for the targeted delivery of nitroglycerine during myocardial infarction."
3rd European Conference for Clinical Nanomedicine (CLINAM), Basel, 10-12 May 2010.